
Nonequilibrium phase transition in binary complex plasmas

Chengran Du



München 2012

Nonequilibrium phase transition in binary complex plasmas

Chengran Du

Dissertation
an der Fakultät für Physik
der Ludwig–Maximilians–Universität
München

vorgelegt von
Chengran Du
aus Shanghai, China

München, den 2012

Erstgutachter: Prof. Dr. Gregor E. Morfill

Zweitgutachter: Prof. Dr. Hartmut Löwen

Tag der mündlichen Prüfung: 16. 01. 2013

Contents

Acknowledgements	vii
Zusammenfassung	x
Abstract	xii
1 Introduction to complex plasmas	1
1.1 RF discharge and plasma diagnostics	2
1.1.1 Equivalent circuit approach	3
1.1.2 Probe measurement	4
1.1.3 Particle-in-cell simulation	5
1.2 Charging of particles in complex plasmas	6
1.2.1 Charging in isotropic plasmas	7
1.2.2 Charging in anisotropic plasmas	8
1.2.3 Some other charging mechanism	9
1.3 Forces on particles in complex plasmas	10
1.3.1 Gravitational force	10
1.3.2 Ion drag force	10
1.3.3 Neutral drag force	11
1.3.4 Electromagnetic force	12
1.3.5 Thermophoretic force	12
1.4 Complex plasma as soft matter	13
1.4.1 Binary complex plasma and non-additivity	14
1.4.2 Channeling effect	15
1.4.3 Lane formation	16
2 Particle charging	17
2.1 Objectives	17
2.2 Methods	18
2.2.1 Measurement of particle charge in deep sheath	18
2.2.2 Model of particle charging with various discharge frequencies	20
2.3 Results	21
2.4 Outlook	21

3	Agglomeration of microparticles	23
3.1	Objectives	23
3.2	Methods	23
3.3	Results	24
3.4	Outlook	25
4	Interaction of 2D crystalline lattices with upstream particles	27
4.1	Objectives	27
4.2	Methods	28
4.3	Results	29
4.4	Outlook	31
5	Lane formation in binary complex plasmas	33
5.1	Objectives	33
5.2	Methods	34
5.2.1	Langevin dynamics simulations	35
5.2.2	Experiment on board the ISS	35
5.2.3	Experiment on the ground	37
5.3	Results	39
5.4	Outlook	41
6	Summary	43
	List of figures	45
	Bibliography	54
	Publication list	56
	Curriculum vitae	58
	Enclosed papers	59

Acknowledgements

I would like to take the chance to express my gratitude to all those who ever supported and helped me complete this dissertation.

First of all, I would like to thank Prof. Gregor Morfill for giving me the opportunity to start and carry on my research in Max-Planck-Institute for Extraterrestrial Physics. His kindness and wisdom as well as the resources and freedom that he has provided has made me enjoy my stay here more than anywhere else. I particularly appreciate his support as I had difficulties working on the paper of lane formation, which is eventually published in NJP.

I would like to give my special thanks to my advisors Dr. Hubertus Thomas, Dr. Alexei Ivlev for their instructions, encouragements and supports all the time. They spent quite a lot of time to explain me everything about complex plasma, taught me the experimental techniques personally and brought me always new ideas to solve my problems. Without them, this work could never be achieved.

I am grateful to all the colleagues in the complex-plasma group in MPE: Thanks to Tetyana for the time we spent together in the lab. I really enjoyed that. Thanks to Vladimir N. and Sergey Z. for their guidance on the experiments in the GEC chamber. I learned a lot from their attitude towards the scientific work. Thanks to Sergey K. for the help on my very first referee job. Thanks to Christina, Lisa, Daniel, Ralf, Michael, and Sloboden for the great experience in the parabolic flight. Thanks to Uwe and Peter for helping me solve various computer problems all the time and teaching me to use the SPIT software. Special thanks to Robert and Jayson for everything they have done for me (too much to list) and to Mierk for introducing me to this great group. I also want to thank Angelika, Christoph, Dong, Guido, Julia, Jin, Katinka, Lu-Jing, Manis, Mikhail, Milenko, Martin, Lénaïc, Pintu, Philip, Satoshi, Mr. Steffes, Tetsuji, Tanja, Tobi, Thomas, and Yang-Fang for the helpful discussions and more importantly for the wonderful time we spent together in the group.

Besides, I also want to thank our Russian colleagues in IHED, Vladimir M. and Andrey, for helpful discussions in many occasions and hosting my stay in Korolev. I had a really good time in Moscow.

Additionally, I would like to thank Gregor, Hubertus, Markus, Christoph and Vladimir N. for helping me to improve this dissertation and Lisa for polishing the abstract in German. And I want to thank George for taking his time to improve the English writing of this dissertation.

Last but not least, I would like to thank my parents not only for their strong support during my study abroad but also for their foster and understanding through my life. And special thanks has to be given to Hui, who is always with me and brings me happiness no matter how far apart we are.

Zusammenfassung

Komplexe Plasmen sind Systeme bestehend aus schwach ionisierten Gasen und mesoskopischen Partikeln. Partikel in einem Plasma erhalten ihre Ladung hauptsächlich durch den Fluß von Ionen und Elektronen auf denen Oberflächen. Abhängig von der Teilchengröße und den Plasmabedingungen kann die Ladung pro Teilchen mehrere tausend Elementarladungen betragen. Da das Hintergrundgas sehr dünn ist, können Partikelsysteme unabhängig von dem Plasma betrachtet werden. In vielen Fällen kann das Partikelwechselwirkungspotential als Yukawapotential angenähert werden, welches im Wesentlichen ein abgeschirmtes Coulombpotential ist. Kapitel 1 ist eine kurze Einleitung in die theoretischen Konzepte komplexer Plasmen.

Aufgrund der Bedeutung des Mechanismus, beginne ich diese Arbeit mit der Diskussion der Teilchenladung für zwei verschiedene Situationen in Kapitel 2. Zunächst beschreibe ich ein einzigartiges Experiment, die “Coulomb-Explosion”, zur Messung der Teilchenladung tief in der Plasmarandschicht. Ein Hybrid-Analyseverfahren, bestehend aus Teilchenverfolgung, MD und PIC Simulationen, wurde angewendet um die Ladung im Anfangsstadium der Explosion abzuschätzen. Dieses wird mit einer theoretische Methode zur Bestimmung der Partikelladung im Bulk-Plasma bei verschiedenen Entladungsfrequenzen ergänzt. Die Abhängigkeit der Partikelladung von der Entladungsfrequenz wird bei drei verschiedenen Drücken gezeigt. Das verwendete Modell ist hilfreich um die Veränderung der Teilchenladung in Abhängigkeit der Entladungsfrequenz abzuschätzen.

Die hohe Teilchenladung und die damit verbundene abstoßende Teilchenwechselwirkung verhindern Partikelagglomeration. In Kapitel 3 stelle ich ein Experiment vor, in dem Partikelagglomeration durch selbst-angeregte Wellen induziert wird. Innerhalb der Wellen werden die Teilchen derart beschleunigt, dass das abstoßende Potential durch die erhöhte kinetische Energie überwunden werden kann. Die resultierenden Agglomerate werden mit einem “Long-Distance” Mikroskop überprüft.

Im Folgenden stelle ich ein System binärer komplexer Plasmen vor. Unter bestimmten Bedingungen können monodisperse Partikel in einer Monolage eingefangen werden. Die Teilchen ordnen sich in einem Dreiecksgitter mit hexagonaler Symmetrie an. Dies ist als 2D Plasmakristall bekannt. Wenn ein sich bewegendes, einzelnes Teilchen einer anderen Spezies in das System eingeführt wird, verursacht es eine Störung des Kristallgitters. In Kapitel 4 werden die Untersuchungen der Wechselwirkung des Kristallgitters mit einem sich oberhalb des Gitters (stromaufwärts des Ionenflusses) befindlichen Teilchens diskutiert. Dieses zusätzliche Partikel erzeugt einen Mach-Kegel, da es sich mit einer

Geschwindigkeit, schneller als der Schall in dem System bewegt. Das stromaufwärts befindliche Teilchen neigt dazu sich zwischen Reihen von Teilchen in dem Gitter zu bewegen, was als "Channeling-Effekt" bekannt ist.

Wenn Teilchen einer Spezies eine Partikelwolke einer anderen durchdringen, bilden sowohl die durchfließende als auch die durchflossene Teilchenwolke Kettenstrukturen ("Lanes") aus. In komplexen Plasmen ist die Wechselwirkung verschiedener Partikel immer stärker abstoßend als das geometrische Mittel der Wechselwirkung gleicher Partikel. Diese Asymmetrie in der gegenseitigen Wechselwirkung heißt "Positive nicht-Additivität". Deren Grad wird von dem nicht-Additivitäts Parameter bestimmt. In Kapitel 5 beschreibe ich zuerst die Ergebnisse von Langevin-Simulationen, um die Abhängigkeit der "Lane - Formation" von dem nicht-Additivitäts Parameters zu studieren. Weiterhin wurde die Rolle des Anfangszustands numerisch untersucht. Zusätzlich wurde eine Reihe umfassender Experimente zur "Lane - Formation" an Bord der Internationalen Raumstation (ISS) durchgeführt. Die Auswertung der Experimente konzentrierte sich auf die Struktur der durchflossenen Teilchen. Der Einfluss der Partikeldichten und -größe wurden untersucht. Das Studium zweier aufeinanderfolgenden Durchdringungen offenbarte einen "Memory-Effekt" in der Kettenstruktur. Zusätzlich wurde ein Übergang von freier "Lane-Formation" zu einem, von Entmischung dominierten, Zustand des Nichtgleichgewichtsystems innerhalb einer Experimentreihe beobachtet. Schließlich stelle ich einen ergänzenden Versuch zur "Lane-Formation" in erdgebundenen Experimenten vor. Die Schwerkraft wurde hier durch thermophoretische Kräfte kompensiert. In dieser Versuchsreihe konnten die durch unregelmäßige Teilchengeschwindigkeiten und Inhomgenitäten in der durchflossenen Teilchenwolke entstehenden Nachteile erfolgreich überwunden werden. Mit diesem Modell-System kann die "Lane-Formation" im Detail untersucht werden und die Ergebnisse mit denen numerischer Simulationen und denen aus Experimenten in Kolloiden verglichen werden.

Abstract

Complex plasma is a system composed of weakly ionized gas and mesoscopic particles. The particles are charged mainly by absorbing ions and electrons in the plasma. The charge can reach several thousands of elementary charges depending on the particle size and plasma conditions. Since the background gas is dilute, we can treat the charged particles as a system independent from the plasma. In many cases, the interparticle interaction can be approximated as Yukawa potential, which is essentially a screened Coulomb interaction. A brief introduction covering some basic theoretical aspects of complex plasma is given in Chapter 1.

Because of the importance of the particle charging mechanism, we start this thesis with studying particle charge under two situations in Chapter 2. First we introduce a unique experiment of Coulomb “explosion” to measure the particle charge deep in the sheath. A hybrid analysis method composed of particle tracking, molecular dynamics simulation and particle-in-cell simulation is applied to estimate the particle charge at the initial stage of the “explosion”. Second we develop a theoretical method to calculate the particle charge in the bulk plasma with different discharge frequencies. We show the dependence of particle charge on the discharge frequency at three different gas pressures. The model is rather simple and thus we can use it for preliminary estimation of the change of particle charge as a result of changing the discharge frequency.

Since the particles are heavily charged, the repulsive interparticle interactions prevent particle agglomeration. In Chapter 3 we introduce an experiment to realize particle agglomeration, which is induced by self-excited waves. In the waves the microparticles are accelerated so that the repulsive potential can be overcome by the kinetic energy. We verify the results by using a long-distance microscope.

We then start to study a system of binary complex plasmas. Under certain conditions, monodisperse microparticles can be confined in a monolayer, self-organizing in a triangular lattice with hexagonal symmetry. This is known as 2D plasma crystal. If a moving single particle of another species is introduced into the system, it creates a disturbance on the crystal lattice. In Chapter 4, we study the interaction of the crystal lattice with a particle moving above it (upstream of the ion flow). This extra particle generates a Mach cone as it moves faster than the sound speed. It turns out that the upstream particle tends to move between rows of particles in the lattice layer, which is known as “channeling” effect.

As particles of one species penetrate into a particle cloud of another species, both the penetrating particles and background particles form lane structure. For microparticles

of two species, the interspecific interaction is always more repulsive than the geometric mean of two intraspecific interactions. This asymmetry in the mutual interaction is called “positive non-additivity” and its degree is measured by the non-additivity parameter. In Chapter 5 we first employ Langevin dynamics simulation to study the dependence of lane formation on positive non-additivity parameter. The role of initial condition has been also studied numerically. Second we comprehensively investigate a series of experiments on lane formation performed on board the International Space Station. In the experiments, we focus on the lanes formed by the background particles. The influence of the number density ratio and size ratio between two particle types has been studied. By investigating two consecutive penetrations, a “memory” effect of the first penetration on the second is revealed. In addition, we observe a crossover from free lane formation to a demixing dominated mode of the nonequilibrium system in the same set of experiments. Finally, we introduce an supplementary experiment to investigate the lane formation of the penetrating particles on the ground. The gravity is compensated by the thermophoretic force. The experiment successfully overcomes the drawbacks in terms of non-uniformity of the speed of the penetrating particles and inhomogeneity of the background particles. Using it as a model system we can investigate the process of lane formation in great detail and directly compare it with numerical simulations and experiments in colloidal suspensions.

Chapter 1

Introduction to complex plasmas

A plasma is known as the fourth classical state of matter [42]. It is a multi-particle system including ions, electrons and neutrals coupled together. Plasma exists widely in nature. In fact, over 99% of the visible matter in the universe is in the plasma state [11]. For example, the intergalactic medium, the interstellar medium, and solar wind are all mainly diffuse plasma. The stars such as the sun in our solar system are made of dense plasma.

A complex plasma can be loosely defined as plasma with an additional charged component of microparticles¹ [114]. Since the first observation of the formation of spokes in Saturn's B ring [45, 83, 115], see Fig. 1.4, the field of complex plasma has drawn a lot of attention. However, for quite long time, complex plasma is actively studied mainly in the scope of astronomy, astrophysics and geophysics [25, 46, 49, 108].

In 1994, a series of experimental realizations of plasma crystal were reported [24, 47, 119]. The microparticles were confined in a multilayer system in a radio frequency (rf) discharge and self-organized in a triangular lattice with hexagonal symmetry. Since then, the study of complex plasma has come to a new era. It became a powerful tool to study generic process in classic gas, liquid, and solid. The research of complex plasma can be roughly divided into three catalogs: i) The interaction between microparticles and plasma [38]. ii) Complex plasma as a model system to study generic physics phenomena [20, 84]. iii) Applications in semiconductor production, fusion device, etc. [74, 113, 123]

There have been many reviews and books on the various experiments and theories of complex plasma published in the past decades [16, 38, 40, 41, 84, 114]. In this introduction, we only briefly introduce some basic theories, which are closely related to the studies included in this thesis.

¹ Strictly speaking, in a complex plasma, particle size could range from nanometers (e.g., particle growth) to several meters (e.g., space dusty plasma). However, in laboratory experiments, particles in micrometer range are most widely used. For the purpose of distinction from ion, electron particles and neutral gas molecules, these particles are generally called microparticles in this thesis regardless their real size.

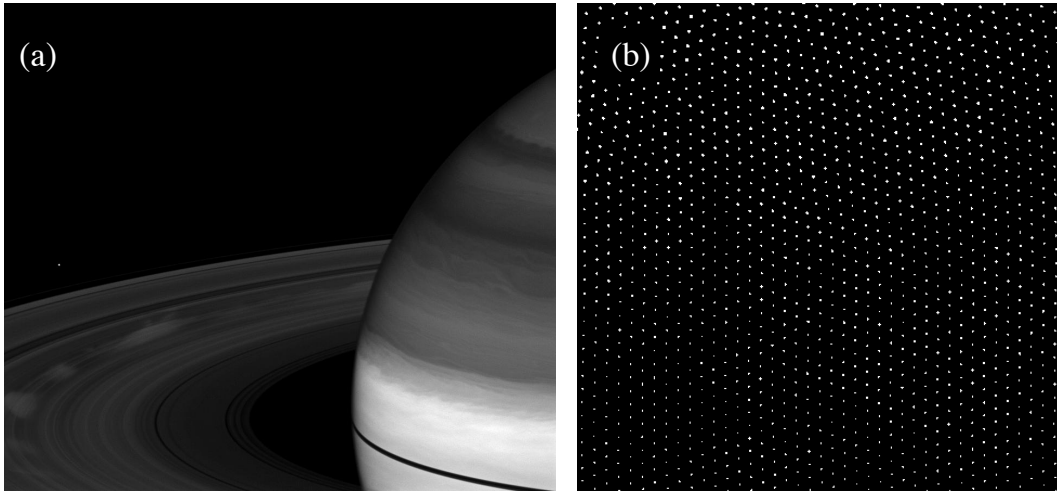


Figure 1.1: Two important discoveries for the complex plasma research: (a) The observation of the spokes in Saturn’s B ring. The image was taken with the Cassini spacecraft wide-angle camera in 2009. Credit: NASA/JPL/Space Science Institute; (b) The experimental realization of two-dimensional plasma crystal. The experiment shown here was performed in a rf discharge in a Gaseous Electronic Conference (GEC) reference cell. Individual particle positions (bright dots) are recorded by a complementary metal-oxide semiconductor (CMOS) camera with laser illumination techniques. Microparticles are confined in a single layer in the (pre)sheath above bottom electrode and self-organize in a triangular lattice with hexagonal symmetry.

1.1 RF discharge and plasma diagnostics

It is generally important to understand the generation and the basic properties of pure plasma – the background medium of complex plasma, before we start to study more sophisticated features of complex plasma. Plasma is one of four classical states of matter. As we all know, a solid substance generally passes to a liquid state and further passes to a gas state as the temperature increases. At a sufficiently high temperature, the molecules in the gas decompose to form a gas of atoms that move freely in random directions². If the temperature is further increased, some of the atoms decompose into freely moving charged particles (electrons and ions), and the substance enters the plasma state [77].

In all the experiments presented in this thesis, plasmas are generated by radio frequency (rf) discharge. In order to ignite the plasma, a strong electric field is necessary to accelerate the seed electrons³. These electrons with a high kinetic energy ionize a fraction of the

² Collisions between atoms are infrequent.

³ These seed electrons can be created by the ionization by cosmic x-ray background or emission from the rough surface by electric field [96].

neutral gas and the plasma is created. However, once the plasma is ignited, the voltage to maintain such a rf discharge could be reduced to a relative low value because the electron loss, which is only caused by diffusion to the chamber surface, is not intense and thus such a high ionization rate as in the ignition phase is not required in the maintenance phase. Compared with direct current (dc) discharges, rf discharges are more efficient and need smaller maintain voltage [19, 77].

In our experiments, we used a capacitively coupled rf discharge. The plasma is created by applying an radio frequency electric field between two electrodes. There are three chambers involved in this thesis. The size, shape, and the way they are powered are different from chamber to chamber. We will introduce them in more detail in the corresponding chapters.

It is important to obtain the basic parameters of the plasmas for the experimental analysis. There are several ways to achieve this purpose. Basically we can categorize them into three methods: equivalent circuit approach, direct measurements, and numerical simulations.

1.1.1 Equivalent circuit approach

The basic concept of equivalent circuit approach is to divide the complete discharge circuit into several sections, including bulk plasma and sheath region. For a homogeneous model, some assumptions are made [43]: Firstly, the ions respond only to the time-averaged potentials and the electrons respond to the instantaneous potentials and carry the rf discharge current. Secondly, the electron density is zero within the sheath regions. Thirdly, there is no transverse variation (along the plates). Lastly, the ion density is uniform and constant in time everywhere in the plasma and sheath regions.

With these assumptions, we can convert the bulk plasma and sheath region to some combinations of electronic components in the circuit, see Fig. 1.2(a). For example, the admittance of the bulk plasma can be expressed analytically as [77]

$$Y_p = i\omega_{rf}C_0 + \frac{1}{i\omega_{rf}L_p + R_p}, \quad (1.1)$$

which is in fact a series combination of inductor $L_p = \omega_{pl,e}^{-2}C_0^{-1}$ and a resistor $R_p = \nu_{en}L_p$ in parallel with a capacitor $C_0 = \epsilon_0 A/d$, where $\omega_{pl,e}$ is electron plasma frequency, ω_{rf} is rf frequency, ν_{en} is electron neutral collision frequency and A is the area of the electrode. Likewise, we can also describe the sheath region analytically (even more complicated) and complete the circuit. The model is qualitatively correct and introduced to describe the underlying physics and the procedures of real discharges. However, due to some unrealistic assumptions, it cannot be used to describe the quantitative behavior of real discharge.

One improvement of this mode is to take into account the inhomogeneity of the plasma and the sheath, so called inhomogeneous model. The facts that the ion density decreases within the sheath and the boundary collects particles lead to a Child law variation of

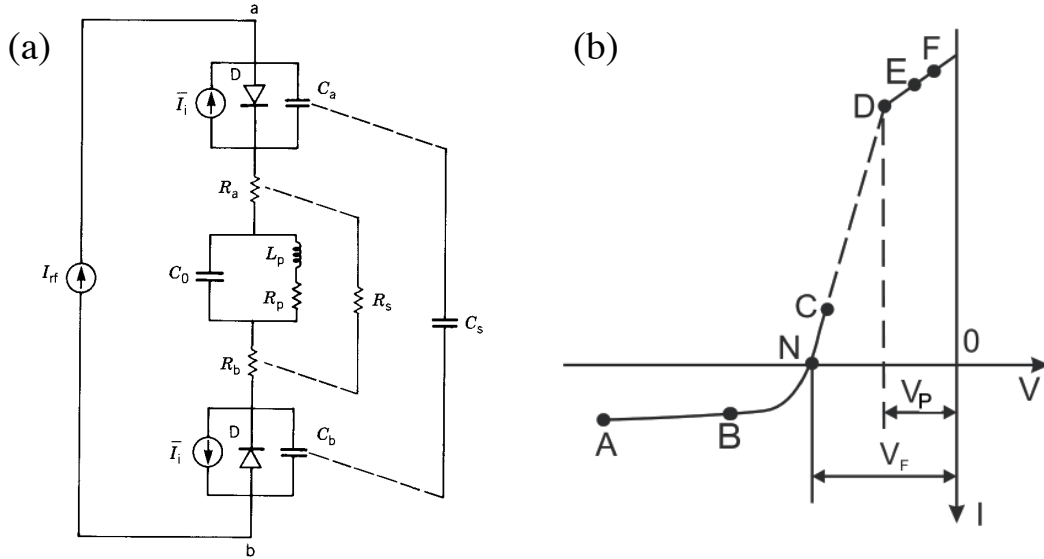


Figure 1.2: RF plasma and plasma diagnostics: (a) Nonlinear circuit model of the homogeneous rf discharge in the equivalent circuit approach. Reproduced from Ref. [77]. I_{rf} is the rf current, \bar{I}_i is equivalent dc current sources, C_0 is the vacuum capacitance, L_p is the plasma inductance, and R_p is the plasma resistance. The dashed lines indicate that the series connection of the nonlinear sheath capacitors C_a and C_b , and resistance R_a and R_b , yield the corresponding linear sheath capacitor C_s and resistance R_s , respectively; (b) The typical current-voltage characteristic in probe measurement. Reproduced from Ref. [5]. V_p is the plasma potential and V_F is the floating potential. Section AB and EF represent saturation regimes, where probe voltage is negative and positive to the plasma potential, respectively. By measuring the slope in section CD , electron temperature of the plasma can be estimated.

the density [77]. This further complicates the model but makes the model sensible for quantitative comparison with the real situation. By solving a complete set of equations with some basic input conditions, one can practically estimate the plasma parameters for the purpose of plasma diagnostics.

The drawbacks of this model is obvious. The model is rather complicated even in the simplest plane-parallel geometry. Quite a lot of assumptions are made for the purpose of simplicity, some of which are not quite realistic⁴.

1.1.2 Probe measurement

The electric probe method of plasma diagnostics is widely used for studying the parameters of gas discharges [3, 29, 73, 85]. An electric probe is a small metallic electrode immersed

⁴ E.g., the electron density is zero in the sheath, which is not true in reality.

into a plasma. The probe is connected to a power supply and the different voltage V can be input on the probe. By measuring the current I (current-voltage characteristic), as shown in Fig. 1.2(b), one can estimate the plasma parameters.

The current-voltage characteristic can be interpreted as follows [5]: If the probe has the same potential as the plasma (point D), it mainly collects electron current due to the high thermal velocity of electron. If the probe is positive with respect to the discharge, the electrons are accelerated to the probe and ions are retarded. The current increases until saturation of the electron current occurs (section EF), i.e., the negative space charge at the probe surface rises until it is equal to the positive charge of the probe. When the probe is negative with respect to the plasma, the electrons are repelled and ions are attracted. The current decreases with the decrease of voltage until the voltage is so low that all electrons are repelled (saturation state, section AB).

The plasma parameters can be derived directly from the measured characteristics described above. For example, by measuring the angle α of the slope of the linear part of current-voltage curve (section CD), the electron temperature can be estimated:

$$T_e = \frac{e}{k_B} \frac{1}{\tan \alpha}. \quad (1.2)$$

The advantage of probe method is that the diagnosis can be performed using relatively simple apparatus. It can measure local plasma parameters with relatively high spatial resolution. However, this method is not applicable for *in situ* measurement in complex plasma experiments since the probe disturbs not only the local plasma but also the suspended particles. An alternative method, i.e., optic measurement, can to some extent overcome this drawback. However, the spectrometer collects the light in a certain volume. It obtains an average value of the plasma parameters within this certain volume and thus does not have a high spatial resolution.

1.1.3 Particle-in-cell simulation

Comparing to two methods introduced above, particle-in-cell (PIC) simulation provides plasma parameters in a high spatial and time resolution. It is a standard particle-based simulation⁵ widely used in plasma research. It employs the fundamental equations without much approximation, allowing it to retain most of the physics [13, 61, 112, 122].

The fundamentals of PIC are briefly introduced [126]: In the PIC scheme particles including ions and electrons⁶ are defined in continuum space in both position and velocity. Fields are defined at the grid vertices in space. However, both fields and particles are defined at discrete times. Starting from the input initial conditions, particle positions and velocities advance one time step based on the particle equation of motions and fields interpolated from the discrete grid to the continuous particle locations. Next, particle

⁵In contrast to the simulation based on the fluid model.

⁶Here the concept of superparticle is employed. Each superparticle consists a certain number of real particles, having a collective mass and charge.

boundary conditions such as absorption and emission are applied. If the model is collisional, the Monte Carlo collision (MCC) scheme is employed [124, 125]. Source terms including density ρ and current J for the field equations are accumulated from the continuous particle locations to the discrete grid vertices. The fields then advance one time step, and the time step loop repeats.

Despite having many advantages, the PIC simulations have some weaknesses. The grid size limits the spatial resolution of the simulation. It is challenging to simulate a system with a large range of time scale. Complex plasma is such kind of system since the time scale of microparticles is much slower than that of ions and electrons. This brings huge difficulties to simulate a complete complex plasma system using PIC method. Last but not least, the simulation requires a significant computational power. In contrast, simulation based on the fluid model has a higher efficiency [79]. However, the results are reliable only if the particle (ion, electron) density is high in the system. In a low pressure plasma discharge, it is normally not the case.

In the works presented in this thesis, plasma parameters are obtained only by numerical simulations. For measuring the particle charge in the deep sheath presented in Chapter 2, the plasma parameters in the sheath are extracted from an one-dimensional PIC simulation. For the investigation on lane formation under microgravity conditions in Chapter 5, the plasma parameters are obtained from a commercialized simulation code SIGLO-2D based on the fluid model [120].

1.2 Charging of particles in complex plasmas

Charging mechanism plays a central role in the research of complex plasmas [38, 67]. The particle charge determines the magnitude of interaction between particles as well as external force exerted on the particle, e.g., electric force. It is the fundament for the further study on different phenomena in complex plasmas.

The major mechanism of charging in a plasma is the particle current absorption on the microparticle surface. In the plasma, both electrons and ions move towards the surface of microparticles. Due to high thermal velocity, electrons reach the microparticles much more rapidly than the ions. Thus, the microparticles acquire more electrons than ions and their surface potential becomes negative. The particle charge reaches a stationary state as ion current and electron current are balanced. The evolution of the charge on a microparticle is governed by the equation [38]

$$\frac{dQ_p}{dt} = I_i + I_e, \quad (1.3)$$

so that the stationary charge is determined from the current balance:

$$I_i + I_e = 0, \quad (1.4)$$

where $I_{(i)e}$ is ion(electron) current to the surface of microparticle.

1.2.1 Charging in isotropic plasmas

Since the major mechanism of charging in a plasma is current absorption, the central question of estimating the surface charge is to calculate the ion and electron current toward the surface of microparticles. One of the most widely used theory to describe the charging procedure of particles in a complex plasma is the orbit motion limited (OML) approximation [1]. This approach deals with collisionless electron and ion trajectories in the vicinity of a microparticle⁷ and determines the collection cross section. The ion and electron current can be expressed as follows⁸:

$$I_i = 4\pi r_p^2 n_i e \left(\frac{k_B T_i}{2\pi m_i} \right)^{1/2} \left(1 - \frac{e\phi_p}{k_B T_i} \right), \quad (1.5)$$

and

$$I_e = 4\pi r_p^2 n_e e \left(\frac{k_B T_e}{2\pi m_e} \right)^{1/2} \exp \left(\frac{e\phi_p}{k_B T_e} \right), \quad (1.6)$$

where r_p is radius of particle, $n_{i(e)}$ is ion(electron) density, e is an elementary charge, $T_{i(e)}$ is ion(electron) temperature, $m_{i(e)}$ is ion(electron) mass, and ϕ_p is particle floating potential.

However, as mentioned above, OML approach is only applicable for collisionless regime of the plasma particles. If we take ion-neutral collisions into account, the ion orbital motion will be destroyed. When an orbiting ion collides with an atom in the vicinity of the microparticle (perturbed plasma region), it will lose energy and be trapped in the region of negative potential. As result, ion current to the microparticle will increase.

For a weakly collisional regime ($l_i \geq R_0$ where l_i is ion mean free path), ion current to a microparticle [72] is composed of the random ion current into the perturbed region and the ion current determined by OML approach with different weighting. Here we define R_0 as the relevant length scale for the perturbed plasma region. Beyond the sphere of radius R_0 the plasma density is weakly perturbed. If we assume Maxwellian velocity distribution for the ions in this region, the random current into the perturbed region is given by

$$I_{R_0} \approx 4\pi R_0^2 n_i e \left(\frac{k_B T_i}{2\pi m_i} \right)^{1/2}, \quad (1.7)$$

and the total ion current can be written as

$$I_i \approx (1 - R_0/l_i) I_{OML} + (R_0/l_i) I_{R_0}, \quad (1.8)$$

where I_{OML} is the ion current given by OML approach.

However, if we consider the microparticle immersed in a strong collisional plasma ($l_i \ll R_0$), the ion motion to the microparticle is determined by mobility. Even in this case, the electrons can still be collisionless because the characteristic cross section for electron-neutral collision is much smaller than that for ion-neutral collision. A number of investigations have been dedicated to solving the charging problem in strong collisional regime. More detail on this topic can be found in the references [17, 36, 38, 68].

⁷ Mean free path of the plasma particle is much longer than plasma screening length [44].

⁸ Here we assume the ion has one positive elementary charge.

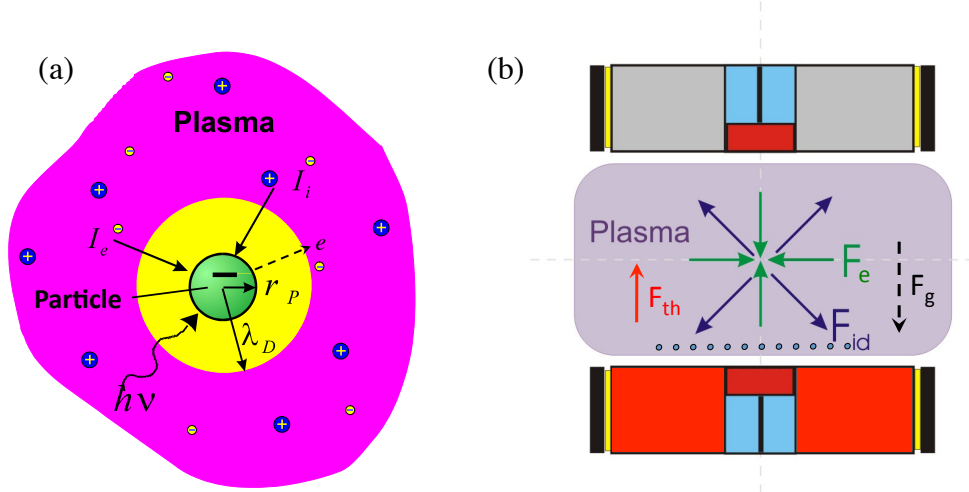


Figure 1.3: Charging and force of microparticle in plasmas: (a) Illustration of charging mechanism of a single microparticle with a radius of r_p in plasmas. Ion current I_i and electron current I_e reaches balance at the surface of microparticle. Secondary emission and thermionic emission occur when the microparticle is impacted by energetic plasma particles and heated, respectively. By absorbing high energy photons $h\nu$, photon emission can lead to a positive charge of a microparticle; (b) Demonstration of various forces exerted on a microparticle in a discharge. The chamber shown in the figure is PKE device, which is originally designed for the experiments onboard the International Space Station (ISS). In such chamber, particles experience ion drag force F_{id} and electric force F_e (magnetic force F_m is negligible in this device). If the experiment is not performed on the orbit, gravity should be taken into account. Besides, if we heat the bottom electrode and cool the top electrode, thermophoretic force directs along the temperature gradient. Note that neutral drag, which depends on the relative speed of microparticle to the neutral gas, is not shown in the picture. Courtesy of H. Thomas.

1.2.2 Charging in anisotropic plasmas

In the laboratory experiment on the ground, particles are normally levitated in the sheath where plasma is no more isotropic. In such area the ions have a finite drift. This can in turn affect particle charging mechanism by changing the hitting cross sections and the velocity distribution functions of the ions.

The ion current [114] can be expressed as

$$I_i = 4\pi r_p^2 e n_i \left(\frac{k_B T_i}{2\pi m_i} \right)^{1/2} \left[F_1(u_0) - F_2(u_0) \frac{e\phi_p}{k_B T_i} \right], \quad (1.9)$$

where $F_1(u_0) = (\sqrt{\pi}/4u_0)(1 + 2u_0^2)\text{erf}(u_0) + (1/2)\exp(-u_0^2)$ and $F_2(u_0) = (\sqrt{\pi}/2u_0)\text{erf}(u_0)$ are written in terms of the error function $\text{erf}(u_0) = (2/\pi) \int_0^{u_0} \exp(-t^2) dt$ and $u_0 = v_{i0}/V_{T_i}$. Here v_{i0} denotes ion drift velocity and V_{T_i} denotes ion thermal speed. If we express functions F_1 and F_2 around $u_0 = 0$ by Taylor series, both of them approach unity as $u_0 \rightarrow 0$. As a

result, Equation 1.9 reduce to Equation 1.5 if ion drift speed is much smaller than ion thermal speed ($u_0 \ll 1$). On the other hand, if ion drift speed is much greater than ion thermal speed ($u_0 \gg 1$), the ion current can be approximated as

$$I_i = 4\pi r_p^2 e n_i v_{i0} \left(1 - \frac{2e\phi_p}{m_i v_{i0}^2} \right). \quad (1.10)$$

Again we have to point out that the results are obtained on the basis of OML approach in which no ion-neutral collision is taken into account. The ion current would be dramatically different for the collisional regime.

1.2.3 Some other charging mechanism

The collection of ions and electrons from the plasma is not the only possible charging mechanism. Electrons can also be emitted from the particle surface due to secondary emission, thermionic emission, etc. These processes are only briefly mentioned for completeness, since they are not relevant to the thesis.

Secondary emission

When the energetic primary plasma particles (ions and electrons) fall onto the surface of a microparticle, energy will be released to excite the electrons which can be emitted from the particle surface. Two processes are involved: one by electron impact and the other by ion impact. When an energetic electron approaches the particle surface, it might enter into the microparticle and even passes through the whole particle. During the procedure electron loses its energy and a portion of this energy might be enough to excite other electrons which may in turn escape from the microparticle [23]. Such behavior can happen also with energetic ion impact. In addition, when an ion approaches the microparticle at low kinetic energies, it might be neutralized by the electrons which tunnel through the potential barrier. The energy released in this process also may excite additional electrons which can be emitted from the particle surface [31].

Thermionic emission

When a microparticle is heated to a high temperature, electrons and ions might be thermionically emitted from its surface. The thermionic emission may be induced by laser heating or by thermal infrared heating. This process plays a significant role in particle charging mechanisms which might cause the particle positively charged [102].

Photoemission

When a flux of photons with energy greater than the photoelectric work function of the microparticle incidents on the surface of a microparticle, the latter emits photoelectrons. This mechanism depends on the wavelength of the incident photons, surface area of the

microparticle as well as the properties of the microparticle material. This mechanism tries to make the microparticle positively charged. [101]

1.3 Forces on particles in complex plasmas

In laboratory complex plasmas on the ground, there are several different forces acting on an isolated charged microparticle, e.g., gravitational force, ion and neutral drag force, electromagnetic force, etc. These forces govern the dynamics of microparticles immersed in plasmas. One can express the dynamics of a microparticle as follow:

$$m_p \frac{d\mathbf{v}_p}{dt} = \mathbf{F}_g + \mathbf{F}_{id} + \mathbf{F}_{nd} + \mathbf{F}_{em} + \mathbf{F}_{th}, \quad (1.11)$$

where m_p and v_p are the mass and velocity of the microparticle, respectively, \mathbf{F}_g is the gravitational force, \mathbf{F}_{id} and \mathbf{F}_{nd} are the ion and neutral drag force respectively, \mathbf{F}_{em} is the electromagnetic force and \mathbf{F}_{th} is the thermophoretic force. Besides the forces mentioned above, there are also electron drag force and radiation pressure force acting on the microparticle. Concerning electron drag force, in rf discharges, where ions and electrons have the similar drift speed due to ambipolar diffusion [21], this force is usually ignored because the electron-to-mass ratio is quite small. As to radiation pressure force, which is induced by the momentum exchange between particle radiation, or laser beam, and the microparticle, it also can be neglected if we do not focus the laser beam on one microparticle. Thus, in the next sections we will just discuss the former five forces.

1.3.1 Gravitational force

In ground-based experiments the gravitational force $\mathbf{F}_g = m_p g$ usually plays an important role. In order to suspend the microparticles, there should be other forces which can compensate the gravitational force. The electric force which is induced by the electric field in the (pre)sheath of the plasma can provide the balance. That's why in many experiments on the ground, microparticles are levitated close to the lower electrode. Besides, one can always apply an external electromagnetic force or a thermophoretic force to levitate the microparticles in different height inside discharge chamber.

1.3.2 Ion drag force

The ion drag force is caused by the momentum transfer from the ion flow to the microparticles [114]. This momentum transfer can be achieved in three different ways. Firstly, the ions transfer momentum to a microparticle through direct impacts. Secondly, the ions transfer momentum through Coulomb collisions with the charged microparticles. Thirdly, the ion flow exerts a collective effect by modifying and distorting the shape of the Debye sheath around the microparticle, making it asymmetrical⁹. Therefore, the total ion drag

⁹ Since Northrop et al. [90] showed that this collective effect has only a minor effect on the total ion drag force, we can neglect this term and calculate the remaining two terms.

force can be expressed as

$$\mathbf{F}_{id} = \mathbf{F}_{id}^{coul} + \mathbf{F}_{id}^{coll}, \quad (1.12)$$

where F_{id}^{coul} is the ion drag force caused by Coulomb collision and F_{id}^{coll} is the ion drag force caused by ion collection.

By using the laws of conservation of energy and angular momentum [15], one can estimate the momentum transfer cross section for the Coulomb drag and further estimate the Coulomb ion drag force [89]

$$\mathbf{F}_{id}^{coul} = 2\pi b_0^2 n_i m_i V_{it} \mathbf{v}_i \left(\frac{b_0^2 + \lambda_{De}^2}{b_0^2 + b_c^2} \right). \quad (1.13)$$

where $b_0 = r_p \frac{e\phi_p}{k_B T_i}$ is the impact radius corresponding to a 90° deflection and $b_c = r_p \left(1 - \frac{e\phi_p}{k_B T_i}\right)$ is the hitting collision impact parameter, and $V_{it} = (\mathbf{v}_i^2 + 8k_B T_i / \pi m_i)^{1/2}$ is the total ion speed, which is a combination of average ion drift speed and thermal speed.

On the other hand, concerning collection force, we assume that the momentum transfer cross section for the collection drag is equal to the cross section used for the ion charging current. Therefore, the collection force can be expressed as

$$\mathbf{F}_{id}^{coll} = n_i m_i V_{it} \pi r_p^2 \mathbf{v}_i \left(1 - \frac{e\phi_p}{k_B T_i} \right). \quad (1.14)$$

However, the standard theory of Coulomb scattering used in calculating ion drag force usually fails for the ion-grain elastic collision. Taking into account the moderate coupling between ions and microparticles [65] and ion-neutral collision [53], an extended approach has been recently developed which predicts a substantial enhancement of the ion drag force. It is later shown experimentally that the effect of ion-grain coupling is apparently more important than that due to ion-neutral collisions under many typical experimental conditions [129]. This discovery might be quite important for understanding of some basic processes in complex plasmas, e.g., the void formation, wave propagation, long-range interactions, etc.

1.3.3 Neutral drag force

The neutral drag force can be defined as the rate of momentum exchange between the microparticles and neutrals during their collision. To estimate the neutral drag force, there are two regimes to be considered [114, 89], i.e., the hydrodynamic regime ($Kn \ll 1$) and the kinetic regime ($Kn \gg 1$). In the hydrodynamic regime, the neutral drag force can be estimated from Stokes's law and is found to be proportional to the speed and radius of the microparticle. On the other hand, in the kinetic regime, classical gas theory may be used and Baines et al. [9] obtained two slightly different analytic expressions for the neutral drag force depending on the assumption concerning the nature of the collision, i.e., specular and diffuse.

When the relative speed is very small in comparison with the neutral thermal speed, the result can be described by Epstein expression [34]:

$$\mathbf{F}_{nd,r} = -\delta_{Ep} \frac{8}{3} \sqrt{2\pi} r_p^2 m_n n_n V_{T_n} (\mathbf{v}_p - \mathbf{v}_n), \quad (1.15)$$

where $V_{T_n} = \sqrt{T_n k_B / m_n}$ is neutral thermal speed, m_n is mass of single atom and n_n is the density. Depending on the collision mechanism, the Epstein coefficient is 1 for specular reflection and $1 + \pi/8$ for diffusive reflection.

In reality, the Epstein coefficient also depends on the microparticle material and other conditions. According to the measurement with a laser acceleration method, the Epstein coefficient is $\delta_{Ep} = 1.26 \pm 0.13$ for melamine-formaldehyde (MF) microparticles [78]. On the other hand, using horizontal oscillation method, Konopka measured the coefficient to be $\delta_{Ep} = 1.48 \pm 0.05$ [70]. In this thesis, we use the measurement result given by Konopka.

1.3.4 Electromagnetic force

The electromagnetic force \mathbf{F}_{em} acting on a moving charged microparticle of charge Q_p is the sum of the electric force

$$\mathbf{F}_e = Q_p \mathbf{E}, \quad (1.16)$$

and the magnetic force, i.e., Lorentz force,

$$\mathbf{F}_m = \frac{Q_p}{c} \mathbf{v}_p \times \mathbf{B}, \quad (1.17)$$

where \mathbf{E} is the electric field and \mathbf{B} is the magnetic field.

In the ground-based experiments magnetic force is insignificant if we do not apply an external magnetic field. Therefore here we concentrate on the electric force that a conducting microparticle feels in a plasma in the presence of a presheath field in the discharge. To calculate such an electric force acting on a microparticle in the presence of electric field directing in z direction, one should solve the linear Poisson equation in spherical coordinates with an azimuthal symmetry [114]. Here we give the final expression:

$$F_{e_z} = Q_p E_0 \left[1 + \frac{k_D^2 r_p^2}{3(1 + k_D r_p)} \right]. \quad (1.18)$$

Note that the constant electric field E_0 is along the z direction. This result implies that for most of the complex plasma in which $k_D r_p \ll 1$, where $k_D = 1/\lambda_D$ and λ_D is the Debye length, we have $F_{e_z} = Q_p E_0$. In other words, the plasma does not shield the microparticle from the bulk electric field and reduce the electrostatic force.

1.3.5 Thermophoretic force

We consider a microparticle that resides in a neutral gas with a temperature gradient ∇T_n . The molecules on the hot side of the particle have higher thermal speeds than those on the

cold side. Since the momentum transfer rate from the gas to the microparticle depends on the speed of the molecules, this asymmetry momentum transfer cause a thermophoretic force, which is directed towards lower gas temperature [114, 103]. In the case that the gas and dust have temperature less than $500K$, the thermophoretic force can be expressed as [118]

$$\mathbf{F}_{th} \approx \frac{5}{4\sqrt{2}} \left(\frac{r_p}{\sigma_{Lj}} \right)^2 k_B \nabla T_n. \quad (1.19)$$

This expression shows that the thermophoretic force depends on the particle radius r_p , gas type σ_{Lj} and temperature gradient ∇T_n , but does not depend on the gas pressure and average temperature.

1.4 Complex plasma as soft matter

The term ‘‘soft matter’’ describes a class of material that is supramolecular, exhibits macroscopic softness, and has metastable states and a sensitivity of their equilibrium to external conditions [60]. Such materials typically have energies of about room temperature, i.e., they are far away from quantum states.

Complex plasma is exactly such kind of system [20, 84]: The microparticles serve as supramolecular in the system which obey classical mechanics. Waves can be excited by external disturbance and propagate in the medium, which shows its macroscopic softness [82, 97, 111]. The co-existence of crystalline state and glassy state corresponds to the metastable state of the system [54]. A complex plasma system is sensitive to the external confinement such as boundary of the discharge chamber [6, 93].

In complex plasmas, the interaction between microparticles i and j can be well described by screened (Yukawa) Coulomb interaction:

$$\phi_{ij} = \frac{Q_i Q_j}{r_{ij}} \exp\left(-\frac{r_{ij}}{\lambda_D}\right) \quad (1.20)$$

where r_{ij} is the interparticle distance, and the Debye length in the bulk plasma can be approximated by ion Debye length

$$\lambda_D \approx \sqrt{\frac{k_B T_i}{4\pi e^2 n_i}} = \lambda_{Di} \quad (1.21)$$

since the electron temperature is much higher than the ion temperature. On the contrary, in the sheath area the ion stream is so fast that the Debye length results from electron Debye length. The Yukawa interaction will be modified if we take into account the ion-neutral collision effect. Long range attraction due to ion shadowing can exist if certain threshold condition can be satisfied [66]. But under normal conditions, Yukawa interaction is a good approximation within a microparticle cloud.

In a complex plasma, the rate of momentum exchange through interactions between the microparticles can be much larger than that through other means, such as ion drag. Therefore, the microparticles alone can be treated as essentially independent system regarding

their dynamics¹⁰. Assuming the microparticles in the system are equally charged with Q , the coupling strength of such system is defined as the ratio of the Coulomb interaction between particles to the kinetic energy [114]:

$$\Gamma = \frac{Q^2}{k_B T_p \Delta} \exp\left(-\frac{\Delta}{\lambda_D}\right), \quad (1.22)$$

where Δ is the interparticle distance of the system and T_p is the temperature of microparticles¹¹. If Γ exceeds unity, we call the system a strongly coupled system. Together with screening parameter $\kappa = \Delta/\lambda_D$, a phase diagram of a Debye-Hückel system is obtained by numerical simulation. The complex plasma system can exist either in solid state or in liquid state. At low Γ ($1 \lesssim \Gamma \lesssim 175$), system is always in liquid state while at high Γ ($\Gamma > 175$), system can exist in solid state with either body centered cubic (bcc) structure or face centered cubic (fcc) structure [109].

Comparing to other soft matter, complex plasma has several remarkable features. Dynamical time scale associated with microparticles is stretched to tens of millisecond¹². The background gas is dilute so that particle dynamics in strongly coupled complex plasmas is virtually undamped. All these features make complex plasma a powerful tool to study regular liquid and solid at the kinetic level [84].

1.4.1 Binary complex plasma and non-additivity

A binary mixture is a system comprising two different species of particles. Comparing to a single species system, it has a more complicated structure and dynamics properties. In the study of binary mixtures in numerical simulations, glassy state has been discovered [7, 62]. In the study of alloy, by introducing a second species into the base of the metal, the mechanical properties can be altered [22].

Recently complex plasma with more than one type of microparticles¹³ mixed together has drawn more and more attention. Strictly speaking, the study of Mach cone induced by an extra particle is also one type of binary complex plasma study [105]. So is “channeling” effect, which will be introduced in Chapter 4 in detail. However, in a more general sense, we confine the binary complex plasma study to a mixture of two groups of particles with different properties such as size and mass. With such system, we can study different phenomena including phase separation and lane formation [58, 117].

In a binary complex plasma, one feature is very important – so called non-additivity. For both large and small particles in the binary mixture of complex plasmas we assume that they can be treated as point-like and that their electric potential is screened exponentially with the same screening length λ_D (plasma screening length), but different interaction

¹⁰ However, at large pressures ($P \gtrsim 50$ Pa for example) the neutral friction becomes important [64].

¹¹ Temperature represents the kinetic energy (not the surface temperature of the particle).

¹² In colloidal suspensions, the dynamical time scale can be a few weeks.

¹³ In the sense of particles of different sizes or materials.

magnitudes ε_{ij} . The general form of inter-particle interaction can then be written as

$$\phi_{ij}(r) = \varepsilon_{ij} \frac{\exp(-r_{ij}/\lambda_D)}{r_{ij}}. \quad (1.23)$$

For like particle interaction, $\varepsilon_{ij} = \varepsilon_{SS/LL}$ is the product of the effective charge and the real charge $Z_{S/L}$ [55] (subscripts S and L denote small and large particles respectively). According to the Lorentz-Berthelot mixing rules [4] for the interaction between unlike particles one gets:

$$\varepsilon_{ij} = \varepsilon_{LS} = \varepsilon_{SL} = (1 + \delta) \sqrt{\varepsilon_{SS}\varepsilon_{LL}}. \quad (1.24)$$

δ is the non-additivity parameter¹⁴ [55], which represents the asymmetry in the mutual interaction between unlike particles. δ is always positive in binary complex plasmas [55]. Our model reduces to a typical Yukawa potential when $\delta = 0$, which is the exact interaction model adopted in Ref. [117].

1.4.2 Channeling effect

When a charged particle is incident upon an anisotropic solid target such as crystalline, the physical processes are very strongly dependent on the orientation of the momentum of the particle relative to the crystalline axes or planes. This phenomenon is called channeling effect [35].

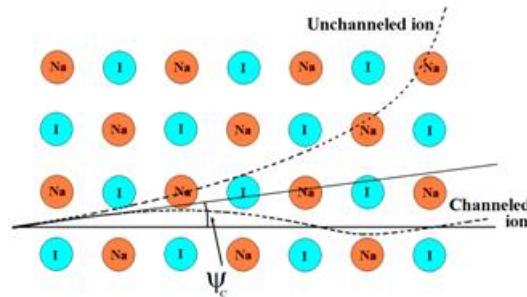


Figure 1.4: Illustration of channeling effect in a sodium iodide (NaI) crystal: Ions move in a crystal in a different way than in amorphous materials. In particular in the case of motion along crystallographic axes and planes, the so-called “channeling” effect can occur. Ψ_c is the scattering angle of the ion in the channel. (Credit: the DAMA Project)

There are several situations: i) If the orientation of the momentum of the incident charged particle lies close to a major crystal direction, the particle will suffer a small-angle scattering as it passes through several layers of atoms in the crystal. ii) If the orientation of the momentum of the incident charged particle lies close to crystalline plane (not close to the major crystalline axes), the situation should be further divided into two cases. If

¹⁴ In the attached paper No. 5, non-additivity is represented by Δ .

the incident particle is positive charged as the atom nuclei in the crystalline plane, it is repelled by the closest plane and move towards the neighboring planes. However, for the same reason it will also be repelled by the second plane back toward the first plane. In fact, the particle's motion is confined in the space between two neighboring crystalline planes, which is known as the classic situation of channeling. On the contrary, if the incident particle is negative charged, opposite to the charge of nuclei in the crystalline plane, it is attracted to the plane and thus move along the plane. It is known as "plane channeling". In the latter case, the probability of "dechanneling" is much higher than the earlier case due to the high density of atomic nuclei¹⁵ in the plane.

Channelling effects can be used as tools to investigate the properties of the crystal lattice that is not accessible to X-rays. At higher energies (tens of GeV), the applications include the channelling radiation for enhanced production of high energy gamma rays [63], and the use of bent crystals for extraction of particles from the halo of the circulating beam in a particle accelerator [12, 14].

1.4.3 Lane formation

When two different species of particles are driven into each other, particles of the same species form a stream line and move collectively in a lane. At encounter of the front of two particle cloud, particles interpenetrate randomly. However, the particles will self-organize to follow the particles moving in front of them because this is energetically favorable. The non-additivity effect will weaken the formation of lanes but strengthen the phase separation.

As the ubiquitous prototype of non-equilibrium pattern formation, lane formation has drawn a lot of attention over the last decade. It is a generic process, which has been studied for mixtures in various branches of physics, for instance, in colloidal suspensions [33, 128, 76, 99, 127] and in molecular ions [87]. Besides physics, such process has also been studied in the context of self organization, for instance in biology [28] with traffic routes of army ants. Recently lane formation was also discovered in complex plasma experiments performed under microgravity conditions on board the International Space Station [117, 116], and further investigated with numerical simulations [57]. In this thesis, we comprehensively investigate lane formation under microgravity conditions in Chapter 5. The crossover from lane formation to phase separation is revealed in this study. We also present a model experiment of lane formation on the ground, which has several advantages over the experiments performed on ISS.

¹⁵ In other words, high probability to suffer a high angle Rutherford scattering.

Chapter 2

Particle charging

This chapter provides complementary information to the papers:

- T. Antonova, C.-R. Du, B.M. Annaratone, L.-J. Hou, R. Kompaneets, H.M. Thomas, and G.E. Morfill, *Microparticles deep in the plasma sheath: Coulomb “explosion”*, Phys. Plasmas 19, 093709 (2012) No. 1
- C.-R. Du, S.A. Khrapak, T. Antonova, B. Steffes, H.M. Thomas, and G.E. Morfill, *Frequency dependence of microparticle charge in a radio frequency discharge with Margenau electron velocity distribution*, Phys. Plasmas 18, 014501 (2011) No. 2

2.1 Objectives

Charge on the microparticles is one of the most important parameters to study various phenomenon in complex plasma. It directly determines the magnitude of particle interactions with ions and electrons, with electric potential and with other particles. Particle charge can be directly measured using collision of a pair of particles in the (pre)sheath area [71]. However, particle charge in the deep sheath is hard to measure. Under normal condition, particles can not be confined deep in the sheath because of strong electric field. Therefore collision method can not be used. Despite the existence of the charging theory in anisotropic plasmas [38], the plasma parameters deep in the sheath can not be directly measured by probe measurement. The experiment presented in the included paper No. 1 gives an unique opportunity to measure particle charge in the deep sheath directly.

In many circumstances, it is very difficult to measure the particle charge *in-situ* during the experiments or plasma processes. Therefore, it is quite necessary to develop reliable theories to estimate the particle charge based on given plasma parameters [1, 2]. Different charging mechanism has been discussed in the introduction part of this thesis. However, even within the frame of one single charging mechanism, different plasma conditions leads to different theoretical models. For example, in an anisotropic plasma, the peak of the electron (ion) velocity distribution is usually shifted to the flux velocity. If the gas pressure

is high, electron-neutral collision and ion-neutral collision should be taken into account. A global charging model applicable for all situations simply does not exist.

Although there exist plenty of charging models applicable for different plasma conditions, the dependence of particle charge on rf discharge frequency has been poorly studied. As we will see in Fig. 2.3, with the same input power, microparticles are levitated at different heights and the particle cloud configurations are also different in discharges excited with rf frequency of 13.6 MHz, 90 MHz, and 180 MHz. This implies that charge on the dust particle is different under these three situations. It is possible to estimate particle charge based on PIC simulation [50, 51, 52]. However, it is very time consuming to conduct the simulation and thus not very easy to implement in practice. Therefore, it is important to develop a simple model which is applicable for estimating particle charge in a plasma ionized at different frequencies. We present this study in paper No. 2 included in this chapter. The theoretical model is applicable for particle charging in a bulk plasma in the collisionless regime. In addition, this work also gives a hint how the charge varies with discharge frequency at different gas pressure regimes.

2.2 Methods

On one hand, the particle charge in the deep sheath is measured experimentally. Both PIC simulation and molecular dynamics (MD) simulation play a significant role in the experiment analysis. Despite the hybrid analysis method, it is straight forward to estimate the charge of microparticle. On the other hand, the charge in the bulk plasma is calculated using a simple theoretical model. Assuming the same plasma parameters, we can compare the dependence of particle charge on discharge frequency and gas pressure.

2.2.1 Measurement of particle charge in deep sheath

We performed our experiment in a rf discharge chamber, shown in Fig. 2.1. A rf signal is input to the top electrode to ignite and maintain a plasma. In addition, we install an adaptive electrode at the bottom of the discharge chamber. The adaptive electrode is composed of 38 independent segments, each of which can be driven by a rf or dc power. In the experiment presented here, only the center segment is powered by rf. Microparticles are injected into the chamber by the dispenser. They can be confined by this driven segment in the vicinity of the bottom adaptive electrode. As we switch off the segment, the particle cloud “explodes” due to mutual repulsion, as shown in Fig. 2.2. We call it a Coulomb “explosion”.

In the previous research [32], particle charge is derived in the late stage of the explosion. However, in the late stage, interparticle distance becomes larger so that the simplification of Coulomb interaction is not accurate. Furthermore, the assumption of spherical symmetry is not valid in the late stage due to the strong deformation of the cloud. Moreover the vertical expansion is mainly due to the charge variation and strong sheath electric field instead of mutual repulsion. Although the charge distribution along the height in the sheath was

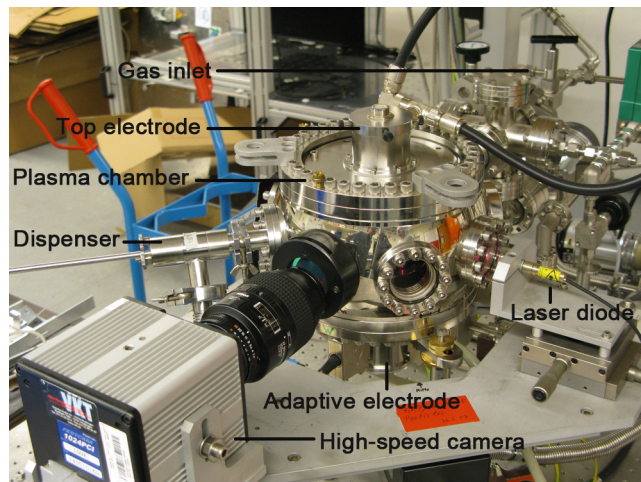


Figure 2.1: Photo of “adaptive” electrode chamber: The adaptive electrode is mounted at the bottom of the chamber. The top electrode is rf driven, generating the plasma filling the whole chamber (also see the sketch in Fig. 1 in the included paper No. 1). In the experiment we use argon for discharge. A high-speed camera (Photron FASTCAM 1024 PCI) is mounted in front of a window of the chamber with a filter, through which only the laser light shined by the laser diode can go through. Particles can be levitated in the plasma ball in the vicinity of adaptive electrode. Reproduced from Ref. [32].

calculated, the results deviate from MD simulation to a large extent. Therefore, a new approach is required to overcome these drawbacks stated above. In the current work, we focus on the initial stage of the explosion Fig. 2.2(b)-(d). As we see the results from the PIC simulation in paper No. 1, only at the deep region of the sheath (high Mach number) at low pressure, Coulomb interaction is an appropriate approximation as the particle cloud is still dense¹. Based on the horizontal motion of particles, combined with PIC simulation and MD simulation, the particle charge can be estimated where the particles are still located in the deep region of the sheath.

For simplicity we applied a 1D PIC simulation code to obtain the basic plasma parameters in the sheath region. The general flow of the PIC scheme is described in the Chapter 1. For the purpose of diagnostics in our case, we apply the boundary condition extracted from experiment. The initial condition is obtained based on earlier probe measurement in the same chamber. The system reaches a stable condition eventually and we extract the basic plasma parameters in the sheath. It turns out that our assumption of Coulomb interaction is rather reasonable at the deep region of the sheath. The simulation also provides an electric field distribution for further MD simulation.

The MD simulation used in this work is well described in Ref. [32]. However, we don’t use the linear approximation of the sheath field since a more accurate distribution is available from PIC simulation. In practice, we compare two cases with and without

¹ The cloud size is much smaller than the Debye length.

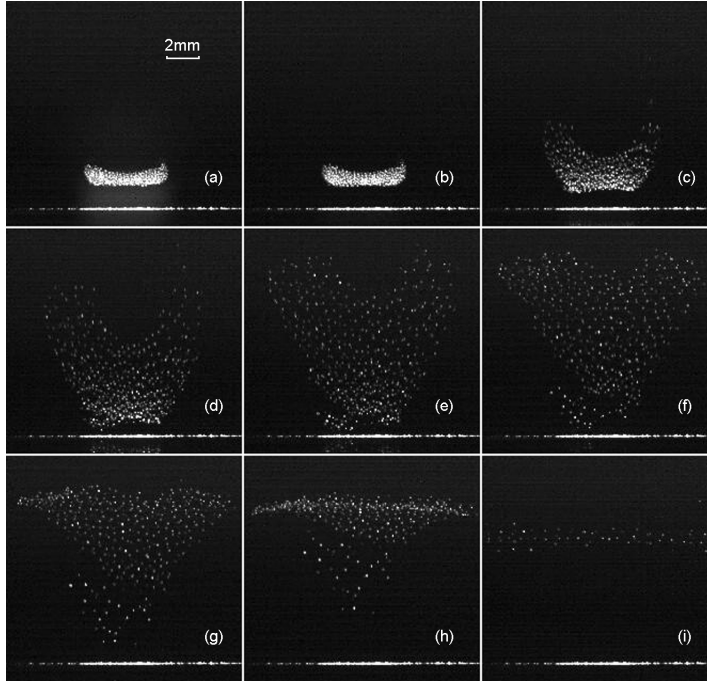


Figure 2.2: Process of Coulomb explosion experiment: Picture (a) shows the dust cloud profile before expansion. Picture (b) to (g) shows the expansion process with an time interval of 6.7 ms (20 frames) between each two pictures, where picture (b) is the first frame of expansion. Picture (i) shows the profile of the dust cloud at 440 ms after the beginning of the expansion. Reproduced from Ref. [32].

the presence of the vertical electric field. The results show difference only in the vertical expansion. There is no substantial difference on the horizontal velocity of the particles at the initial stage of the explosion. As we fit the simulation to the experiment results, we can estimate the particle charge in a good accuracy.

2.2.2 Model of particle charging with various discharge frequencies

The OML theory is a classic method to estimate the charge of a microparticle in an isotropic plasma in the collisionless regime [1]. Assuming Maxwellian velocity distribution for both ions and electrons, one can easily calculate the particle floating potential (proportional to the particle charge) based on the balance of ion and electron fluxes directed towards the particle surface. However, the Maxwellian distribution is only valid if the discharge frequency is very high. In an intermediate regime of discharge frequency, the electron velocity is then frequency dependent. It can be described by Margenau velocity distribution:

$$f_{e,Mar}(v) = A_1 \exp\left(-A_2 \frac{m_e^2 v^4 + 2m_e^2 \omega_{rf}^2 l_e^2 v^2}{4T_e^2}\right), \quad (2.1)$$

where v is electron velocity, m_e is electron mass, T_e is electron temperature, ω_{rf} is angular discharge frequency, l_e is the electron mean free path treated as constant, and A_1 and A_2 are coefficients, which can be determined from $\int_0^\infty v^2 f_{e,Mar}(v) d^3v = 3v_{T_e}^2$ and $\int_0^\infty f_{e,Mar}(v) d^3v = 1$, where $v_{T_e} = \sqrt{T_e/m_e}$ is the electron thermal velocity. If we limit ourself to the case where the discharge frequency is higher than the characteristic frequency of ions, we can estimate the particle charge by replacing the Maxwellian distribution of electrons by Margenau distribution in OML theory.

2.3 Results

The particle charge at the deep region in the sheath is weakly dependent on the pressure. Comparing to the theoretical estimation on single particle charge in the sheath in the PIC, the value of charge is much less. The theoretical value of the charge was estimated by using a simple expression for the ion current, corresponding to a displaced Maxwellian velocity distribution. However, the ion distribution in the sheath is rather complicated. Accurate calculation of ion current using method in Ref. [100] indicates that it could be up to one order of magnitude larger than the current we use in this work. Thus, the theoretical particle charges should be substantially smaller and, hence, closer to the values deduced from the fitting procedure of MD simulations.

As to the charge in the bulk plasma with various rf frequencies, assuming the same plasma parameters, we find that the dependence on particle charge on discharge frequency is different at different gas pressures. At low pressure, charge on the dust increases as the frequency increases. The increase can reach 10% if the pressure is sufficiently low. On the other side, if the pressure is relatively high, charge decreases as pressure increases. However, this decrease is so small that it can be neglected in most practical applications.

2.4 Outlook

Particle charging at different discharge frequencies is a very interesting topic [8]. In fact, the charge on particles with plasma at various rf discharge frequencies can be directly measured using different methods such as linear dust oscillation [81, 121]. One possible method is based on the levitation position of the particles in front of a surface [10], as we see in Fig. 2.3. With different discharge frequencies, microparticles are levitated at different height in the (pre)sheath region above the bottom electrode. The higher is the discharge frequency, the lower are microparticles levitated. The interparticle distance also changes with discharge frequency. When discharge frequency is 13.56 MHz, the interparticle distance is about 370 μm . As it increases to 90 MHz and 180 MHz, the distance decreases to 320 μm and 240 μm , respectively. We can also apply a certain biased voltage on the bottom electrode to manipulate the particle position. This requires further careful experiments. Our work here only proposes a theoretical charging model, which is discharge frequency dependent.

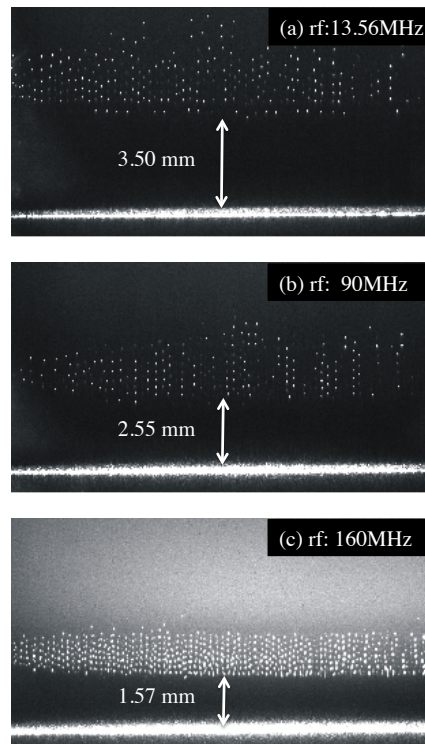


Figure 2.3: Microparticles in the discharge at different rf frequencies. The experiments were performed in the chamber shown in Fig. 2.1. The bottom electrode is replaced by a normal aluminum electrode, which is grounded. The input power is 0.3 W and the gas pressure is 30 Pa. The levitation height of particle cloud is 3.5 mm, 2.55 mm and 1.57 mm for the discharge frequency of 13.56 MHz, 90 MHz and 160 MHz, respectively. In the figure, it is clear that the glow is much stronger in a plasma with a higher discharge frequency. The difference of particle charge and thereby the levitation height are mainly caused by the change of plasma parameters resulting from the change of discharge frequency.

Chapter 3

Agglomeration of microparticles

This chapter provides complementary information to the paper:

- C.-R. Du, H. M. Thomas, A.V. Ivlev, U. Konopka, and G.E. Morfill, *Agglomeration of microparticles in complex plasmas*, Phys. Plasmas 17, 113710 (2010) No. 3

3.1 Objectives

As we discussed in the previous chapters, microparticles are strongly negatively charged in the plasma environment. In many experiments, particularly where the dust density waves are involved, we observed the emergence of particles of different species after the waves were suppressed. These particles were levitated beneath the major particle cloud with a clear interface. Due to a lack of other particle sources and based on their levitation height, we can conclude that these particles must be made of the same material and be large in size. One of the most probable explanations is agglomeration. However, theoretically the Yukawa repulsive interaction prohibits the agglomeration of particles due to their high charge. Only with very high kinetic energy, the repulsive potential can be overcome and two single particles can hit and stick together, forming an aggregate [32]. In the above mentioned circumstances, the dust density wave could be the driving mechanism to accelerate the particles to such high kinetic energy. In order to investigate the feasibility of agglomeration of microparticles in a plasma, we perform a series of experiments in the PK-3 Plus chamber on the ground using particles of various sizes and materials.

3.2 Methods

We performed the experiments in the modified PK-3 Plus chamber on the ground, see Fig. 3.1. The chamber consists of two parallel electrodes driven in push-pull mode at a frequency of 13.56 MHz. The particles can be inserted by shaking the dispensers mounted on the top electrode. A vertical laser sheet with a thickness of about of 100 μm was used

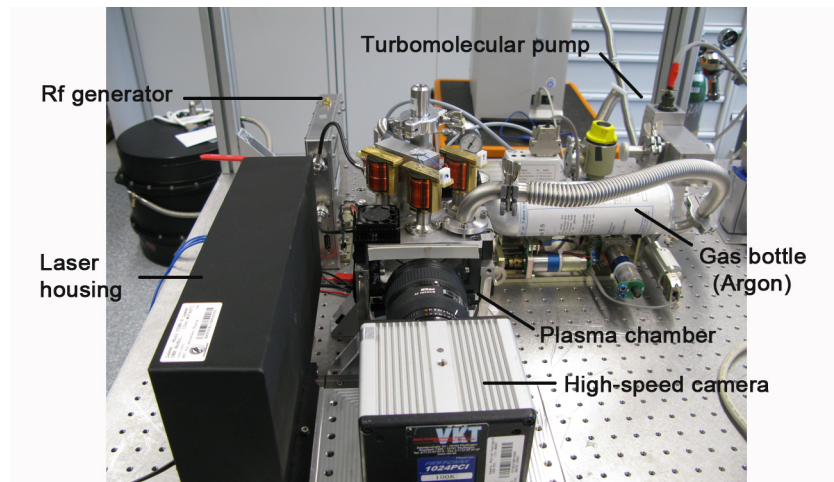


Figure 3.1: Photo of PK-3 Plus chamber in the laboratory on the ground. The particles are inserted from the dispenser on the top electrode. A high-speed camera is installed to record individual particle motion in the waves. Reproduced from Ref. [32].

to illuminate the particles in the plasma. The individual particle motion can be recorded by a high-speed video camera for further analysis.

In order to accelerate the particles in the plasma, self-excited waves [82, 97, 111] were triggered by reducing the gas pressure. Particle velocity distribution is calculated in the waves and the collision probability is compared with the final number of aggregates we observe. Furthermore, we installed a long-distance microscope with back light to observe the shape and structure of aggregates *in-situ* in the plasma. This observation is only feasible as gas pressure is restored and particles are relaxed.

3.3 Results

By performing a series of experiments, we prove that agglomeration is feasible for microparticles immersed in the plasma despite of their high surface charge. However, a driving mechanism, for instance self-excited waves in our experiments, is needed to accelerate particles to overcome the interparticle repulsion. The particle charge can be deduced based on the elastic collision events in the waves captured by the high-speed camera. In fact, both particle charge and Debye length are deduced by fitting a two-body elastic collision simulation to the experimental observations. It turns out that Debye length is insensible to the fit and thus the Rutherford's scattering theory is applicable in our case, as we explained in the paper. With the information of particle charge and velocity, which is measured directly in the video, we can deduce the agglomeration rate and compare it with the experimental observations. The result confirms that the source of those large particles is agglomeration of microparticles in the initial dust cloud. The estimation was performed for the MF microparticles with a initial size of $2.5 \mu\text{m}$ in diameter. However,

by performing the similar experiments with particles of other sizes and materials, we show that particle agglomeration in plasma is generally feasible for different kinds of particles.

Conventional laser illumination with video camera recording is a powerful system to obtain the information of microparticles such as their positions, velocities. However, if we are interested in the shape or structure of individual grains, a long-distance microscope can provide more information. Compared to the normal optical microscope or scanning electron microscope (SEM), the greatest advantage of a long-distance microscope is that it can capture the particle shape and structure while they are still levitated in the plasma in the chamber. In this case, we don't have to collect the samples from the chamber and therefore eliminate the risk of external contaminations¹. By analyzing the photos captured by long-distance microscope, we find that most aggregates are made of two single particles, while a few aggregates consist of more than two single particles. The aggregates composed of several particles can have different structures [80], which is apparently related to the way how the aggregates are formed. Interestingly, if the aggregates have a elongated shape, the long axis is perpendicular to the bottom electrode, see Fig. 3.2. This might be explained by the ion wake effect since those aggregates are usually levitated in the sheath area.

3.4 Outlook

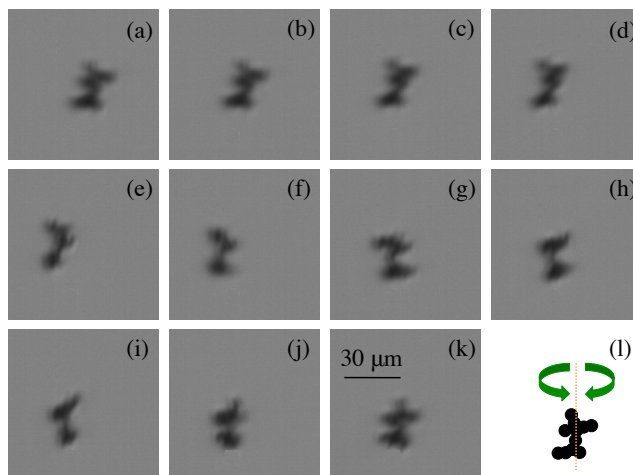


Figure 3.2: Spin of an aggregate suspended in the plasma. A consecutive of images shows the motion of the elongated aggregate. Based on the asymmetry of the aggregate (the “branches” on the side of the aggregate), one can notice that it moves against the major axis. However, it is hard to tell whether the aggregate is spinning or swinging.

¹ In the Ref. [32] we present a SEM photo of microparticles collected from the chamber after wave excitation. Although we see several “aggregates” composed of several single microparticles, the results are not conclusive since we cannot rule out the possibility that those “aggregates” are formed during the collection.

It is interesting to observe the behavior of individual aggregates in the long-distance microscope. Sometimes, such aggregates seem to spin around their long axis, as shown in Fig. 3.2. However, from the side view alone, one can not conclude the spin direction. It is even possible that the aggregate is not spinning but swinging. This requires further careful analysis.

Chapter 4

Interaction of 2D crystalline lattices with upstream particles

This chapter provides complementary information to the paper:

- C.-R. Du, V. Nosenko, S. Zhdanov, H.M. Thomas, and G.E. Morfill, *Interaction of two-dimensional plasma crystals with upstream charged particles*, Europhys. Lett. 99, 55001 (2012) No. 4

4.1 Objectives

As a disturbance moves in a medium, it produces waves and wakes behind it. The medium can be gas, liquid as well as solid. As we all know, a ship moving in a deep water leaves multiple lateral wakes and transverse wakes behind it [86]. Sometimes if the disturbance is in the supersonic regime, i.e., faster than the sound speed of the medium, the wakes show a V-shape structure. This structure is called Mach cone, see Fig. 4.1. For example, an aircraft can create a vapor cone at transonic speed in the air [18]. This phenomenon can also happen to a solid medium even to a crystal. However, as we know, it is not easy to directly observe such phenomenon in a solid medium. Thanks to the discovery of plasma crystal, we can observe the Mach cone structure in a 2D crystalline, which is excited by a supersonic disturbance, of the “atomic” level [105, 106]. In other words, the reaction of individual particles to the disturbance in the waves can be recorded and analyzed directly. Recently, in complex plasmas, mach cones in 3D complex plasma are also observed [59, 110]. The disturbance in the above described cases is always a moving projectile [105]. However, it can also be from some other sources such as a laser [91].

In laboratory experiment, we observed a kind of Mach cone in a 2D plasma crystal, which has a strikingly different feature from the ones reported earlier [105]. This triggers a detailed study on the structure as well as the source of such Mach cone. We call the newly found Mach cone type I and the reference Mach cone type II for the purpose of distinction, as in paper No. 4.

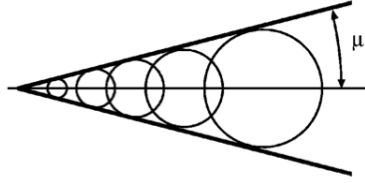


Figure 4.1: Sketch of a Mach cone produced by a supersonic disturbance moving to the left. The cone angle μ is defined as $M \sin \mu = 1$, where M is the Mach number. Reproduced from Ref. [106].

4.2 Methods

The experiment was performed in a GEC reference chamber, as we show in Fig.4.2. The bottom electrode is connected to a matching box, driven by a rf generator with a constant discharge frequency of 13.56 MHz. Comparing to the chambers mentioned earlier in this thesis, it has a larger size (220 mm diameter) in order to form a large flat 2D plasma crystal. The counter electrode is a grounded ring, which is mounted inside the chamber. A high-speed camera and an overview camera are installed above the chamber to record the particle motion in the lattice layer. A side view camera is installed and used to purify the 2D plasma crystal¹. Apart from a regular laser (not shown in the photo) which is used to illuminate the lattice layer, a second laser is installed to observe the source of disturbance.

As we report in the paper, the disturbance source of type I Mach cone is upstream particle², while that of type II Mach cone is downstream particle. In order to study the structure of Mach cones and lateral wakes, we follow the earlier references [91, 106] to analyze the speed map, divergence map and vorticity map, as shown in Fig. 4.3. Generally speaking, the speed of disturbance in type I Mach cone is slower than type II Mach cone. In order to make the experiments for two types of Mach cone comparable, we adjust the Mach number³ similar in the two examples presented here, i.e., $M \simeq 1.2$ for type I and $M \simeq 1.3$ for type II.

The Mach cone excited by extra particles, as shown in the velocity map in Fig. 4.3(a,b), contains both compressional and shear wakes. Several lateral wakes are visible in both cases. The magnitude for the velocity is much smaller in the Mach cone excited from above, representing a weaker disturbance. The cone angle presented in the paper, see the definition in Fig. 4.1, is measured in these speed maps. The cone angle is measured to be $55^\circ \pm 10^\circ$ and $50^\circ \pm 6^\circ$ for type I and II Mach cone, respectively. This agrees with the measurement of Mach number.

Comparing the $\nabla \cdot \mathbf{v}$ map of Fig .4.3(c) and (d), which show the compressional wake, we can resolve not only the first cone but also several lateral wakes in both cases. As we

¹ During the purification procedure, we increase the gas pressure and decrease the discharge power to drop the particles of larger size on the bottom electrode.

² Upstream of the ion flow in the (pre)sheath in respect to the lattice layer.

³ The Mach number is defined as $M = v_d/C_L$, where v_d is the speed of extra particle and C_L is the longitudinal sound speed of the crystalline lattice [94, 95].

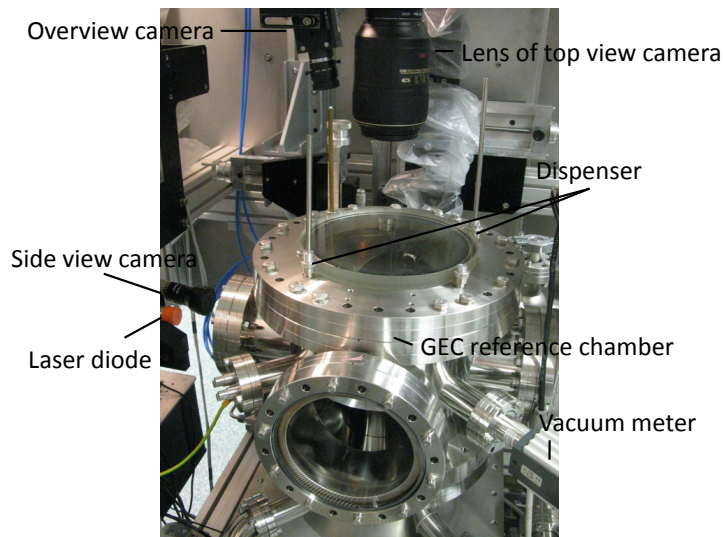


Figure 4.2: Photo of GEC reference chamber. The bottom electrode is driven and the counter ring electrode is grounded (also see the sketch in Fig. 1 in the included paper No. 4). There are three video cameras installed to record the top view and side view of lattice layer. The chamber is particularly suitable for 2D plasma crystal experiments [92, 26, 27].

look closer at the apex of the cone in the divergence map, the sign of the divergence at the wave front is opposite in two cases. It is positive for type I Mach cone and negative for type II. Particles in the monolayer in type I cone are moving towards the disturbance, while in the other case they move away. This implies already an attraction for type I Mach cone⁴, other than the repulsion for type II. As to the vorticity $\nabla \times \mathbf{v}$ map of Fig. 4.3(e) and (f), the cone angle in the shear wave is much smaller than that in the compressional wave since the transverse wave speed is much lower, revealed by phonon spectrum analysis. The angle matches the prediction relatively good to be $\mu \approx 8^\circ$.

4.3 Results

Although both types of Mach cones are excited by extra particles, the interaction mechanism is quite different. For type I Mach cone, the extra particles located above the lattice layer. This will induce a ion wake effect beneath the extra particle. Sometimes we can use a model of an imaginary positively charged particle to simplify the ion wake effect. Thus an attractive force is generated to drive particles in the lattice layer toward the extra particle, complying with our observation. The situation is different for type II Mach cone. There the dominant interaction is still Yukawa repulsive. This causes the different features of the two Mach cones.

⁴ See the net force map in the paper attached for detail.

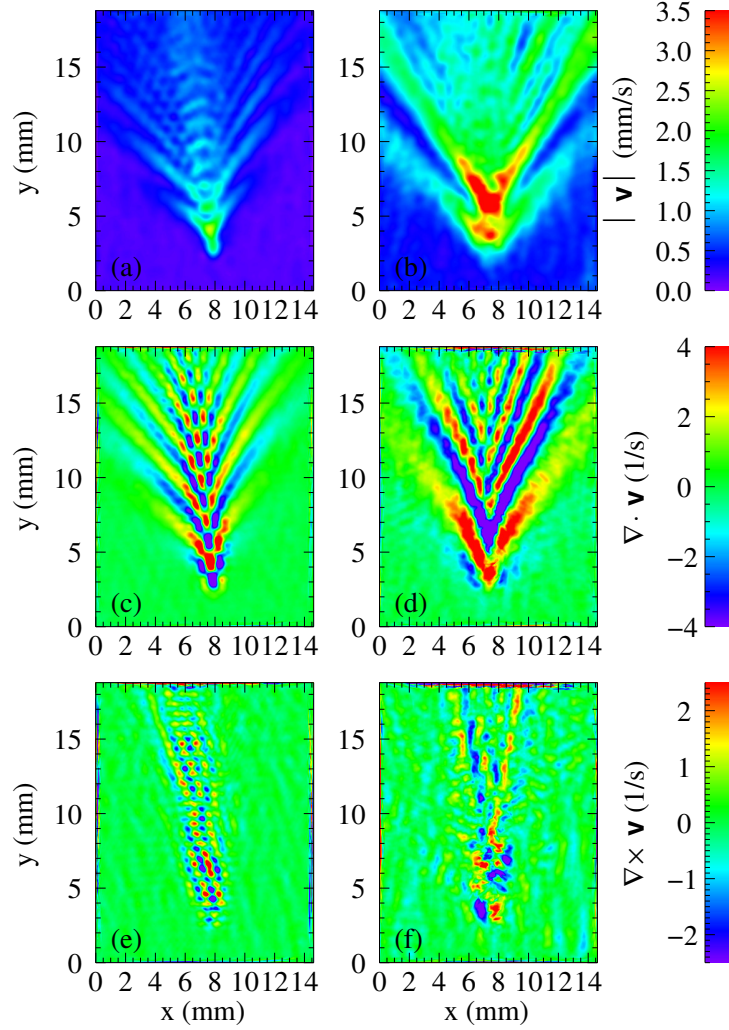


Figure 4.3: Comparison of the wave features between type I and type II Mach cones: (a,b) The speed $|\mathbf{v}|$ map of type I (left) and type II (right) Mach cone. The disturbance from the upstream particle is much weaker than from the downstream particle; (c,d) The divergence $\nabla \cdot \mathbf{v}$ map of type I (left) and type II (right) Mach cone. At the apex of the divergence map, the sign of divergence is opposite in two cases; (e,f) The vorticity $\nabla \times \mathbf{v}$ map of type I (left) and type II (right) Mach cone. The small wave length of the shear wave and discrete particle positions in the lattice lead to a feature of isolated bright spots in the map.

As we study the effect closer, we notice that upstream particle moves preferable in the channel in the lattice. We call it “channeling” effect. Two rows of particles in the lattice form a channel, confining the upstream particles. Meanwhile the upstream particle deform the channel via ion wake effect.

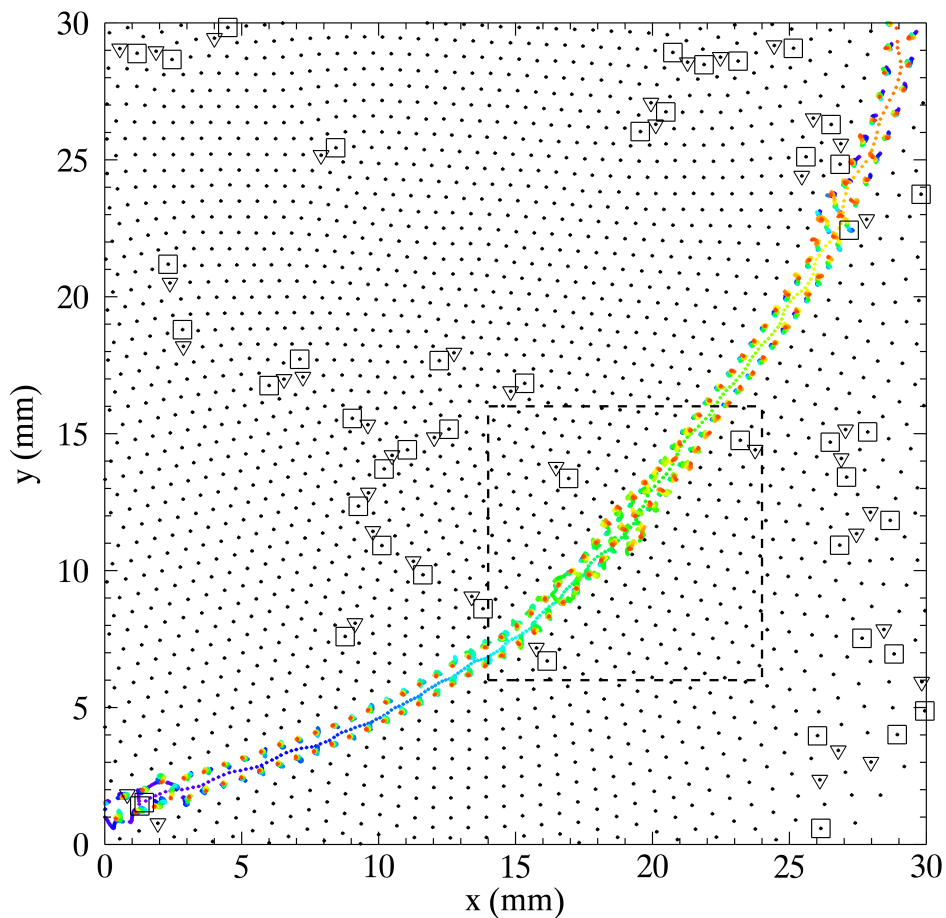


Figure 4.4: Illustration of channeling effect in a bent 2D crystal lattice. Black dots represent the lattice particles, colored dots represent position of the upstream particle and the “wall” particles (coded from blue to red). The region where the channel strongly bends is marked by a dashed-line rectangle. The 7-fold cells are marked by the triangles, and 5-fold cells are marked by the squares.

4.4 Outlook

If defects exist in the lattice layer, the channeling motion of extra particle is disturbed. The extra particle changes path depending on the local structure as well as the particle motion itself. Two examples are demonstrated in the paper. This requires a further careful analysis.

In addition, we observe *in situ* the channeling effect of an upstream particle in a bent 2D plasma crystal at kinetic level, as shown in Fig. 4.4. As we discussed in the introduction, bent crystal is widely used as a collimator in the accelerator to direct ions or protons [30, 37]. Despite the difference of the kinetic energy of the projectile, studying channeling effect in a bent 2D plasma crystal can still provide rich information of the interaction

between the channeling particle and the medium.

Chapter 5

Lane formation in binary complex plasmas

This chapter provides complementary information to the papers:

- K. Jiang, C.-R. Du, K.R. Sütterlin, A.V. Alexei and G.E. Morfill, *Lane formation in binary complex plasmas: Role of non-additive interactions and initial configurations*, Europhys. Lett. 92, 65002 (2010) No. 5
- C.-R. Du, K.R. Sütterlin, K. Jiang, C. R ath, A.V. Ivlev, S. Khrapak, M. Schwabe, H.M. Thomas, V.E. Fortov, A.M. Lipaev, V.I. Molotkov, O.F. Petrov, Y. Malentschenko, F. Yurtschichin, Y. Lonchakov, and G.E. Morfill, *Experimental investigation on lane formation in complex plasmas under microgravity conditions*, New J. Phys. 14, 073058 (2012) No. 6
- C.-R. Du, K.R. S utterlin, A.V. Alexei, H.M. Thomas and G.E. Morfill, *Model experiment for studying lane formation in binary complex plasmas*, Europhys. Lett. 99, 45001 (2012) No. 7

5.1 Objectives

As the ubiquitous prototype of non-equilibrium pattern formation, lane formation has drawn a lot of attention over the last decade. In the daily life, one can often observe the formation of lanes when two crowds of people move towards each other, as shown in a demonstration experiment in Fig. 5.1 [69]. Such phenomenon also appears quite often in the discipline of physics. It has been widely studied in colloidal suspensions both experimentally and numerically [33, 76]. Recently lane formation has also been observed in binary complex plasma on board the International Space Station [117, 116]. Both complex plasma and colloidal suspension are soft matter and share a lot of properties [99, 127]. However, compared to colloidal suspension, the damping rate in a complex plasma can be much lower, virtually undamped under certain experimental conditions [84]. This gives us an unique opportunity to study the dynamics of lane formation.



Figure 5.1: Demonstration of lane formation as two crowds of people walk towards each other. This experiment shows how walkers self-organize into lanes to avoid interactions with oncoming pedestrians. It is a snapshot adopted from the supplementary video of a magazine article [107].

This chapter includes three separate works which are closely related to each other. We first study the influence of non-additivity on the lane formation using a Langevin dynamics (LD) simulation [55]. Using the data from a series of experiments in PK-3 Plus laboratory on board the ISS, we investigate various factors which also affects the process of lane formation, including the size ratio and density ratio. However, the experimental condition is not ideal on board the ISS due to the limitation of the chamber itself and supporting hardware such as camera. This brings some difficulties to compare the experiment directly with simulation. Therefore, we perform an experiment on the ground using vortex as a driving mechanism of penetrating particles to form lanes in the background of particles of a different species.

5.2 Methods

On one hand, in order to investigate the influence of non-additivity on the lane formation process, we apply LD simulation of a binary complex plasma system. On the other hand, a series of experiments were performed on board the ISS to study different aspects of lane formation, when bunches of small particles were injected into the cloud of big particles. As a supplementary experiment, lane formation was also realized on the ground in the same chamber with additional heaters installed to generate thermophoresis. Instead of bunches of particles, penetrating particles were driven continuously so that a steady state of lane formation was achieved.

5.2.1 Langevin dynamics simulations

Langevin dynamics simulation is a popular method to simulate a multi-particle system of single species or multiple species. The governing Langevin equation is a stochastic differential equation in which two force terms¹ have been added to Newton's second law [56, 41]:

$$\mathbf{F}_i - \gamma_i \mathbf{v}_i + \mathbf{R}_i = m_i \dot{\mathbf{v}}_i, \quad (5.1)$$

where m_i , \mathbf{v}_i , and γ_i are mass, velocity and damping rate of particle i . The force exerted on the particle can be expressed as $\mathbf{F}_i = \sum_{j \neq i} \nabla \phi_{ij} + \mathbf{F}_{ext}$, where the first term on the right is the force resulted from interparticle interaction and the second term is the external force. In the simulation, the damping rate can be calculated based on the Epstein neutral drag: $\gamma_i = \delta_{Ep} \frac{8}{3} \sqrt{2\pi} r_p^2 m_n n_n V_{T_n}$ which depends on the particle size. As to the stochastic force term \mathbf{R}_i , it represents the random kicks from surrounding media molecules and is commonly described by a delta-correlated stationary Gaussian process [75]:

$$\langle \mathbf{R}_i(0) \mathbf{R}_i(t) \rangle = 2\gamma_i k_B T_p m_i \delta(t), \quad (5.2)$$

where $\langle R_i(t) \rangle = 0$, T_p is the system temperature, δ is Dirac delta function.

The simulation is applied to a system composed of two species of particles. The non-additivity is implemented in the simulation realization, see Chapter 1. In order to simulate the lane formation situation in the space station, a bunch of small particles was driven by an external force, which is derived from the experimental observation. The small particles penetrate into the cloud of big particles, forming lane structure. More details can be found in the attached paper No. 5.

5.2.2 Experiment on board the ISS

The first experimental realization of lane formation in complex plasma was performed under microgravity condition on board the ISS. Under microgravity condition, big particles can fill a large fraction of the chamber, forming a dust cloud of large size and served as the background medium for lane formation. Also due to the absence of gravity, small particles can be driven by the plasma potential and tend to move to the center of the chamber. All these make the experiment of lane formation possible².

The setup of the experiment is introduced in great detail in the attached paper No. 6 as well as in Ref. [120]. Here we only show a photo of the overview of the setup taken in the preparing stage before it is launched to the space station, see Fig. 5.2. The setup is sealed in a cylindrical container and operated by a control system named "Telescience".

¹ Friction term $-\gamma_i \mathbf{v}_i$ and stochastic force term \mathbf{R}_i .

² On the ground, big particles can only be levitated in several layers above the bottom electrode. As small particles are injected inside the chamber, they simply move to the position above the pre-injected big particle cloud without penetration due to their smaller mass-charge ratio.

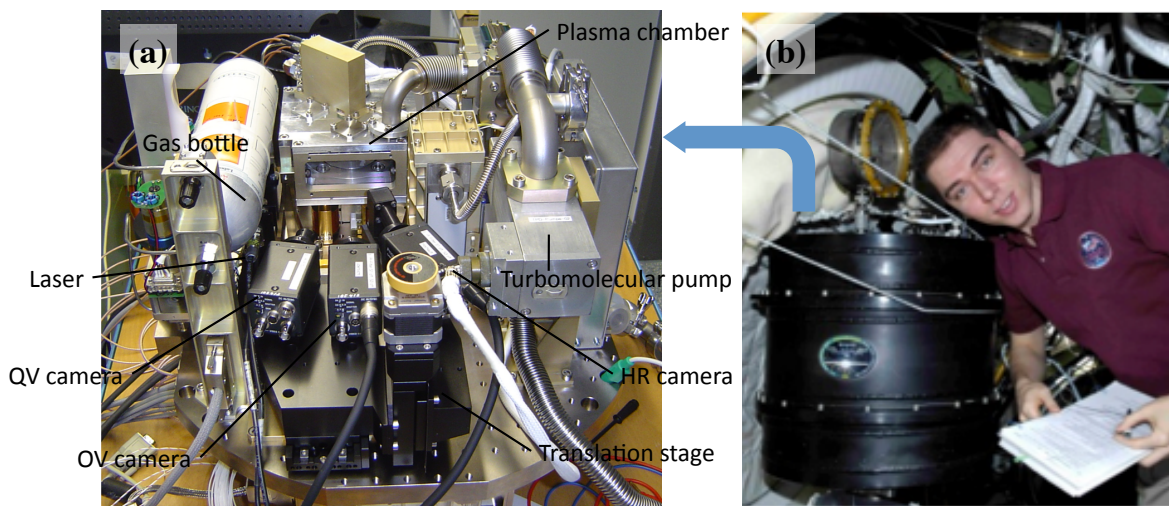


Figure 5.2: Photo of PK-3 Plus laboratory on board the ISS: (a) The interior structure of PK-3 Plus laboratory. Three cameras were installed to have overview, quadrant view, and high resolution view of individual microparticles in the plasma (also see the sketch in paper No. 6). Argon gas and neon gas are available for discharge; (b) The outlook of the laboratory and the operating cosmonaut. The devices are enclosed in the black cylindrical container.

In order to quantify the lane formation, we employed an anisotropic scaling index method (ASIM) to realize a local nonlinear measure for structure characterization³. The method is developed based on the weighted scaling index method [98]. For the detail of the analysis method, please read the attached paper No. 6.

We use this method not only to quantify the lane structure in the LD simulation, but also to compare the lane structure in various experiments performed on the ISS with different experimental conditions. In both cases, we apply this method to investigate the lane structure formed by the big particles in the background only. Besides, we also measure the kinetic energy of the penetrating the particles as a parameter. With this measurement, we can investigate the “memory” effect of the first injection on the consecutive injection.

Apart from kinetic measurement, we also analyze the lane structure based on the direct observation in a different angle of view, which we name as “view-in-line”. From this angle of view, a unique structure, i.e., “honey comb” structure during the penetration is revealed. This implies a cage effect during the lane formation.

³ The analysis is rather time consuming since it involves all pair correlation. In order to study the influence of initial condition on lane formation, we repeat the LD simulation as well as the analysis for each parameter 1000 times with random initial conditions. The code first ran on XGRID cluster in the theory of MPE to analyze the simulation results. Later on, an analysis code is developed to analyze the experimental results from the ISS based on GPU parallel computation [88].

5.2.3 Experiment on the ground

As to the ground experiment, we successfully performed the lane formation experiment in the modified PK-3 Plus chamber. The device has been introduced in Chapter 3, see Fig. 3.1. In addition, we installed the heater on the bottom electrode and fans on the top electrode. By heating the bottom electrode and cooling the top electrode, a temperature gradient can be produced. With selection of a certain temperature gradient, thermophoretic force can be generated to compensate gravity of microparticles, as explained in the introduction in Chapter 1. The combination of two particle types was specially selected so that the gravity can be compensated by the same temperature gradient. Due to the inhomogeneous heating on the wall of the chamber, particle circulation (vortex) was created on the side of dust cloud close to the wall [48, 104]. We took advantage of this phenomenon as driving mechanism to indirectly “pump” the big particles into the dust cloud of small particles to realize lane formation.

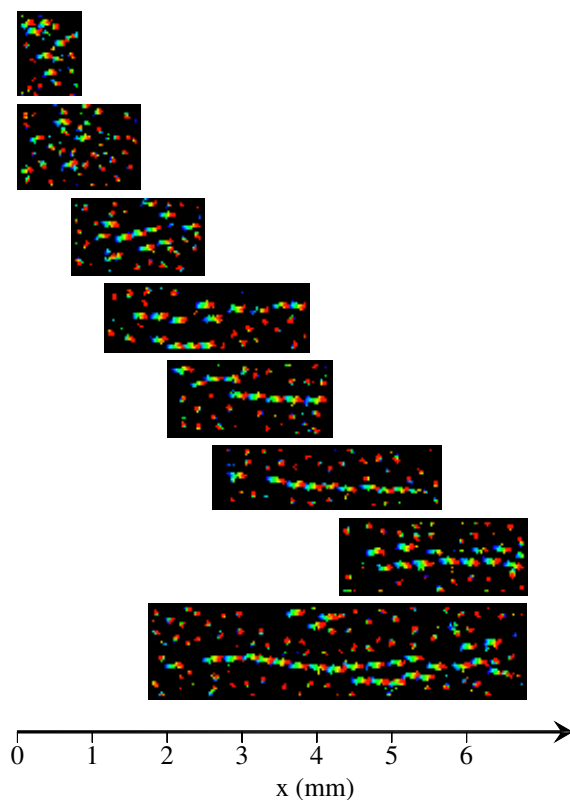


Figure 5.3: Samples of lane structure along the penetration direction. The eight panels show overlays of colored raw images in 6 consecutive frames (coded from blue to red). As the big particles sink to a deeper position, lane structure is gradually formed. This figure corresponds to Fig. 2 in the attached paper No. 7.

In this experiment, we concentrate more on the penetrating particles instead of back-

ground particles. Samples of lanes formed by penetrating particles are shown in Fig. 5.3. As the big particles move deeper into the dust cloud, the lane structure is gradually formed. In order to quantify the development of the lane formation of penetrating particles, we applied the order parameter Φ , which has been recently used to identify the lane structure in colloidal suspensions [127]. For the details please read the attached paper No. 7.

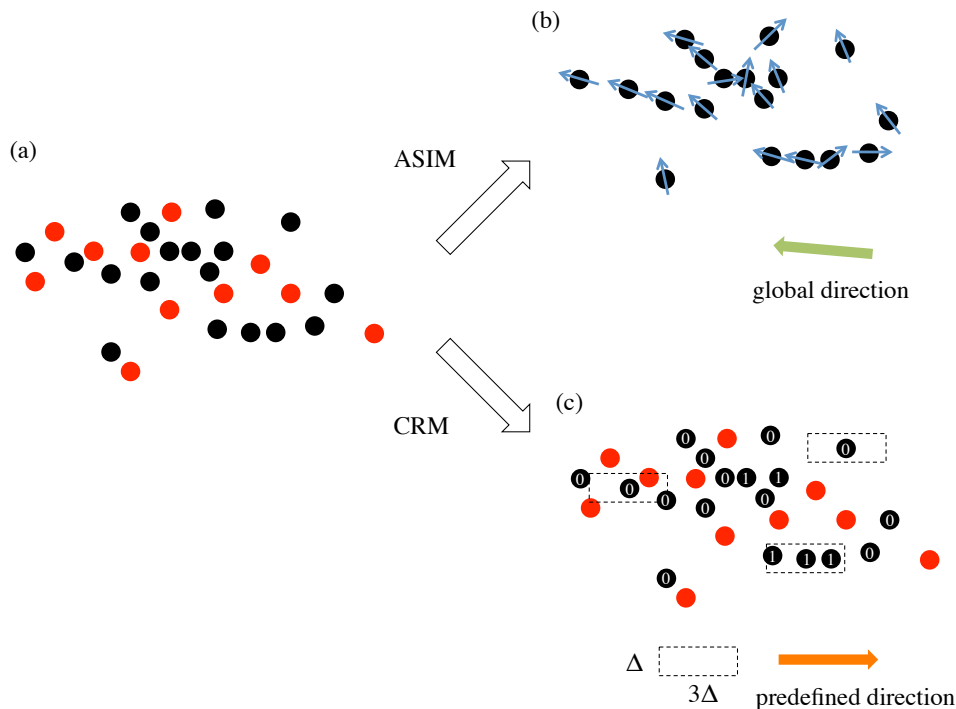


Figure 5.4: Illustration of anisotropic scaling index method (ASIM) and centered rectangle method (CRM) for quantification of lane structure: (a) A sample of binary mixture. Black dots and red dots represent particles of two species. In this illustration, the black dots are the particles we are interested in. (b) Illustration of ASIM. Only the particles of interest are included for analysis. Preferred angle (ranging from 0° to 180°) is calculated for individual particles taking into account all particles of the same species. A global direction (denoted by green arrow) results from the “average” of the preferred angle of all particles. (c) Illustration of CRM. Particles of both species are taken into account. A “True(1)-False(0)” value is assigned to each particle considering only the particles in the neighborhood (shown by dashed rectangle aligned at the predefined direction, marked by orange arrow, based on the specific experiment configuration). This value (either 1 or 0) shows whether the target particle is in the lane or not, respectively.

Let us compare the analysis method used here with the one used to analyze the space data. For the convenience of comparison, we name the analysis method for the ground experiment as centered rectangle method (CRM) since the method is based on the particles

within a fixed-size rectangle centered at the target particle. The only common part of these two methods is that every particle of interest is assigned a value in the analysis. However, the value has different origins and also different meanings. In ASIM, a “preferred” angle ranging from 0° to 180° is calculated for individual particles. This angle is calculated based on positions of all the particles of the same species in the snapshot. This means that both long-range effect and short-range effect are included⁴. In CRM, the value has only two possibilities: 1 means that the particle is in a lane or 0 means that the particle is not in a lane. To calculate this value, a rectangle with a length of 3Δ and a width of Δ is centered to a target particle, where Δ is average interparticle distance. Only the particles within this rectangle are taken into account. In other words, only the neighboring particles contribute to this “True-False” value and the long-range term is completely suppressed. In the final result, the order parameter represents a collective effect of particles either in a single snapshot (ASIM) or in an area of the same height (CRM)⁵. In ASIM the lane order parameter results from the eigenvalue of the sum of a second-rank tensor of “preferred” direction for each particle. It represents the deviation of the preferred angle of all big particles in the region of interest from the penetration direction in one time moment. In contrast, in CRM the lane order parameter results from the average of the “True-False” value of all small particles at the similar height, representing the percentage of particles in the lane. Based on the above stated features, in conclusion, the ASIM fits more to the case where there is a large amount of particles in the space to achieve good statistics. On the contrary, CRM is more suitable to investigate the local structure and can to some extent overcome the disadvantage of poor statistics⁶. This is exactly the case we have for these two distinct experiments.

5.3 Results

The LD simulation is employed to study the lane formation with non-additive particle interaction in binary complex plasma. The results show that the lane order parameter decreases with increase of non-additivity parameter. A crossover from the normal laning mode to a demixing-dominated laning mode is revealed. The simulation also shows that the initial configuration plays an important role in lane formation. Even though the initial configurations are thermodynamically equivalent, the minuscule details of single-particle kinetics defines the dynamics of laning.

The study of experiments performed on board the ISS provides a comprehensive view on different aspects on lane formation. It is found that if the number of injected small particles is increased, big particles are more easily caged between the lanes formed by

⁴ Even though a weighting factor is included so that long-range effect has less contribution than the short-range effect, both of them have influence on the ultimate preferred angle.

⁵ This has nothing to do with the property of method itself but with the different study objects of two experiments. In the space experiment we focus on the time evolution while in the ground experiment we are more interested in the height dependence.

⁶ In order to investigate the development of lane structure against height, the cloud is segmented into slices where a limited amount of particles exist in each slice.

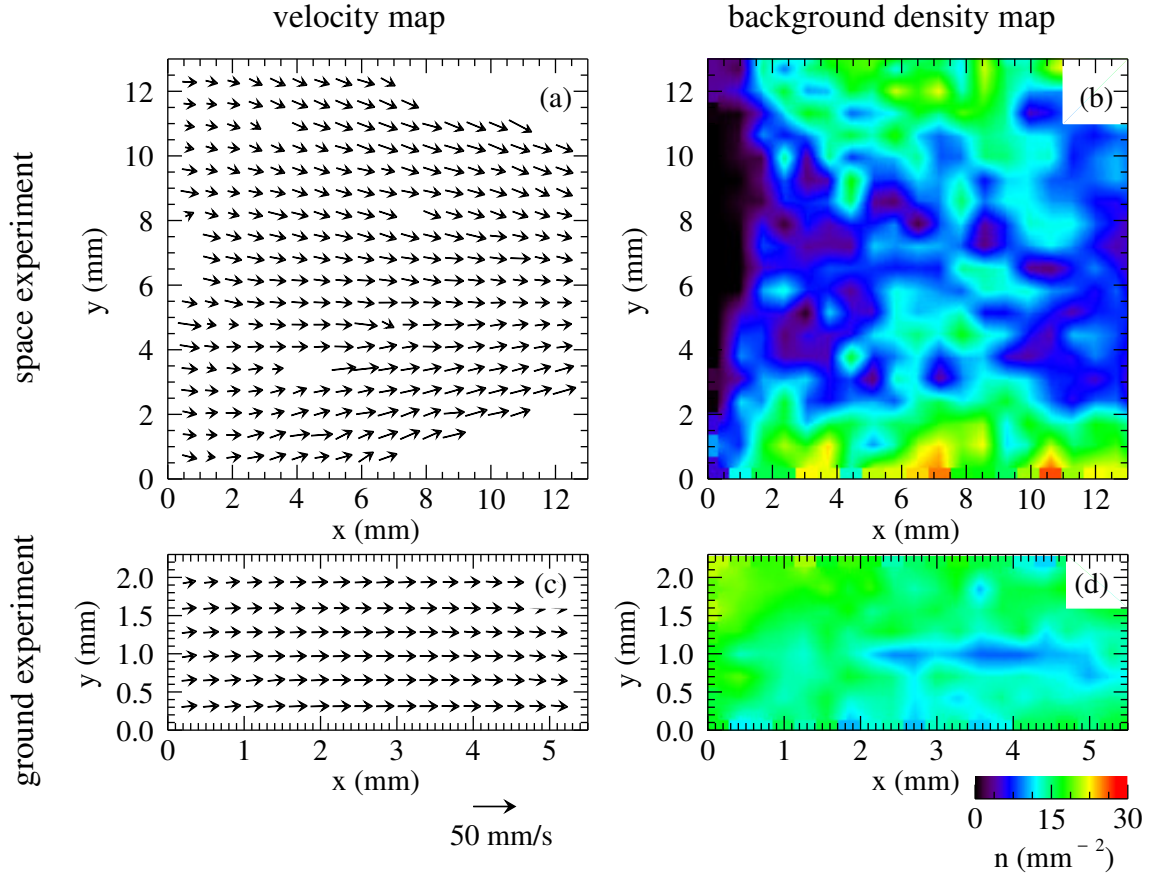


Figure 5.5: Comparison between the space experiments and the ground experiments: (a,c) Velocity map for space and ground experiments. Comparing to the experiments performed on board ISS, velocity of penetrating particles is more uniform in both direction and magnitude in the experiments on the ground; (b,d) Particle number density map in the background for space and ground experiments. Likewise, the particle number density is more homogeneous in the ground experiments.

small particles, resulting in a higher peak of lane order parameter. By tuning the time interval between two consecutive penetration events of small particles, we investigated the “memory” effect of the previous penetration on the consecutive one. From the point view of kinetics, the shorter the time interval, the faster the small particles penetrate through the background particle cloud in the second penetration. Based on the peak value of order parameter, we find the memory effect is linear. In addition, we observe a crossover from free lane formation to a demixing dominated mode of the nonequilibrium system in the same set of experiments.

The experiments on the ISS have also some drawbacks. As we see in Fig. 5.5, for the penetrating particles the direction and the magnitude of the penetrating particles varies

depending on the location in the chamber. Clearly, the particles on the wings move in direction to the very center of the chamber, resulting in non-parallel velocities. As to the particle number density in the background, the density is much higher on the wings than in the middle of the dust cloud. The density is far from homogeneous even in the middle. All these facts bring a lot of difficulties in the numerical simulation and theory building. Moreover, the cameras on board the ISS have relatively low recording rate and spatial resolution due to the weight and size limitation of the payload. As result we can not clearly observe the lane formation of the penetrating particles. On the ground we can use a high-speed camera instead to overcome that drawback and investigate the lane formation of penetrating particles.

The experiments performed on the ground can overcome those drawbacks. As we see in Fig. 5.5 in the thesis and Fig. 3 in paper No. 7, penetrating particles move quite uniformly to the right. The particle number density is rather homogeneous comparing to the experiments performed on board the ISS. This provides a very convenient model system for comparison with computer simulation and experiments in colloidal suspensions.

In addition, instead of injecting bunches of particles [117], we can continuously “pump” particles of one type into the particle cloud of the other type. This is essential for studying the process of lane formation from the point that particles start to penetrate into a cloud until they move deeper in the cloud and form stable lanes. As we see in paper No. 7, initially the lane order parameter increases linearly as the big particles move deeper in the background of small particles. In the later stage, the lanes stop to grow and the lane order parameter reaches a plateau.

5.4 Outlook

Lane formation in complex plasma has been studied thoroughly under different experimental conditions in PK-3 Plus chamber both in the ISS and on the ground⁷. We also present a model experiment, which is convenient to directly compare with numerical simulations. In the future, we should work on the mechanism of lane formation to address the questions such as how the lanes grow. Do the lanes grow by adding single particles to the existing lanes or by merging short lanes together to form longer lanes? How do the single particles form short lanes initially? Are there any attraction mechanisms involved? To answer those questions, we need more theories and numerical simulations to compare with the observations we have made in the experiments.

⁷ The plasma in PK-3 Plus chamber is generated by rf discharge. Recently lane formation has also been observed in PK-4 laboratory in the parabolic flight. In principle PK-4 chamber is composed of a glass tube where two electrodes are mounted at the two ends of chamber. Plasma is generated by DC discharge. The elongated configuration of the chamber provides many advantages for studying lane formation. For more details of the chamber, please read Ref.[39].

Chapter 6

Summary

To summarize, we start this cumulative thesis by reviewing some basic theoretical aspects of complex plasmas. As original works, we first investigate particle charge in deep sheath experimentally and build a theoretical model to calculate the particle charge in the bulk plasma ionized in a wide range of discharge frequencies. In the third chapter, we show experimentally that agglomeration is feasible in complex plasma despite the existence of strong interparticle repulsion due to high charge on the particle surface. Afterwards, we study the interaction of an extra particle (upstream of the ion flow) with a lattice layer in 2D plasma crystals. In the end, a series of experiments as well as a set of Langevin dynamics simulations dedicated to study lane formation are presented. The results are listed as follows:

- Using hybrid analysis method combining particle tracking, molecular simulation, and particle-in-cell simulation together, particle charge is measured in the experiment of Coulomb “explosion”. The particle cloud is initially confined by a rf segment of a “adaptive” electrode in the deep sheath. As the segment is switched off, the initial stage of the “explosion” is carefully investigated. For three different gas pressures, the charge of 4.8 μm particle is measured to be around one thousand elementary charges at the height of 0.15 mm from the bottom electrode.
- We develop a theoretical approach to calculate particle charge in a wide range of discharge frequency based on Margenau electron velocity distribution. The model is applicable for charging in a bulk plasma in the collisionless regime. The surface potential, which is proportional to the particle charge, increases with an increase of discharge frequency at low gas pressures, and decreases at high pressures. However, the observed variations are so small that in practical situations the direct effect of the rf frequency on the particle charge can be masked by indirect effects associated with plasma parameter modification in response to changing the discharge frequency.
- By triggering self-excited waves in a cloud of microparticles in the presheath region in a low pressure rf discharge, we are able to accelerate particles to velocities that are sufficiently high to overcome their mutual Coulomb repulsion. This results in

the particle agglomeration – the formation of clusters consisting of two, three or more particles. This effect is observed for particles of different sizes and materials. By using a long-distance microscope, we are able to observe the aggregates *in situ*, levitated in plasma after wave excitation.

- We observe an extra particle moving above a monolayer of crystalline lattice with a speed higher than the sound speed. The particle is in the upstream of the ion flow in respect to the lattice layer and generates lateral wakes and Mach cone. At the apex of the Mach cone, the interaction between the lattice layer and the upstream particle is attraction dominated. We show a “channeling” effect of the upstream particles as they tend to move between the rows of particles in the crystal.
- Langevin dynamics simulations are employed to investigate the lane formation phenomenon with additive and non-additive particle interaction in binary complex plasma. In order to quantify the lane formation in the simulation, we use an anisotropic scaling index method to realize a local nonlinear measure for structure characterization. The peak value of laning order parameter decreases with an increase of non-additivity parameter. A crossover from the normal laning mode to a demixing dominated laning mode is observed with a critical value of non-additivity parameter of 0.1. We find that the initial configuration plays an important role in lane formation.
- A series of experiments dedicated to probing the phenomenon of lane formation in binary complex plasmas over a broad range of parameters has been performed with the PK-3 Plus laboratory on board the International Space Station. We show that the dynamics of lane formation varies considerably with density of the background and the size ratio between small and big particles. By tuning the time interval between two consecutive penetration events of small particles, we investigate the “memory” effect of the previous penetration on the consecutive one. The shorter the time interval, the faster the small particles penetrate through the background particle cloud. The peak value of laning order parameter has no evident dependence on the time interval, and the memory effect is linear. In addition, a crossover from free lane formation to a demixing dominated mode of the nonequilibrium system has been observed.
- A model experiment for studying lane formation in binary complex plasmas has been conducted in the PK-3 Plus chamber on the ground. Gravity is compensated by thermophoretic force generated by a temperature gradient. The driving force of penetrating particles is independent of time and position and background density is homogeneous and isotropic. The evolution of lane formation along the penetration direction is investigated using lane order parameter. This provides an ideal model system for comparison with numerical experiments and observations in colloidal suspensions.

List of Figures

1.1	Two important discoveries for the complex plasma research	2
1.2	RF plasma and plasma diagnostics	4
1.3	Charging and force of microparticle in plasmas	8
1.4	Illustration of channeling effect in a sodium iodide (NaI) crystal	15
2.1	Photo of “adaptive” electrode chamber	19
2.2	Process of Coulomb explosion experiment	20
2.3	Microparticles in the discharge at different rf frequencies	22
3.1	Photo of PK-3 Plus chamber in the laboratory on the ground	24
3.2	Spin of an aggregate suspended in the plasma	25
4.1	Sketch of a Mach cone	28
4.2	Photo of GEC reference chamber	29
4.3	Comparison of the wave features between type I and type II Mach cones	30
4.4	Illustration of channeling effect in a bent 2D crystal lattice	31
5.1	Demonstration of lane formation of pedestrian.	34
5.2	Photo of PK-3 Plus chamber on board the ISS	36
5.3	Samples of lane structure.	37
5.4	Illustration of ASIM and CRM for quantification of lane structure	38
5.5	Comparison between the space experiments and the ground experiments	40

Bibliography

- [1] J.E. Allen, *Physica Scripta* **45** (1992), 497.
- [2] J.E. Allen, B.M. Annaratone and U. de Angelis, *J. Plasma Phys.* **63** (2000), 299.
- [3] J.E. Allen, R.L.F. Boyd and P. Reynolds, *Proceedings of the Physical Society. Section B* **70** (1957), 297.
- [4] M. Allen and D.J. Tildesley: *Computer Simulation of Liquids*. Oxford University Press, Oxford, 1987.
- [5] T. Antonova: *Interaction of particles with complex Interactions of Particles with Complex Electrostatic Structures and 3D Clusters*. Munich, Ludwig-Maximilian-Universität München, PhD Thesis, 2007.
- [6] O. Arp, D. Block, A. Piel and A. Melzer, *Phys. Rev. Lett.* **93** (2004), 165004.
- [7] L. Assoud, F. Ebert, P. Keim, R. Messina, G. Maret and H. Löwen, *Phys. Rev. Lett.* **102** (2009), 238301.
- [8] M. Bacharis, M. Coppins and J.E. Allen, *Plasma Sources Science and Technology* **19** (2010), 025002.
- [9] M.F. Baines, I.P. Williams and A.S. Asebiomo, *Monthly Notices of the Royal Astronomical Society* **130** (1965), 63.
- [10] R. Basner, F. Sigeneger, D. Loffhagen, G. Schubert, H. Fehske and H. Kersten, *New Journal of Physics* **11** (2009), 013041.
- [11] W. Baumjohann and R.A. Treumann: *Basic Space Plasma Physics*. World Scientific Publishing, Singapore, 1996.
- [12] A. Baurichter, C. Biino, M. Clément, N. Doble, K. Elsener, G. Fidecaro, A. Freund, L. Gatignon, P. Grafström, M. Gyr, M. Hage-Ali, W. Herr, P. Keppler, K. Kirsebom, J. Klem, J. Major, R. Medenwaldt, U. Mikkelsen, S. Møller, P. Siffert, E. Uggerhøj, Z. Vilakazi and E. Weisse, *Nuclear Instruments and Methods in Physics Research Section B: Beam Interactions with Materials and Atoms* **164 - 165** (2000), 27 .

-
- [13] C.K. Birdsall and A.B. Langdon, editors. *Plasma Physics via Computer Simulation*. Hilger, Bristol and Philadelphia, 1991.
- [14] V.M. Biryukov, Y.A. Chesnokov and V.I. Kotov: *Crystal Channeling and Its Application at High-Energy Accelerators*. Springer, Berlin and Heidelberg, 2010.
- [15] J. Bittencourt: *Fundamentals of Plasma Physics*. Springer, New York, 2004.
- [16] A. Bouchoule, editor. *Dusty Plasmas: Physics, Chemistry, and Technological Impact in Plasma Processing*. Wiley, Chichester, Jul 1999.
- [17] O. Bystrenko and A. Zagorodny, *Phys. Rev. E* **67** (2003), 066403.
- [18] H.W. Carlson and D.J. Maglieri, *The Journal of the Acoustical Society of America* **51** (1972), 675.
- [19] B. Chapman: *Glow Discharge Processes: Sputtering and Plasma Etching*. Wiley, New York, 1980.
- [20] M. Chaudhuri, A.V. Ivlev, S.A. Khrapak, H.M. Thomas and G.E. Morfill, *Soft Matter* **7** (2011), 1287.
- [21] F. Chen: *Plasma Physics and Controlled Fusion*. Plenum Press, New York and London, 1984.
- [22] V. Chidambaram, H. Yeung and G. Shan, *Journal of Electronic Materials* **41** (2012), 2107. 10.1007/s11664-012-2114-6.
- [23] V.W. Chow, D.A. Mendis and M. Rosenberg, *J. Geophys. Res.* **98** (1993), 19065.
- [24] J.H. Chu and L. I, *Phys. Rev. Lett.* **72** (1994), 4009.
- [25] J.E. Colwell, S. Batiste, M. Hornyi, S. Robertson and S. Sture, *Rev. Geophys.* **45** (2007), RG2006.
- [26] L. Couédel, V. Nosenko, A.V. Ivlev, S.K. Zhdanov, H.M. Thomas and G.E. Morfill, *Phys. Rev. Lett.* **104** (2010), 195001.
- [27] L. Couédel, V. Nosenko, S.K. Zhdanov, A.V. Ivlev, H.M. Thomas and G.E. Morfill, *Phys. Rev. Lett.* **103** (2009), 215001.
- [28] I.D. Couzin and N.R. Franks, *Proc. R. Soc. Lond. B* **270** (2003), 139.
- [29] V.I. Demidov, S.V. Ratynskaia and K. Rypdal, *Review of Scientific Instruments* **73** (2002), 3409.
- [30] N. Doble, L. Gatignon and P. Grafström, *Nuclear Instruments and Methods in Physics Research Section B: Beam Interactions with Materials and Atoms* **119** (1996), 181 .

- [31] B.T. Draine and E.E. Salpeter, *Astrophysical Journal* **231** (1979), 438.
- [32] C.R. Du: *Coulomb Explosion and Agglomeration in Complex Plasma*. Garching, Technische Universität München, Master Thesis, 2009.
- [33] J. Dzubiella, G.P. Hoffmann and H. Löwen, *Phys. Rev. E* **65** (2002), 021402.
- [34] P.S. Epstein, *Phys. Rev.* **23** (1924), 710.
- [35] L.C. Feldman, J.W. Mayer and S.T. Picraux: *Materials analysis by ion Channeling*. Academic Press, New York, 1982.
- [36] A. Filippov, N. Dyatko, A. Pal' and A. Starostin, *Plasma Physics Reports* **29** (2003), 190. 10.1134/1.1561112.
- [37] R.P. Fliller, A. Drees, D. Gassner, L. Hammons, G. McIntyre, S. Peggs, D. Trbojevic, V. Biryukov, Y. Chesnokov and V. Terekhov, *Phys. Rev. ST Accel. Beams* **9** (2006), 013501.
- [38] V. Fortov, A. Ivlev, S. Khrapak, A. Khrapak and G. Morfill, *Physics Reports* **421** (2005), 1 .
- [39] V. Fortov, G. Morfill, O. Petrov, M. Thoma, A. Usachev, H. Hoefner, A. Zobnin, M. Kretschmer, S. Ratynskaia, M. Fink, K. Tarantik, Y. Gerasimov and V. Esenkov, *Plasma Physics and Controlled Fusion* **47** (2005), B537.
- [40] V.E. Fortov, A.G. Khrapak, S.A. Khrapak, V.I. Molotkov and O.F. Petrov, *Physics-Uspekhi* **47** (2004), 447.
- [41] V.E. Fortov and G.E. Morfill: *Complex and Dusty Plasmas: From Laboratory to Space*. Plasma Physics. CRC Press, Boca Raton, 2010.
- [42] D. Frank-Kamenezki: *Plasma – der vierte Aggregatzustand*. Progress, Moscow, 1963.
- [43] V.A. Godyak: *Soviet Radio Frequency Discharge Research*. Delphic Associates, Falls Church, 1986.
- [44] J. Goree, *Plasma Sources Science and Technology* **3** (1994), 400.
- [45] E. Grün, C. Goertz, G. Morfill and O. Havnes, *Icarus* **99** (1992), 191 .
- [46] E. Grün, B. Gustafson, S. Dermott and H. Fechtig, editors. *Interplanetary*. Springer, Berlin, 2001.
- [47] Y. Hayashi and K. Tachibana, *Japanese Journal of Applied Physics* **33** (1994), L804.
- [48] R. Heidemann, S. Zhdanov, K.R. Sütterlin, H.M. Thomas and G.E. Morfill, *EPL (Europhysics Letters)* **96** (2011), 15001.

- [49] M. Horányi, *Ann. Rev. Astron. Astrophys.* **34** (1996), 383 .
- [50] I.H. Hutchinson, *Plasma Phys. Control. Fusion* **45** (2003), 1477.
- [51] I.H. Hutchinson, *Plasma Phys. Control. Fusion* **47** (2005), 71.
- [52] I.H. Hutchinson and L. Patacchini, *Phys. Plasmas* **14** (2007), 013505.
- [53] A.V. Ivlev, S.A. Khrapak, S.K. Zhdanov, G.E. Morfill and G. Joyce, *Phys. Rev. Lett.* **92** (2004), 205007.
- [54] A.V. Ivlev, H. Löwen, G.E. Morfill and C.P. Royall: *Complex Plasmas and Colloidal Dispersions*. World Scientific Publishing, London, 2012.
- [55] A.V. Ivlev, S.K. Zhdanov, H.M. Thomas and G.E. Morfill, *EPL* **85** (2009), 45001.
- [56] K. Jiang: *Particle Manipulation in Plasma Device & Dynamics of Binary Complex Plasma*. Munich, Ludwig-Maximilian-Universität München, PhD Thesis, 2011.
- [57] K. Jiang, C.R. Du, K.R. Sütterlin, A.V. Ivlev and G.E. Morfill, *EPL* **92** (2010), 65002.
- [58] K. Jiang, L.J. Hou, A.V. Ivlev, Y.F. Li, C.R. Du, H.M. Thomas, G.E. Morfill and K.R. Sütterlin, *EPL (Europhysics Letters)* **93** (2011), 55001.
- [59] K. Jiang, V. Nosenko, Y.F. Li, M. Schwabe, U. Konopka, A.V. Ivlev, V.E. Fortov, V.I. Molotkov, A.M. Lipaev, O.F. Petrov, M.V. Turin, H.M. Thomas and G.E. Morfill, *EPL (Europhysics Letters)* **85** (2009), 45002.
- [60] R.A. Jones: *Soft Condensed Matter*. Oxford University Press, New York, 2002.
- [61] G. Joyce, M. Lampe, S.P. Slinker and W.M. Manheimer, *Journal of Computational Physics* **138** (1997), 540 .
- [62] T. Kawasaki, T. Araki and H. Tanaka, *Phys. Rev. Lett.* **99** (2007), 215701.
- [63] J.W. Kephart: *Beyond the Continuum Potential Approximation: Channeling Radiation from Nonideal Crystals*. Stanford University, PhD Thesis, 1987.
- [64] S.A. Khrapak, A.V. Ivlev and G.E. Morfill, *Phys. Rev. E* **70** (2004), 056405.
- [65] S.A. Khrapak, A.V. Ivlev, G.E. Morfill and H.M. Thomas, *Phys. Rev. E* **66** (2002), 046414.
- [66] S.A. Khrapak and G.E. Morfill, *Physics of Plasmas* **15** (2008), 084502.
- [67] S.A. Khrapak and G.E. Morfill, *Contributions to Plasma Physics* **49** (2009), 148.
- [68] S.A. Khrapak and G.E. Morfill, *Physics of Plasmas* **19** (2012), 024510.

- [69] W. Klingsch, C. Rogsch, A. Schadschneider and M. Schreckenberg, editors. *Pedestrian and Evacuation Dynamics 2008*. Springer, Berlin and Heidelberg, 2010.
- [70] U. Konopka: *Wechselwirkungen geladener Staubteilchen in Hochfrequenzplasmen*. Ruhr-Universität-Bochum, PhD Thesis, 2000.
- [71] U. Konopka, L. Ratke and H.M. Thomas, *Phys. Rev. Lett.* **79** (1997), 1269.
- [72] M. Lampe, R. Goswami, Z. Sternovsky, S. Robertson, V. Gavrishchaka, G. Ganguli and G. Joyce, *Phys. Plasmas* **10** (2003), 1500.
- [73] I. Langmuir, *Phys. Rev.* **21** (1923), 419.
- [74] M. Laroussi, M.G. Kong, G.E. Morfill and W. Stolz, editors. *Plasma Medicine: Applications of Low-Temperature Gas Plasmas in Medicine and Biology*. Cambridge University Press, Cambridge, 2012.
- [75] D.S. Lemons: *An Introduction to Stochastic Processes in Physics*. John Hopkins University Press, Baltimore, 2002.
- [76] M.E. Leunissen, C.G. Christova, A.P. Hynninen, C.P. Royall, A.I. Campbell, A. Imhof, M. Dijkstra, R. van Roij and A. van Blaaderen, *Nature* **437** (2005), 235.
- [77] M.A. Lieberman and A.J. Lichtenberg: *Principles of Plasma Discharges and Materials Processing*. 2. edition. Wiley, Hoboken, 2005.
- [78] B. Liu, J. Goree, V. Nosenko and L. Boufendi, *Physics of Plasmas* **10** (2003), 9.
- [79] T. Makabe: *Advances in Low Temperature RF Plasmas: Basis for Process Design*. Elsevier, Amsterdam, 2002.
- [80] L.S. Matthews, V. Land, Q. Ma, J.D. Perry and T.W. Hyde, *AIP Conference Proceedings* **1397** (2011), 60.
- [81] A. Melzer, T. Trottenberg and A. Piel, *Physics Letters A* **191** (1994), 301 .
- [82] K.O. Menzel, O. Arp and A. Piel, *Phys. Rev. E* **83** (2011), 016402.
- [83] G. Morfill and C. Goertz, *Icarus* **55** (1983), 111 .
- [84] G.E. Morfill and A.V. Ivlev, *Reviews of Modern Physics* **81** (2009), 1353.
- [85] H.M. Mott-Smith and I. Langmuir, *Phys. Rev.* **28** (1926), 727.
- [86] W.H. Munk, P. Scully-Power and F. Zachariasen, *Proceedings of the Royal Society of London. A. Mathematical and Physical Sciences* **412** (1987), 231.
- [87] R.R. Netz, *EPL* **63** (2003), 616.

- [88] J. Nickolls and W. Dally, *Micro, IEEE* **30** (2010), 56 .
- [89] T. Nitter, *Plasma Sources Science and Technology* **5** (1996), 93.
- [90] T. Northrop and T. Birmingham, *Planetary and Space Science* **38** (1990), 319 .
- [91] V. Nosenko, J. Goree, Z.W. Ma, D.H.E. Dubin and A. Piel, *Phys. Rev. E* **68** (2003), 056409.
- [92] V. Nosenko, A.V. Ivlev and G.E. Morfill, *Phys. Rev. Lett.* **108** (2012), 135005.
- [93] V. Nosenko, A.V. Ivlev, S.K. Zhdanov, M. Fink and G.E. Morfill, *Physics of Plasmas* **16** (2009), 083708.
- [94] S. Nunomura, J. Goree, S. Hu, X. Wang and A. Bhattacharjee, *Phys. Rev. E* **65** (2002), 066402.
- [95] S. Nunomura, S. Zhdanov, D. Samsonov and G. Morfill, *Phys. Rev. Lett.* **94** (2005), 045001.
- [96] Y.P. Raizer: *Gas Discharge Physics*. Springer, Berlin and Heidelberg, 1991.
- [97] N. Rao, P. Shukla and M. Yu, *Planetary and Space Science* **38** (1990), 543 .
- [98] C. R ath, W. Bunk, M.B. Huber, G.E. Morfill, J. Retzlaff and P. Schuecker, *Monthly Notices of the Royal Astronomical Society* **337** (2002), 413.
- [99] M. Rex and H. L wen, *EPL* **26** (2008), 143.
- [100] T.B. R cker, S.K. Zhdanov, A.V. Ivlev, M. Lampe, G. Joyce and G.E. Morfill, *Physics of Plasmas* **19** (2012), 073708.
- [101] M. Rosenberg, D. Mendis and D. Sheehan, *Plasma Science, IEEE Transactions on* **24** (1996), 1422 .
- [102] M. Rosenberg, D. Mendis and D. Sheehan, *Plasma Science, IEEE Transactions on* **27** (1999), 239 .
- [103] H. Rothermel, T. Hagl, G.E. Morfill, M.H. Thoma and H.M. Thomas, *Phys. Rev. Lett.* **89** (2002), 175001.
- [104] M. Rubin-Zuzic, H.M. Thomas, S.K. Zhdanov and G.E. Morfill, *New Journal of Physics* **9** (2007), 39.
- [105] D. Samsonov, J. Goree, Z.W. Ma, A. Bhattacharjee, H.M. Thomas and G.E. Morfill, *Phys. Rev. Lett.* **83** (1999), 3649.
- [106] D. Samsonov, J. Goree, H.M. Thomas and G.E. Morfill, *Phys. Rev. E* **61** (2000), 5557.

- [107] A. Schadschneider, *Physics World* (2010).
- [108] W. Schröder, *Bulletin of the American Meteorological Society* **82** (2001), 2457.
- [109] M. Schwabe: *Dynamical Effects in Fluid Complex Plasmas*. Munich, Ludwig-Maximilian-Universität München, PhD Thesis, 2009.
- [110] M. Schwabe, K. Jiang, S. Zhdanov, T. Hagl, P. Huber, A.V. Ivlev, A.M. Lipaev, V.I. Molotkov, V.N. Naumkin, K.R. Sütterlin, H.M. Thomas, V.E. Fortov, G.E. Morfill, A. Skvortsov and S. Volkov, *EPL (Europhysics Letters)* **96** (2011), 55001.
- [111] M. Schwabe, M. Rubin-Zuzic, S. Zhdanov, H.M. Thomas and G.E. Morfill, *Phys. Rev. Lett.* **99** (2007), 095002.
- [112] I.V. Schweigert and V.A. Schweigert, *Plasma Sources Science and Technology* **13** (2004), 315.
- [113] G.S. Selwyn, J.E. Heidenreich and K.L. Haller, *Journal of Vacuum Science & Technology A: Vacuum, Surfaces, and Films* **9** (1991), 2817.
- [114] P. Shukla and A. Mamun: *Introduction to Dusty Plasma Physics*. Institute of Physics Publishing, Bristol and Philadelphia, 2002.
- [115] B.A. Smith, L. Soderblom, R. Batson, P. Bridges, J. Inge, H. Masursky, E. Shoemaker, R. Beebe, J. Boyce, G. Briggs, A. Bunker, S.A. Collins, C.J. Hansen, T.V. Johnson, J.L. Mitchell, R.J. Terrile, A.F. Cook, J. Cuzzi, J.B. Pollack, G.E. Danielson, A.P. Ingersoll, M.E. Davies, G.E. Hunt, D. Morrison, T. Owen, C. Sagan, J. Veverka, R. Strom and V.E. Suomi, *Science* **215** (1982), 504.
- [116] K.R. Sütterlin, H.M. Thomas, A.V. Ivlev, G.E. Morfill, V.E. Fortov, A.M. Lipaev, V.I. Molotkov, O.F. Petrov, A. Wysocki and H. Löwen, *IEEE Transactions on Plasma Science* **38** (2010), 861.
- [117] K.R. Sütterlin, A. Wysocki, A.V. Ivlev, C. Räth, H.M. Thomas, M. Rubin-Zuzic, W.J. Goedheer, V.E. Fortov, A.M. Lipaev, V.I. Molotkov, O.F. Petrov, G.E. Morfill and H. Löwen, *Phys. Rev. Lett.* **102** (2009), 085003.
- [118] L. Talbot, R.K. Cheng, R.W. Schefer and D.R. Willis, *Journal of Fluid Mechanics* **101** (1980), 737.
- [119] H. Thomas, G.E. Morfill, V. Demmel, J. Goree, B. Feuerbacher and D. Möhlmann, *Phys. Rev. Lett.* **73** (1994), 652.
- [120] H.M. Thomas, G.E. Morfill, V.E. Fortov, A.V. Ivlev, V.I. Molotkov, A.M. Lipaev, T. Hagl, H. Rothermel, S.A. Khrapak, R.K. Suetterlin, M. Rubin-Zuzic, O.F. Petrov, V.I. Tokarev and S.K. Krikalev, *New Journal of Physics* **10** (2008), 033036.

-
- [121] T. Trottenberg, A. Melzer and A. Piel, *Plasma Sources Science and Technology* **4** (1995), 450.
- [122] D. Tskhakaya, K. Matyash, R. Schneider and F. Taccogna, *Contributions to Plasma Physics* **47** (2007), 563.
- [123] V.N. Tsytovich and J. Winter, *Physics-Uspekhi* **41** (1998), 815.
- [124] M.M. Turner, *Physics of Plasmas* **13** (2006), 033506.
- [125] V. Vahedi and M. Surendra, *Computer Physics Communications* **87** (1995), 179 .
- [126] J.P. Verboncoeur, *Plasma Physics and Controlled Fusion* **47** (2005), A231.
- [127] T. Vissers, A. Wysocki, M. Rex, H. Löwen, C.P. Royall, A. Imhof and A. van Blaaderen, *Soft Matter* **7** (2011), 2352.
- [128] A. Wysocki and H. Löwen, *Journal of Physics: Condensed Matter* **16** (2004), 7209.
- [129] V. Yaroshenko, S. Ratynskaia, S. Khrapak, M.H. Thoma, M. Kretschmer, H. Höfner, G.E. Morfill, A. Zobnin, A. Usachev, O. Petrov and V. Fortov, *Physics of Plasmas* **12** (2005), 093503.

Publication list

Publications on peer reviewed journals. The first nine publications correspond to the research done during PhD study in Max Planck Institute for Extraterrestrial Physics. The last two publications correspond to the research done during undergraduate study in Shanghai Jiao Tong University.

1. T. Antonova, C.-R. Du, B.M. Annaratone, L.-J. Hou, R. Kompaneets, H.M. Thomas, and G.E. Morfill, *Microparticles deep in the plasma sheath: Coulomb “explosion”*, Phys. Plasmas 19, 093709 (2012)
2. C.-R. Du, V. Nosenko, S. Zhdanov, H.M. Thomas, and G.E. Morfill, *Interaction of two-dimensional plasma crystals with upstream charged particles*, Europhys. Lett. 99, 55001 (2012)
3. C.-R. Du, K.R. Sütterlin, A.V. Alexei, H.M. Thomas and G.E. Morfill, *Model experiment for studying lane formation in binary complex plasmas*, Europhys. Lett. 99, 45001 (2012)
4. C.-R. Du, K.R. Sütterlin, K. Jiang, C. R ath, A.V. Ivlev, S. Khrapak, M. Schwabe, H.M. Thomas, V.E. Fortov, A.M. Lipaev, V.I. Molotkov, O.F. Petrov, Y. Malentschenko, F. Yurtschichin, Y. Lonchakov, and G.E. Morfill, *Experimental investigation on lane formation in complex plasmas under microgravity conditions*, New J. Phys. 14, 073058 (2012)
5. C.-R. Du, S.A. Khrapak, T. Antonova, B. Steffes, H.M. Thomas, and G.E. Morfill, *Frequency dependence of microparticle charge in a radio frequency discharge with Margenau electron velocity distribution*, Phys. Plasmas 18, 014501 (2011)
6. K. Jiang, L.-J. Hou, A.V. Alexei, Y.-F. Li, C.-R. Du, H.M. Thomas, G.E. Morfill, and K.R. S tterlin, *Initial stages in phase separation of binary complex plasmas: Numerical experiments*, Europhys. Lett. 93, 55001 (2011)
7. K. Jiang, C.-R. Du, K.R. S tterlin, A.V. Alexei and G.E. Morfill, *Lane formation in binary complex plasmas: Role of non-additive interactions and initial configurations*, Europhys. Lett. 92, 65002 (2010)

8. C.-R. Du, H.M. Thomas, A.V. Ivlev, U. Konopka, and G.E. Morfill, *Agglomeration of microparticles in complex plasmas*, Phys. Plasmas 17, 113710 (2010)
9. B.M. Annaratone, T. Antonova, C. Arnas, P. Bandyopadhyay, M. Chaudhuri, C.-R. Du, Y.ZElskens, A.V. Ivlev, G.E. Morfill, V. Nosenko, K.R. Sütterlin, M. Schwabe, and H.M. Thomas *Collective effects in complex plasma*, Plasma Sources Sci. Technol. 19, 065026 (2010)
10. C.-R. Du and K.-D. Zhu, *Temperature dependence of violation of Bell's inequality in coupled quantum dots in a microcavity*, Appl. Phys. B 95, 675-683 (2009)
11. C.-R. Du and K.-D. Zhu, *Phonon effect on two coupled quantum dots at finite temperature*, Phys. Lett. A 372, 537-540 (2008)

Curriculum vitae

Chengran Du

Max Planck Institute for Extraterrestrial Physics
Giessenbachstr., 85748 Garching, Germany
Email: chengran.du@mpe.mpg.de
Telephone: +49-89-30003012

Birthday: 16. Dec 1984
Birthplace: Shanghai, China

Education

- 10/2009 - present Theory and Complex Plasma Group
Max Planck Institute for Extraterrestrial Physics, Germany
PhD candidate (Supervisor: Prof. G.E. Morfill)
Majoring in Physics
- 10/2007 - 06/2009 Department of Physics
Technische Universität München, Germany
Master of Science (Supervisor: Prof. G. Hasinger)
Majoring in Engineering Physics
- 09/2003 - 08/2007 Department of Physics
Shanghai Jiao Tong University, China
Bachelor of Science (Supervisor: Prof. K.-D. Zhu)
Majoring in Applied Physics
- 03/2006 - 08/2006 Department of Physics
Universität des Saarlands, Germany
Exchange Student
Majoring in Physics
- 08/2005 - 12/2005 Department of Physics
National University of Singapore, Singapore
Exchange Student
Majoring in Physics

Research Experience

- 11/2007 - 05/2008 E19, Department of Physics
Technische Universität München, Germany
Work Student (Supervisor: Prof. U. Stimming)
Preparation of gold tips suitable for STM by electrochemical etching
- 05/2006 - 08/2006 AG Hartmann, Department of Physics
Universität des Saarlands, Germany
Work Student (Supervisor: Dr. H.-B. Gao)
3D animation for demonstration of geomagnetic sensor at FRA
- 10/2005 - 12/2005 Colloid Laboratory, Department of Physics
National University of Singapore, Singapore
Research Assistant (Supervisor: Prof. C.H. Sow)
Micro-Topiary: Laser pruning of carbon nanotubes arrays

Conference

- 07/2012 39th IEEE International Conference on Plasma Science, UK
Poster Presentation
*Interaction of 2D plasma crystals with upstream charged particle:
Mach cones and channeling effect*
- 05/2011 6th International Conference on the Physics of Dusty Plasmas, Germany
Poster Presentation
*Role of non-additivity interactions and initial configurations in
lane formation in binary complex plasmas*
- 11/2010 52nd Annual Meeting of the APS Division of Plasma Physics, USA
Contributed Talk
Agglomeration of microparticles in complex plasmas
- 06/2010 Lindau Nobel Laureate Meetings 2010, Germany
Participation
- 03/2010 DPG Spring Meeting 2010 of the Section AMOP, Germany
Contributed Talk
Dust agglomeration induced by self-excited waves in a complex plasma
- 09/2009 2nd Workshop on Diagnostics and Simulation of Dusty Plasmas, Germany
Contributed Talk
Dust agglomeration in a complex plasma

Enclosed papers

This cumulative thesis consists of seven papers, which are reprinted below with permission from American Institute of Physics (AIP) and Institute of Physics (IOP).

1. T. Antonova, C.-R. Du, B.M. Annaratone, L.-J. Hou, R. Kompaneets, H.M. Thomas, and G.E. Morfill, *Microparticles deep in the plasma sheath: Coulomb “explosion”*, Phys. Plasmas 19, 093709 (2012). Copyright: AIP.
2. C.-R. Du, S.A. Khrapak, T. Antonova, B. Steffes, H.M. Thomas, and G.E. Morfill, *Frequency dependence of microparticle charge in a radio frequency discharge with Margenau electron velocity distribution*, Phys. Plasmas 18, 014501 (2011). Copyright: AIP.
3. C.-R. Du, H. M. Thomas, A.V. Ivlev, U. Konopka, and G.E. Morfill, *Agglomeration of microparticles in complex plasmas*, Phys. Plasmas 17, 113710 (2010). Copyright: AIP.
4. C.-R. Du, V. Nosenko, S. Zhdanov, H.M. Thomas, and G.E. Morfill, *Interaction of two-dimensional plasma crystals with upstream charged particles*, Europhys. Lett. 99, 55001 (2012). Copyright: IOP.
5. K. Jiang, C.-R. Du, K.R. Sütterlin, A.V. Alexei and G.E. Morfill, *Lane formation in binary complex plasmas: Role of non-additive interactions and initial configurations*, Europhys. Lett. 92, 65002 (2010). Copyright: IOP.
6. C.-R. Du, K.R. Sütterlin, K. Jiang, C. Räch, A.V. Ivlev, S. Khrapak, M. Schwabe, H.M. Thomas, V.E. Fortov, A.M. Lipaev, V.I. Molotkov, O.F. Petrov, Y. Malentschenko, F. Yurtschichin, Y. Lonchakov, and G.E. Morfill, *Experimental investigation on lane formation in complex plasmas under microgravity conditions*, New J. Phys. 14, 073058 (2012). Copyright: IOP.
7. C.-R. Du, K.R. Sütterlin, A.V. Alexei, H.M. Thomas and G.E. Morfill, *Model experiment for studying lane formation in binary complex plasmas*, Europhys. Lett. 99, 45001 (2012). Copyright: IOP.

Microparticles deep in the plasma sheath: Coulomb “explosion”

T. Antonova,^{1,a)} C.-R. Du,¹ A. V. Ivlev,¹ B. M. Annaratone,^{2,b)} L.-J. Hou,¹ R. Kompaneets,³ H. M. Thomas,¹ and G. E. Morfill¹

¹Max-Planck-Institut für Extraterrestrische Physik, D-85741 Garching, Germany

²PIIM, UMR6633 CNRS/Université de Provence, Campus St. Jérôme F-13397, Marseille, France

³School of Physics, The University of Sydney, Sydney, New South Wales 2006, Australia

(Received 26 July 2012; accepted 5 September 2012; published online 26 September 2012)

A cloud of microparticles was trapped deep in the sheath of a radio-frequency (rf) discharge, very close to the lower (grounded) electrode of the plasma chamber. This was achieved by employing a specifically designed rf-driven segment integrated in the lower electrode, which provided an additional confinement compressing the cloud to a very high density. After switching the rf-driven segment off, the cloud “exploded” due to mutual interparticle repulsion. By combining a simple theoretical model with different numerical simulation methods, some basic properties of complex plasmas in this highly non-equilibrium regime were determined. © 2012 American Institute of Physics. [<http://dx.doi.org/10.1063/1.4754007>]

I. INTRODUCTION

When microparticles are introduced in a plasma, they usually acquire negative charges (due to mobile electrons) and, hence, a negative potential with respect to the surrounding plasma.^{1,2} The magnitude of the charge is mainly determined by the balance of the electron and ion currents on a particle surface. The particles are pulled down, first of all, by the gravity force. But in the pre-electrode region (plasma sheath), a strong inhomogeneous electric field pointed downwards is present. Therefore, negatively charged microparticles are able to levitate in the sheath region, as sketched in Fig. 1 (“normal” levitation), where there is still enough electrons for their charging and, at the same time, the electric field is sufficiently strong to support them against gravity.^{3–6} Light submicron particles can even levitate in the plasma bulk.⁷

In this contribution, we present very special experimental conditions which allow us to observe the dust particles in a completely new and unusual location inside the plasma—very deep in the sheath, levitating in a close proximity to the chamber electrode. The experiments were carried out by employing a specifically designed rf-driven segment⁸ integrated in the lower (grounded) electrode of the plasma chamber, as illustrated in Fig. 1. In this case, the particles find themselves in the extreme state which differs dramatically from other regimes observed so far with complex plasmas. The dust cloud is “compressed” by an additional confinement (generated by the rf-segment) up to very high densities. The particular feature of the setup is that after the confinement is switched off abruptly, the dust cloud “explodes” due to mutual interparticle repulsion.

The principal aim of this work is to study basic properties of complex plasmas in such extreme conditions. In our experiments, the compressed particle cloud was located in the sheath region very close to the lower electrode (around 1–1.5 mm above the electrode, while “normal” levitation height was about 5 mm). In order to determine the particle

charge, we combined a simple theoretical model with different numerical simulation methods, which allowed us to evaluate the plasma parameters directly at the location of the particle cloud.

II. EXPERIMENT

The experiments were performed in the chamber which consists of two parallel-plate electrodes of 3.8 cm diameter, separated by the distance of 3 cm (see Fig. 1). The upper electrode is rf driven at 13.56 MHz with 300 V peak-to-peak amplitude. The lower, so-called “adaptive” electrode⁸ is divided into 57 small segments (of 3.8×3.8 mm² size each), with the possibility to apply rf or/and dc (direct current) voltage to individual segments. During our experiments, the adaptive electrode was grounded except for one segment, where rf voltage was applied in phase with the upper driven electrode. As shown in Fig. 2(a), this ignited a small ($\simeq 40$ mm³) localized plasma spot above the segment, within the sheath of the main rf plasma. The injected melamine formaldehyde particles of 4.8 μ m diameter were attracted into the plasma spot. The density and shape of the resulting cloud as well as the particle distribution inside it was controlled by the amplitude and phase of the rf voltage applied to the segment (for experiments discussed here, we used 245 V peak-to-peak amplitude). Thus, the segmented electrode provided us with a powerful tool for the particle manipulation in the plasma.^{8–10}

In our experiments we obtained dense particle clouds confined in the plasma spot. The clouds typically contained about 5000 particles and had a shape of a slightly bent disk (of diameter 2–3 mm and thickness $\simeq 1$ mm). When the voltage at the rf segment was switched off [see Fig. 2(b)] the particle cloud “exploded”, expanding into the main plasma sheath. After being released, microparticles reached their equilibrium positions in the sheath within approximately 0.2 s. The experiments were performed in argon gas at pressures of 30, 55, and 100 Pa. The particles were illuminated using a diode laser with 681 nm wavelength fanned out in a vertical plane, and recorded by the high-speed Photron video

^{a)}Electronic mail: antonova@mpe.mpg.de.

^{b)}Deceased.

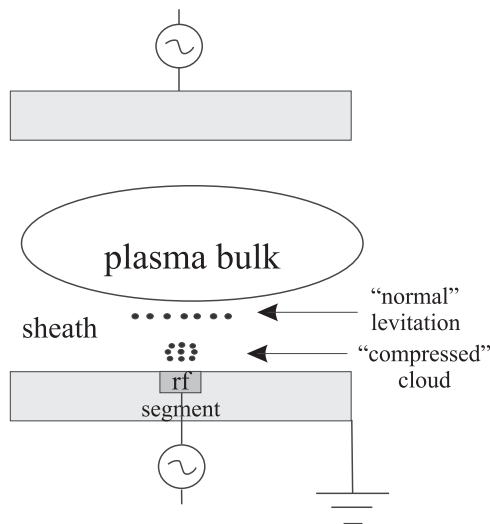


FIG. 1. Sketch of the rf discharge, showing the “normal” particle levitation in a sheath, and the “compressed” particle cloud near the lower electrode (when the additional rf-driven segment is switched on).

camera with the frame rate of 3000 frames/s. Velocities of individual particles were measured by tracking them in consecutive frames (using an automatic particle tracking algorithm with the accuracy of less than a half of a pixel).

The dust cloud explosion has been previously observed in the experiment by Barkan and Merlino,¹¹ where polydisperse particles were initially trapped in an anode double layer produced in a Q-machine. The authors explained the particle acceleration observed after their release by the electrostatic force due to the total charge of the dust cloud. The single particle charge in this case was estimated from the measured parameters of the plasma confinement. In our present work,

we estimate the charge of particles at their location (very deep in the sheath) *after* the explosion has started. For this purpose, we combine the experimental data with numerical simulations and theoretical analysis.

III. PIC SIMULATION AND SIMPLE THEORETICAL ANALYSIS

The particle-in-cell Monte Carlo collision (PIC-MCC) simulations are an extremely powerful tool to describe and understand a wide range of plasma phenomena.¹² Ions and electrons move under the action of externally imposed and self-generated forces. The electrostatic field is calculated by solving Poisson’s equation, with the charge density source term determined by the laydown of the densities of electrons and ions. Plasma parameters can be extracted directly from the simulation with a high spatial and temporal resolution. Our simulations were based on the standard 1D3V PIC-MCC method,¹³ in which the lower electrode (at the height $y=0$) was grounded and the upper one (at $y=3$ cm) was rf driven. This setup corresponds to the experimental conditions when the additional rf-driven segment is switched off.

We performed the simulations for three different pressures studied experimentally. The obtained local plasma parameters at 1.5 mm height above the lower electrode are summarized in Table I. One can see that the ion and electron densities defer pretty much at this position, and the sheath electric field is very strong. Furthermore, for all three cases the ion flow velocity is highly suprathermal, $M_T \gg 1$, and the characteristic scale of the field inhomogeneity is much larger than the ion mean free path, $l_E \gg l_i$. This enables us to employ a simple theoretical analysis to estimate charging

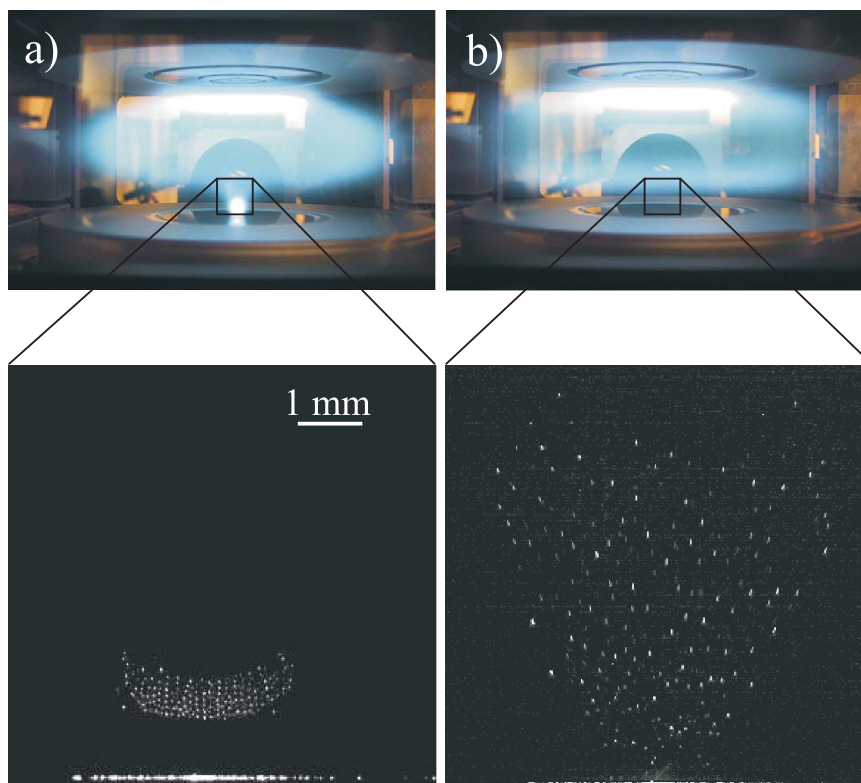


FIG. 2. Illustration of the discharge (a) with the small plasma spot generated by the rf-driven segment, and (b) right after switching off the rf segment. The lower panel shows the corresponding snapshots of (a) stable and (b) expanding particle clouds.

TABLE I. The local plasma parameters at the particle positions in the sheath, at the height $y = 1.5$ mm above the lower electrode, obtained from PIC simulations for different pressures. $M_T = u_i/v_{T_n}$ is the thermal Mach number expressed via the ion flow velocity u_i and the neutral thermal velocity $v_{T_n} = \sqrt{T_n/m_n}$, E is the sheath electric field, $l_E = |E/(dE/dy)|$ is the length scale of the field inhomogeneity (in the vertical direction), l_i is the ion mean free path, n_e and n_i are the electron and ion densities, respectively, T_e and T_i are the corresponding temperatures. The ion temperature was defined via the dispersion of the ion distribution function, $T_i = \frac{1}{3}m_i\langle(v - \mathbf{u}_i)^2\rangle$.

	30 Pa	55 Pa	100 Pa
M_T	15	11	8.1
E [V/cm]	49	54	60
l_E [cm]	0.54	0.46	0.33
l_i [cm]	2.1×10^{-2}	1.1×10^{-2}	6×10^{-3}
n_e [cm $^{-3}$]	3.2×10^6	5×10^6	1.3×10^7
n_i [cm $^{-3}$]	5.3×10^7	6.9×10^7	1.13×10^8
T_e [eV]	1.3	1.3	1.25
T_i [eV]	0.087	0.068	0.045

characteristics at the beginning of expansion, based on the balance of ion and electron currents on the particle surface. The electron current is calculated from the orbital motion limited theory (OML)¹

$$I_e = \sqrt{8\pi a^2 n_e v_{T_e}} \exp(-z), \quad (1)$$

where a is the dust particle radius, $z = e|Q|/aT_e$ is the normalized magnitude of the particle charge Q , and $v_{T_e} = \sqrt{T_e/m_e}$ is electron thermal velocity. For the sake of simplicity, the ion current is derived assuming a displaced Maxwellian velocity distribution (see discussion in the end of Sec. IV) and taking into account that $M_T \gg 1$

$$I_i \simeq \pi a^2 n_i v_{T_i} M_T \left(1 + 2z \frac{\tau}{M_T^2}\right), \quad (2)$$

where $v_{T_i} = \sqrt{T_i/m_i}$ is the ion thermal velocity and $\tau = T_e/T_i$ is the electron to ion temperature ratio. From the condition $I_e - I_i = 0$, we obtain the following charges for a single particle: $|Q| = 3660 e$ (30 Pa), $4350 e$ (55 Pa), $4950 e$ (100 Pa). The charging time of a microparticle is given by inverse charging frequency $\Omega_{ch} = d(I_e - I_i)/dQ$ (calculated for the equilibrium charge), which yields

$$\Omega_{ch} = \frac{a\omega_{pi}^2 M_T}{4v_{T_i} \tau} \left(1 + 2(1+z) \frac{\tau}{M_T^2}\right), \quad (3)$$

where $\omega_{pi} = \sqrt{4\pi e^2 n_i/m_i}$ is the ion plasma frequency. The resulting charging time for the parameters taken from the PIC simulation is about three times shorter than the duration of a single video frame (0.33 ms). Practically, this implies that the explosion process evolves with the equilibrium charge corresponding to the local plasma environment, and the further particle dynamics is governed by their mutual interactions.

For the plasma conditions at the height where the compressed particle cloud initially levitates (see Table I), the electron contribution to the screening of the Coulomb field of microparticles should be insignificant. This is because the

local electron density is relatively low and, therefore, the corresponding electron Debye length ($\simeq 4$ mm) exceeds the characteristic size of the cloud (diameter $\simeq 2$ mm). Concerning the ion screening, we note that the ion flow is suprathermal ($M_T \gg 1$) and mobility-limited ($l_E \gg l_i$), so that we can directly employ the theory of Ref. 14 to calculate the interaction potential $\varphi(\mathbf{r})$ of microparticles

$$\varphi(r_\perp, r_\parallel) = \frac{2Q}{\pi l_i} Re \int_0^\infty dt \frac{e^{it(r_\parallel/l_i)}}{1 + (l_i/\lambda)^2 Y(t)} \times K_0\left(\frac{r_\perp}{l_i} \sqrt{\frac{t^2 + (l_i/\lambda)^2 X(t)}{1 + (l_i/\lambda)^2 Y(t)}}\right), \quad (4)$$

where r_\perp is the radial distance from the particle in the horizontal plane, perpendicular to the ion drift, r_\parallel is the distance along the drift, $K_0(x)$ is the zero-order modified Bessel function of the second kind, and $\lambda = \sqrt{eEl_i/4\pi n_i e^2}$ is the effective (field-dependent) screening length.¹⁴ The functions $X(t)$ and $Y(t)$ are

$$X(t) = 1 - \sqrt{1 + it},$$

$$Y(t) = \frac{2\sqrt{1 + it}}{it} \int_0^1 \frac{d\alpha}{[1 + it(1 - \alpha^2)]^2} - \frac{1}{it(1 + it)}. \quad (5)$$

In Eqs. (4) and (5), square roots should be taken with the positive real part.

In Fig. 3, the interaction potential calculated from Eq. (4) for the conditions of Table I is compared with the Coulomb potential (for the horizontal distances r_\perp within the characteristic cloud diameter). We see that for 30 Pa the interaction between dust particles is only slightly screened within the cloud. For higher pressures the screening becomes more pronounced. Therefore, the interaction between dust particle in our low-pressure experiments has (practically) the Coulomb character. Since the particle dynamics is dominated by the initial configuration, for the further analysis we focus

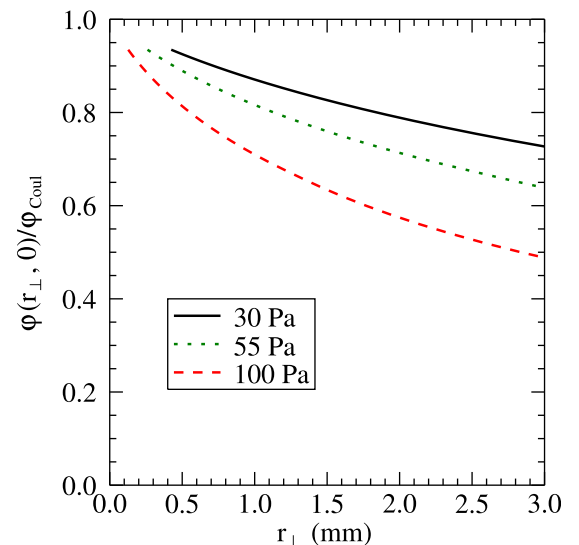


FIG. 3. The ratio of the pair interaction potential $\varphi(r_\perp, 0)$, Eq. (4), to the Coulomb potential $\varphi_{Coul} = Q/r_\perp$ versus the horizontal distance r_\perp , calculated for conditions of Table I.

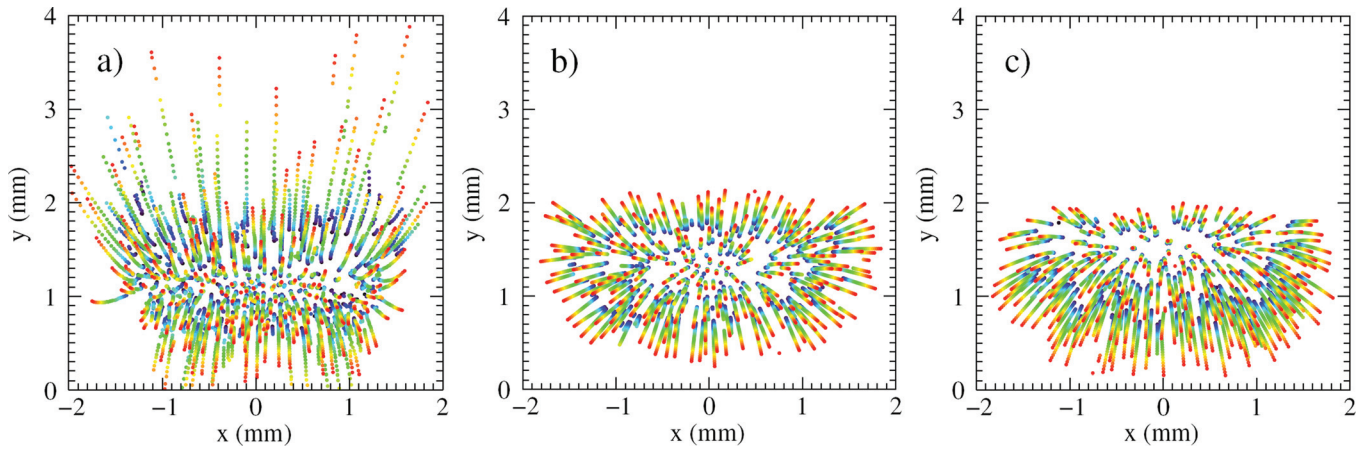


FIG. 4. 30 consecutive frames spanning 10 ms of the dust cloud expansion (a) in the experiment at pressure 30 Pa, (b) in the complementary MD simulation with the vertical sheath electric field from the PIC simulation, and (c) in the MD simulation without the sheath field. The simulation results are for the charge $|Q| = 900 e$. The particle trajectories are color-coded from blue to red. The lower electrode is at the height $y = 0$.

on the beginning of the cloud expansion (≈ 3.3 ms, which corresponds to 10 frames). We only analyze the horizontal component of the particle motion, which is solely due to the mutual repulsion between the particles (while the vertical motion is strongly influenced by the sheath electric field).

IV. PARTICLE CHARGE: COMPARISON WITH MD SIMULATION

The experimental data yield the particle positions and, therefore, velocities. By comparing these data with molecular dynamics (MD) simulations one can estimate the particle charges at the initial stage of the cloud expansion. For simplicity, we assume Coulomb interaction between the particles. This results in the following equation for the dynamics of individual particles:

$$m \frac{d^2 \mathbf{r}_i}{dt^2} + m \nu_{dn} \frac{d\mathbf{r}_i}{dt} = Q\mathbf{E} + Q^2 \sum_{j \neq i} \frac{\mathbf{r}_i - \mathbf{r}_j}{|\mathbf{r}_i - \mathbf{r}_j|^3} - m\mathbf{g}, \quad (6)$$

where m is the particle mass, \mathbf{r}_i is the position of the i th particle, \mathbf{E} is the vertical sheath field, \mathbf{g} is the gravity acceleration, and ν_{dn} is the neutral gas damping rate.¹⁵ The only unknown parameter in this equation is the charge Q (which is assumed to be the same for all particles).

The initial stage of the expansion observed in the experiment is presented in Fig. 4(a), showing the first 30 consecutive frames (10 ms) where the particle positions are obtained by using an automatic tracking algorithm. The results of complementary MD simulations with and without taking into account the sheath electric field (simulated by PIC method) are shown in Figs. 4(b) and 4(c), respectively. The time development is color-coded, from blue (beginning of expansion) to red. In the experiment, Fig. 4(a), about 2% of the particles moved substantially faster vertically than the major front of the “expanding” cloud. In fact, as we see in Fig. 5, the magnitude of the particle charge and, hence, of the electric force acting on particles in the experiment rapidly increases with y at the height of initial levitation (which occurred to be slightly above the equilibrium height deter-

mined by the condition $|QE| = mg$). Therefore, the particles at the upper edge of the cloud in Fig. 4(a) move much faster upwards than those in Fig. 4(b) (and, correspondingly, the particles at the lower edge move faster downwards). As particles move below the equilibrium height $y \approx 1$ mm (mainly driven by mutual repulsion), the electric force can no longer overcome gravity and particles drop to the electrode.¹⁷ We note that the calculation of charge in Fig. 5 is based on single-particle charging mechanism (see discussion below).

By comparing Figs. 4(b) and 4(c), we see that the horizontal motion is practically independent of the sheath electric field, as expected. Therefore, we use the results shown in Fig. 4(c) to deduce the particle charge. The horizontal particle velocities from tracing code were plotted versus the horizontal coordinate and fitted with a linear dependence, as shown in Fig. 6(a). The same procedure was applied to the simulation results, see Fig. 6(b). The resulting slopes of the linear fit for experimental velocities are shown in Fig. 7, for

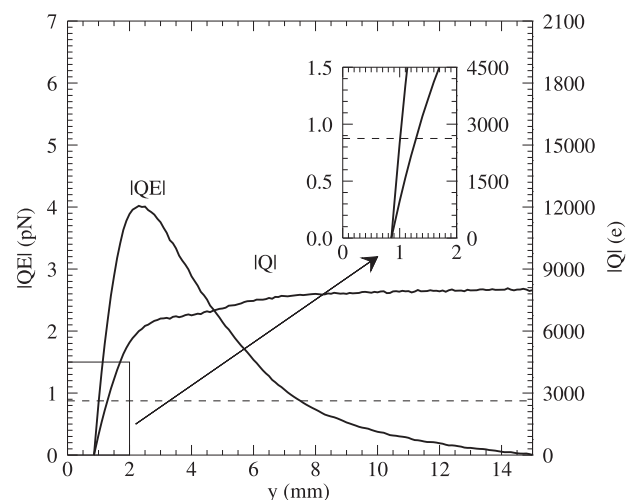


FIG. 5. The particle charge $|Q|$ and electric force $|QE|$ in the chamber (versus height y measured from the lower electrode), obtained from the PIC simulation at pressure 30 Pa. Only the curves for a negative particle charge are depicted. The horizontal dashed line shows the gravity force mg .

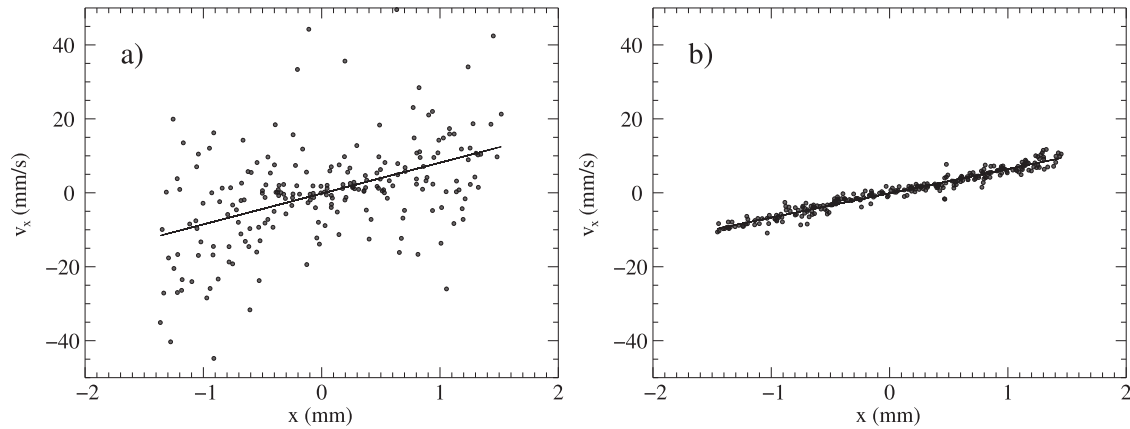


FIG. 6. The horizontal velocity distribution of the expanding dust cloud (versus the horizontal coordinate x) at pressure 30 Pa, measured 1 ms after the beginning of expansion in (a) experiment and (b) MD simulation. The linear fit shows the velocity slope corresponding to the particle charge $|Q| = 900 e$.

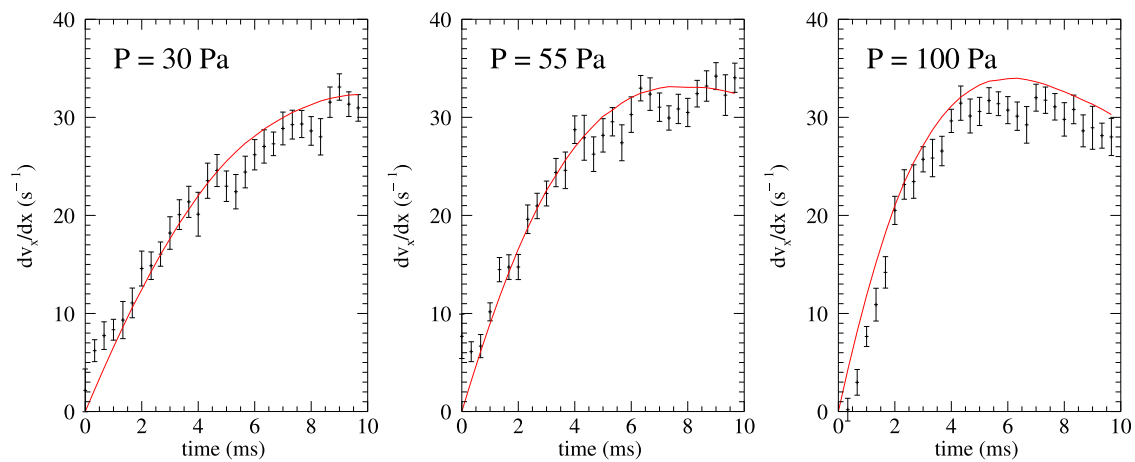


FIG. 7. The evolution of the horizontal velocity slope derived from the linear fit (see Fig. 6). Shown are the experimental data (symbols) and the results of complementary MD simulation (line) for 30 consecutive frames starting from the beginning of expansion, obtained for different pressures.

every frame, by symbols with error bars (the latter are due to small uncertainty in the determination of particle positions). The solid curve shows the dependence dv_x/dx versus t for MD simulations, which were performed for different values of Q with the step of $50 e$. By employing the least squares fit to the experimental data at each step, we were able to find the optimum value of charge. For the pressure of 30 Pa, the optimum charge is about $900 e$. Note, that the fit was only performed for the beginning of the experimental curve (first 10 frames corresponding to 3.3 ms), since at later times (i) the interparticle interaction becomes strongly screened due to expansion and (ii) particle charges vary significantly due to large vertical gradient (see Fig. 5).

The same fitting procedures were carried out for 55 Pa and 100 Pa (Fig. 7), yielding charges around $1100 e$ for both cases. This allowed us to estimate particle charges in the beginning of the cloud expansion for all these performed experiments. At high pressures, as we pointed out above, the basic assumption about the Coulomb interparticle interaction becomes less justified since the screening plays increasingly important role.

The fitting procedure of MD simulations yields the particle charges which are several times smaller than the theoretical values derived from Eqs. (1) and (2). One could associate this with

the fact that we study an extreme state of complex plasmas, with the (initial) particle density about $n_d \simeq 1.4 \times 10^6 \text{ cm}^{-3}$, which corresponds to $|Q|n_d/en_i \sim 10 - 100$. However, the electric field generated by the cloud turns out to be relatively weak: The field strength is estimated to be of the order of $0.1 E$, and the corresponding electrostatic potential at the cloud boundary does not exceed $\sim 0.3 T_e$. Therefore, the cloud does not strongly change the local distribution of ions and electrons and, hence, the charge of individual particles should not be noticeably affected by the presence of other particles.

We believe that the actual reason of the discrepancy between the theory and experiment is that the theoretical value of the charge was estimated by using a simple expression for the ion current, Eq. (2), corresponding to a displaced Maxwellian velocity distribution. In fact, the ion distribution in the sheath, which can be *crudely* approximated by a half-Maxwellian profile, is rather complicated (see, e.g., Ref. 16). Accurate calculation of the ion current in this case is a fairly delicate problem (which is certainly beyond the scope of this paper), but rough estimates indicate that it could be up to one order of magnitude larger than the current given by Eq. (2). Thus, the theoretical particle charges should be substantially smaller and, hence, closer to the values deduced from the fitting procedure of MD simulations.

V. CONCLUSION

We showed that dust particles in the discharge can be manipulated and stored in small plasma volumes by using specifically designed segmented rf-electrode. This setup allows us to create and study extreme states of complex plasmas deep in the sheath, in particular – to investigate the explosion and further expansion of the particle cloud into the sheath after the rf-driven segment (providing the confinement) is switched off. At the initial stage of expansion particles are located very close to each other, and their mutual interactions are practically unscreened. By comparing the experiments with PIC and MD simulations, we were able to explore some basic properties of complex plasmas in this highly non-equilibrium regime.

ACKNOWLEDGMENTS

This research was funded by Bundesministerium für Bildung und Forschung durch das Zentrum für Luft- und Raumfahrt e.V. (DLR) unter dem Förderkennzeichen 50 RT 0207. R.K. acknowledges the receipt of a Professor Harry Messel Research Fellowship supported by the Science Foundation for Physics within the University of Sydney.

¹V. E. Fortov, A. V. Ivlev, S. A. Khrapak, A. G. Khrapak, and G. Morfill, *Phys. Rep.* **421**, 1 (2005).

- ²P. K. Shukla and A. A. Mamun, *Introduction to Dusty Plasma Physics* (Institute of Physics, Bristol, 2002).
- ³V. Nosenko, A. V. Ivlev, and G. E. Morfill, *Phys. Rev. Lett.* **108**, 135005 (2012).
- ⁴M. Y. Pustylnik, N. Ohno, S. Takamura, and R. Smirnov, *Phys. Rev. E* **74**, 046402 (2006).
- ⁵B. M. Annaratone, T. Antonova, H. M. Thomas, and G. E. Morfill, *Phys. Rev. Lett.* **93**(18) 185001–1 (2004).
- ⁶V. V. Yaroshenko, T. Antonova, H. M. Thomas, and G. E. Morfill, *Phys. Plasmas* **16**, 103505 (2009).
- ⁷M. Mikikian, L. Couëdel, Y. Tessier, and L. Boufendi, *IEEE Trans. Plasma Sci.* **39**(11), 2748 (2011).
- ⁸B. M. Annaratone, M. Glier, T. Stuffer, H. Thomas, M. Raif, and G. E. Morfill, *New J. Phys.* **5**, 92 (2003).
- ⁹G. Thieme, R. Basner, R. Wiese, and H. Kersten, *Faraday Discuss.* **137**, 157 (2008).
- ¹⁰R. Basner, F. Sigenege, D. Loffhagen, G. Schubert, H. Fehske, and H. Kersten, *New J. Phys.* **11**, 013041 (2009).
- ¹¹A. Barkan and R. L. Merlino, *Phys. Plasmas* **2**, 3261 (1995).
- ¹²J. P. Verboncoeur, *Plasma Phys. Controlled Fusion* **47**, A231–A260 (2005).
- ¹³Y.-X. Liu, Q.-Z. Zhang, W. Jiang, L.-J. Hou, X.-Z. Jiang, W.-Q. Liu, and Y.-N. Wang, *Phys. Rev. Lett.* **107**, 055002 (2011).
- ¹⁴R. Kompaneets, U. Konopka, A. V. Ivlev *et al.*, *Phys. Plasmas* **14**, 052108 (2007).
- ¹⁵P. S. Epstein, *Phys. Rev.* **23**, 710 (1924).
- ¹⁶T. B. Röcker, S. K. Zhdanov, A. V. Ivlev, M. Lampe, G. Joyce, and G. E. Morfill, *Phys. Plasmas* **19**, 073708 (2012).
- ¹⁷Figure 5 shows that the second equilibrium position is around 7 mm above the electrode, which is slightly higher than the “normal” levitation height observed in the experiment. This discrepancy is because the ion drag force, important for the (pre)sheath region, is not taken into account in our estimation.

Frequency dependence of microparticle charge in a radio frequency discharge with Margenau electron velocity distribution

Cheng-Ran Du,^{a)} Sergey A. Khrapak, Tetyana Antonova, Bernd Steffes, Hubertus M. Thomas, and Gregor E. Morfill
Max Plank Institute for Extraterrestrial Physics, Garching 85741, Germany

(Received 29 October 2010; accepted 3 December 2010; published online 11 January 2011)

rf discharges are widely used in complex plasma experiments. In this paper, we theoretically investigate the dependence of the particle floating potential on the discharge frequency, assuming the model Margenau expression for the electron velocity distribution function. In doing so we use the orbital motion limited cross section to calculate the electron flux to the particle and collision enhanced collection approximation for the ion flux to the particle. The floating potential is then obtained from the flux balance condition. It is shown that for typical plasma conditions in laboratory rf discharges, normalized floating potential grows with increase of the discharge frequency in collisionless regime and decreases in weakly collisional regime. However, variations in the floating potential are usually small when plasma parameters do not depend on the rf frequency.

© 2011 American Institute of Physics. [doi:10.1063/1.3530439]

Charging of a particle immersed in a plasma is one of the most critical issues in the context of complex (dusty) plasmas.^{1–3} It determines the particle interaction with plasma electrons and ions (e.g., electron and ion drag forces),^{4–6} with electromagnetic fields,⁷ between particles themselves,⁸ etc. A particle surrounded by plasma collects ions and electrons from this environment, creating ion and electron fluxes toward its surface. The surface potential reaches a stable value when both fluxes are balanced.⁹ Due to high mobility of electrons, the particle generally acquires a negative surface potential, and hence negative charge. One of the most frequently used approaches to estimate the particle charge is the orbital motion limited (OML) approximation.¹⁰ This approach is based on the analysis of the collisionless ion and electron trajectories inside the sheath region around an individual particle. This analysis is used to calculate the corresponding collection cross sections, and then to estimate the surface floating potential, which yields the particle charge. Usually, Maxwellian velocity distributions are used to calculate the ion and electron fluxes. In other occasions, e.g., in space plasmas, generalized Lorentzian (kappa) distribution has been employed instead in order to fit the non-Maxwellian tails.¹¹

Capacitively coupled rf discharges at the industrial frequency of 13.56 MHz are widely used not only in the industrial applications such as material processing,¹² but also in laboratory plasma experiments.¹³ However, it is known that changing the excitation frequency will dramatically modify the discharge performance.¹⁴ In fact, increasing the excitation frequency brings various benefits in the context of industrial applications.^{15,16} For example, in a plasma enhanced chemical vapor deposition, high discharge frequency results in higher growth rate and better uniformity.¹⁷

Recently, particle charging process at different frequencies has received some attention. For example, Bacharis *et*

*al.*¹⁸ introduced a kinetic model to investigate the dependence of the particle charge on discharge frequency assuming that electron velocity distribution is perturbed. In the present paper, we present a simple calculation of the surface potential of a microparticle inside the bulk plasma of a capacitively coupled glow discharge operating at different frequencies, assuming that the electrons obey Margenau velocity distribution. Using a set of typical plasma parameters, the dependence of the floating potential as well as particle charge on discharge frequency is numerically estimated at four selected gas pressures (0.2, 5, 30, 120 Pa) covering the range from almost collisionless to weakly collisional regime.

The velocity distribution of the electrons considerably affects the magnitude of the electron flux directed to the particle surface.^{18–20} In the context of rf discharges, discharge frequency represents an important factor which influences the velocity distribution of electrons. We consider the range of sufficiently high frequencies, so that ions are not affected by modulations—only electrons react to the rf field. Using kinetic theory, Margenau²¹ derived an expression for the electron velocity distribution function in an ionized gas at arbitrary pressure and frequency of electric field modulation. For a non-negligible field, the distribution function can be written as

$$f_{e,\text{Mar}}(v) = A_1 \exp\left(-A_2 \frac{m_e^2 v^4 + 2m_e^2 \omega_{rf}^2 l_e^2 v^2}{4T_e^2}\right), \quad (1)$$

where v is electron velocity, m_e is electron mass, T_e is electron temperature, ω_{rf} is angular frequency of electric field modulation, $l_e = T_n / P \sigma_{en}$ (T_n is neutral temperature, P is gas pressure, and σ_{en} is the electron-neutral collision cross section) is the electron mean free path, and A_1 and A_2 are coefficients, which can be determined from $\int_0^\infty v^2 f_{e,\text{Mar}}(v) d^3v = 3v_{T_e}^2$ and $\int_0^\infty f_{e,\text{Mar}}(v) d^3v = 1$, where $v_{T_e} = \sqrt{T_e / m_e}$ is the electron thermal velocity. This electron velocity distribution function has been widely used in the investigation of ion-

^{a)}Electronic mail: chengran.du@mpe.mpg.de.

electron recombination of various gases in afterglow experiments.^{22,23} There are two extreme cases: As the frequency approaches zero, (rf discharge retards to dc discharge) the electron velocity distribution can be expressed as Druyvesteyn distribution $f_{e,\text{Dru}}=0.032vT_e^{-3}\exp[-0.243\times(mv^2/2T_e)^2]$.¹⁹ On the other hand, if the discharge frequency is so high to approach infinity, it becomes Maxwellian velocity distribution $f_{e,\text{Max}}=(2\pi vT_e)^{-3/2}\exp(-m_e v^2/2T_e)$. In both cases, discharge frequency is eliminated in the expressions. However, in general case, the electron distribution exhibits a dependence on the discharge frequency. The electron flux to the microparticle can be calculated using

$$J_e = n_e \int_0^\infty v \sigma_e(v) f_e(v) d^3v, \quad (2)$$

where n_e is electron density in the bulk plasma and $\sigma_e(v)$ is the velocity dependent (OML) cross section of electron collection

$$\sigma_e(v) = \begin{cases} \pi a^2 \left(1 - \frac{2e|\phi_s|}{m_e v^2}\right), & \frac{2e|\phi_s|}{m_e v^2} \leq 1, \\ 0, & \frac{2e|\phi_s|}{m_e v^2} > 1, \end{cases} \quad (3)$$

where ϕ_s is the particle surface potential, a is the particle radius, and e is the electron charge. For the sake of analytical convenience, we normalize J_e to the flux of electrons to an uncharged particle, so that $j_e = J_e/J_0$ where $J_0 = \sqrt{8\pi a^2 n_e v T_e}$.

Since the ions do not respond to the rf electric field, the conventional approach can be employed to calculate the ion flux toward charged particle. To account for ion-neutral collisions we use the so-called collision enhanced collection (CEC) model, which is a good approximation in the weakly collisional regime.^{24,25} With the same normalization, the ion flux is given by $j_i = (v_{Ti}/v_{Te})[1 + z\tau + 0.1(z\tau)^2(\lambda/l_i)]$, where $z = e|\phi_s|/T_e$ is the normalized particle surface potential, $\tau = T_e/T_i$ is the electron-to-ion temperature ratio, λ is the plasma screening length and $l_i = T_n/P\sigma_{in}$ (σ_{in} is the ion-neutral collision cross section) is the ion mean free path with respect to collisions with neutrals.^{24,25} The balance between electron and ion fluxes yields particle surface potential and charge.

In this paper, to figure out the effect of frequency modulation on particle charging, we consider an idealized situation where plasma parameters do not depend on the rf frequency. We therefore select a set of typical plasma parameters to calculate numerically the floating potential of a spherical particle at various gas pressures and frequencies:^{1,26} Electron and ion density $n_e \sim n_i \sim 2 \times 10^8 \text{ cm}^{-3}$, electron temperature $T_e \sim 3 \text{ eV}$, ion and neutral temperature $T_i \sim T_n \sim 0.025 \text{ eV}$, linearized Debye radius $\lambda \sim 40 \text{ }\mu\text{m}$, electron-neutral collision cross section $\sigma_{en} \sim 3 \times 10^{-16} \text{ cm}^2$, and ion-neutral collision cross section $\sigma_{in} \sim 2 \times 10^{-14} \text{ cm}^2$.

In Fig. 1, we plot the electron and ion fluxes as functions of the normalized floating potential z for four different rf discharge frequencies and two extreme cases of Maxwellian and Druyvesteyn distributions. Here four different gas pressures are selected, covering the range from 0.2 to 120 Pa

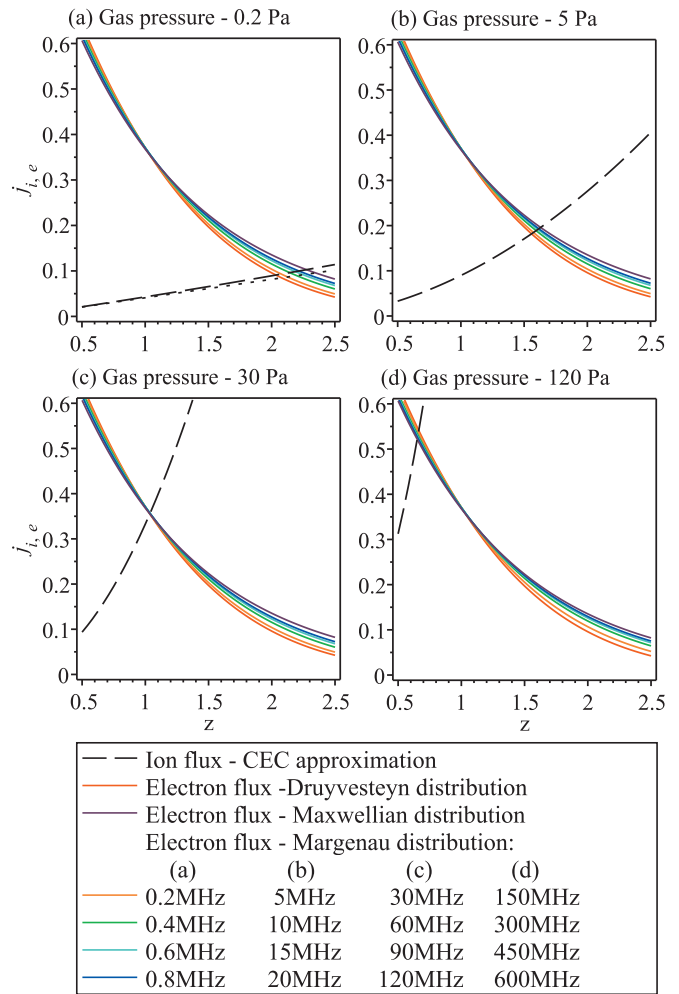


FIG. 1. (Color) Dependence of the normalized ion and electron fluxes collected by a spherical particle in a plasma on the normalized particle surface potential $z = e|\phi_s|/T_e$ at various neutral gas pressures. Dotted line in (a) corresponds to the normalized ion flux derived from the OML theory.

typical for laboratory complex plasma experiments. Ion fluxes are derived from CEC theory at all pressure values. It is worthwhile to mention that at a gas pressure of 0.2 Pa, ion flux derived from the CEC theory almost coincides with the ion flux derived from the collisionless OML theory. At higher pressures, difference between the CEC and OML fluxes is more pronounced. Notice also that the discharge frequencies are chosen differently at various gas pressures since the range of frequency, which has significant influence on the electron distribution, varies with electron-neutral collision frequency. Obviously, only if the electron-neutral collision frequency is comparable with the discharge frequency, the electron velocity distribution will be significantly modified by changing the discharge frequency. The horizontal coordinates of the intersection of ion and electron fluxes give the normalized surface potential z . As we see in Fig. 1, the Druyvesteyn distribution predicts higher electron flux than Maxwellian distribution in the regime of low surface potential ($z \lesssim 1$). However, as to the regime of high surface potential ($z \gtrsim 1$), the Druyvesteyn distribution results in a lower flux because the high-energy tail of the electron distribution function is suppressed. Therefore, the electron flux increases

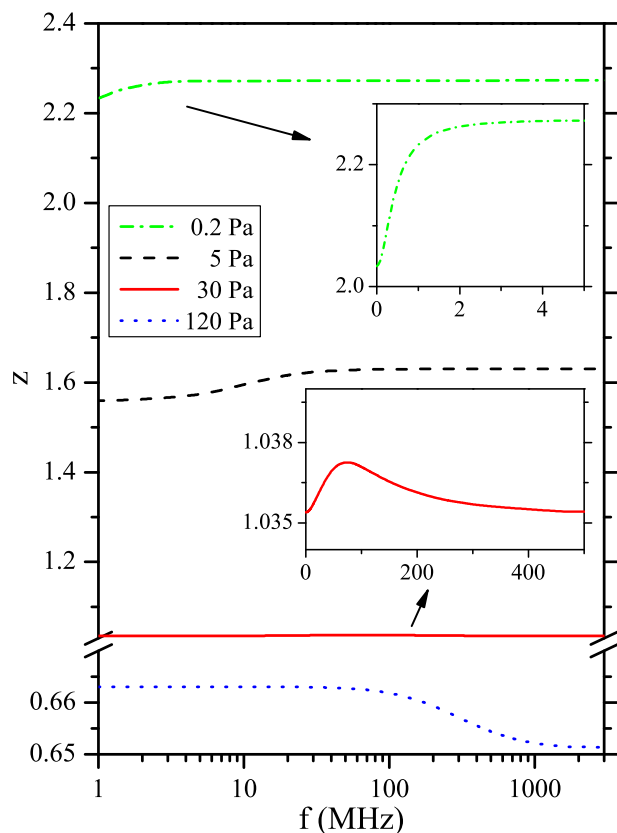


FIG. 2. (Color online) The dimensionless surface potential $z = e|\phi_s|/T_e$ as a function of rf frequency at various gas pressures. The inset figures amplify the dimensionless particle charge in the frequency range from 0 to 5 MHz at a gas pressure of 0.2 Pa and from 0 to 500 MHz at a gas pressure of 30 Pa, respectively.

with discharge frequency in the regime of high surface potential and decreases in the opposite case. It is almost independent of the discharge frequency in the region around $z \sim 1$, where the curves corresponding to different frequencies intersect. On the other hand, the ion flux is insensitive to the rf frequency, but increases considerably with increasing gas pressure (ion collisionality).

We plot the dimensionless floating potential as a function of discharge frequency in Fig. 2. The tendency of surface potential against the rf frequency is different for various gas pressures. For relatively low pressures (e.g., 0.2, 5 Pa), since the particle floating potential is higher, the electron flux increases as the applied rf frequency increases, which leads to the increase of the surface potential. The magnitude of the total increase for 5 Pa is considerably smaller as compared to the case of 0.2 Pa. At a pressure of 30 Pa, the surface potential basically does not depend on the discharge frequency. However, if we zoom in the plot in the range from 0 to 500 MHz, as shown in the inset of Fig. 2, one can observe a peak of the surface potential at the frequency of c.a. 80 MHz. At this intermediate pressure, intersection region of electron flux curves at different frequencies has a complicated structure, resulting in the emergence of the peak. Nevertheless, the variance of this fine peak structure is so small (0.2%) that it can be absolutely neglected in usual situations. As to the highest pressure studied (120 Pa), particle charge is lower as compared to the low pressure regime. Under such

condition, electron flux decreases with frequency and so does the surface potential. The total drop is about 1%, which can also be considered as insignificant. For sufficiently small particles, particle charge and surface potential are related via $Ze = a|\phi_s|$. With the knowledge of the surface floating potential, particle charge can be easily calculated.

In summary, using Margenau electron velocity distribution, we calculated the electron flux toward the microparticle surface in a wide range of discharge frequency. It is shown that modulation of the discharge frequency leads to modulations in the particle surface potential. The surface potential increases with an increase of discharge frequency at low gas pressures, while drops at high pressures. However, the observed variations are so small that in practical situations the direct effect of the rf frequency on the particle charge can be easily masked by indirect effects associated with plasma parameters (density and electron temperature) modification in response to changing the rf frequency. An important conclusion is therefore that it is necessary to determine the dependence of plasma parameters on discharge frequency in order to get a complete picture regarding frequency dependence of the particle charge. We leave this for future work.

¹V. E. Fortov, A. V. Ivlev, S. A. Khrapak, A. G. Khrapak, and G. Morfill, *Phys. Rep.* **421**, 1 (2005).

²G. E. Morfill and A. V. Ivlev, *Rev. Mod. Phys.* **81**, 1353 (2009).

³S. A. Khrapak and G. E. Morfill, *Contrib. Plasma Phys.* **49**, 148 (2009).

⁴S. A. Khrapak, A. V. Ivlev, S. K. Zhdanov, and G. E. Morfill, *Phys. Plasmas* **12**, 042308 (2005).

⁵S. A. Khrapak, A. V. Ivlev, G. E. Morfill, and H. M. Thomas, *Phys. Rev. E* **66**, 046414 (2002).

⁶S. A. Khrapak and G. E. Morfill, *Phys. Rev. E* **69**, 066411 (2004).

⁷J. E. Daugherty, R. K. Porteus, and D. B. Graves, *J. Appl. Phys.* **73**, 1617 (1993).

⁸G. E. Morfill, V. N. Tsytovich, and H. M. Thomas, *Plasma Phys. Rep.* **29**, 1 (2003).

⁹T. Nitter, *Plasma Sources Sci. Technol.* **5**, 93 (1996).

¹⁰J. E. Allen, *Phys. Scr.* **45**, 497 (1992).

¹¹M. Rosenberg and D. A. Mendis, *J. Geophys. Res.* **97**, 14773, doi:10.1029/92JE01313 (1992).

¹²M. A. Lieberman and A. J. Lichtenberg, *Principles of Plasma Discharges and Materials Processing* (Wiley, New York, 1994).

¹³H. M. Thomas, G. E. Morfill, V. E. Fortov, A. V. Ivlev, V. I. Molotkov, A. M. Lipaev, T. Hagl, H. Rothermel, S. A. Khrapak, R. K. Sütterlin, M. Rubin-Zuzic, O. F. Petrov, V. I. Tokarev, and S. K. Krikalev, *New J. Phys.* **10**, 033036 (2008).

¹⁴E. Abdel-Fattah and H. Sugai, *Jpn. J. Appl. Phys., Part 1* **42**, 6569 (2003).

¹⁵J. Rüdiger, H. Brechtel, A. Kottwitz, and U. Stephan, *Thin Solid Films* **427**, 16 (2003).

¹⁶A. Koshiishi, M. Tomoyasu, Y. Tahara, and M. Kojima, Proceedings of the 19th Symposium on Dry Process, Tokyo, 1998, p. 229.

¹⁷A. A. Howling, J. L. Dorier, C. Hollenstein, U. Kroll, and F. Finger, *J. Vac. Sci. Technol. A* **10**, 1080 (1992).

¹⁸M. Bacharis, M. Coppins, and J. E. Allen, *Plasma Sources Sci. Technol.* **19**, 025002 (2010).

¹⁹S. A. Khrapak, *Phys. Plasmas* **17**, 104502 (2010).

²⁰M. Li, S. K. Dew, and M. J. Brett, *J. Phys. D: Appl. Phys.* **32**, 2056 (1999).

²¹H. Margenau, *Phys. Rev.* **69**, 508 (1946).

²²R. Johnsen, *J. Chem. Phys.* **98**, 5390 (1993).

²³M. P. Skrzypkowski and R. Johnsen, *Chem. Phys. Lett.* **274**, 473 (1997).

²⁴S. A. Khrapak and G. E. Morfill, *Phys. Plasmas* **15**, 114503 (2008).

²⁵S. A. Khrapak, S. V. Ratynskaia, A. V. Zobnin, A. D. Usachev, V. V. Yaroshenko, M. H. Thoma, M. Kretschmer, H. Höfner, G. E. Morfill, O. F. Petrov, and V. E. Fortov, *Phys. Rev. E* **72**, 016406 (2005).

²⁶B. M. Annaratone, A. G. Khrapak, A. V. Ivlev, G. Söllner, P. Bryant, R. Sütterlin, U. Konopka, K. Yoshino, M. Zuzic, H. M. Thomas, and G. E. Morfill, *Phys. Rev. E* **63**, 036406 (2001).

Agglomeration of microparticles in complex plasmas

Cheng-Ran Du,^{a)} Hubertus M. Thomas, Alexei V. Ivlev,
Uwe Konopka, and Gregor E. Morfill

Max Planck Institute for Extraterrestrial Physics, Garching 85741, Germany

(Received 15 July 2010; accepted 10 September 2010; published online 24 November 2010)

Agglomeration of highly charged microparticles was observed and studied in complex plasma experiments carried out in a capacitively coupled rf discharge. The agglomeration was caused by strong waves triggered in a particle cloud by decreasing neutral gas pressure. Using a high-speed camera during this unstable regime, it was possible to resolve the motion of individual microparticles and to show that the relative velocities of some particles were sufficiently high to overcome the mutual Coulomb repulsion and hence to result in agglomeration. After stabilizing the cloud again through the increase of the pressure, we were able to observe the aggregates directly with a long-distance microscope. We show that the agglomeration rate deduced from our experiments is in good agreement with theoretical estimates. In addition, we briefly discuss the mechanisms that can provide binding of highly charged microparticles in a plasma.

© 2010 American Institute of Physics. [doi:10.1063/1.3495979]

I. INTRODUCTION

Dust agglomeration, also known as dust aggregation or dust coagulation, is a process of sticking dust particles together after their collision.^{1,2} This process occurs in very different environments and plays an important role in colloid chemistry,³ astrophysics,⁴ atmospheric physics,⁵ fusion physics,⁶ as well as plasma physics.⁷ Agglomeration of nanoparticles in low-temperature plasmas, the major mechanism operating during the so-called “rapid growth” (RG) phase,⁹ has been observed in numerous experiments.^{10,11} At the RG stage, most of the nanoparticles are neutral, some carry several electron charges, even fewer are charged positively,^{11,12} and therefore the charge discreteness plays a very important role. The agglomeration criteria for such particles were derived theoretically based on either the polarization-induced ion flux asymmetry model¹³ or the shadow attraction due to neutral/plasma particle bombardment.¹⁴ The agglomeration of nanoparticles in a plasma has been reported for sizes up to several hundreds of nanometer.^{15,16} As the size of particles immersed in a plasma increases, their charges become more and more negative (the charge is linearly proportional to the particle size, for a 1 μm particle, it ranges from several hundreds to several thousands of electrons, depending on the discharge conditions^{8,17,18}). Therefore, agglomeration of microparticles in a plasma has been believed, so far, to be practically impossible due to strong Coulomb repulsion. This process was primarily studied (both experimentally and theoretically) in a neutral environment,^{19,20} showing that positive and negative charges carried by individual particles (in the overall neutral ensemble) can enormously accelerate the agglomeration.

In this article, we report on a series of experiments where highly-nonlinear dust-acoustic (density) waves trigger agglomeration of microparticles. We show that the agglomeration can occur under typical discharge conditions, for par-

ticles of different sizes and materials, and the aggregates formed in a plasma can be observed *in situ* using a long-distance microscope.

II. EXPERIMENTS AND OBSERVATIONS

The experiments were performed on the ground in the PK-3 Plus chamber,²¹ which was originally designed for microgravity experiments onboard the International Space Station (ISS). The chamber (which consists of two parallel electrodes driven in push-pull mode at a frequency of 13.56 MHz) was placed horizontally and single microparticles (no agglomerates) were injected into the discharge from a special dispenser. A vertical laser sheet (perpendicular to the electrodes) with a thickness of about 100 μm was used to illuminate the particles in the plasma, the scattered light was recorded at 90° by a high-speed charge-coupled-device (CCD) camera. A detailed description of the PK-3 Plus setup can be found in Ref. 21.

Microparticles were first injected into argon plasma (typically maintained at a rf peak-to-peak voltage of ≈ 25 V and gas pressure of ≈ 50 Pa) to form a stable cloud above the bottom electrode. Then, in order to accelerate particles, dust-acoustic (density) waves were triggered in the cloud by decreasing gas pressure well below the instability threshold¹⁸ (down to 10–20 Pa). This unstable regime was maintained for several minutes, and then the gas pressure was restored to the initial (stable) level. Such experiments were performed with particles of different sizes and materials.

We compared profiles of the dust clouds before and after the wave excitation, as illustrated in Fig. 1. After the excitation, we observed aggregates levitated at the bottom of the cloud (they can be identified as brighter spots having larger distances to their neighbors). For SiO₂ particles of 1.5 μm in diameter (first row), multiple layers of aggregates (apparently of different sizes) were seen after the unstable regime. The aggregates were separated from single particles by a narrow but well-seen gap, while before the wave excitation

^{a)}Electronic mail: chengran.du@mpe.mpg.de.

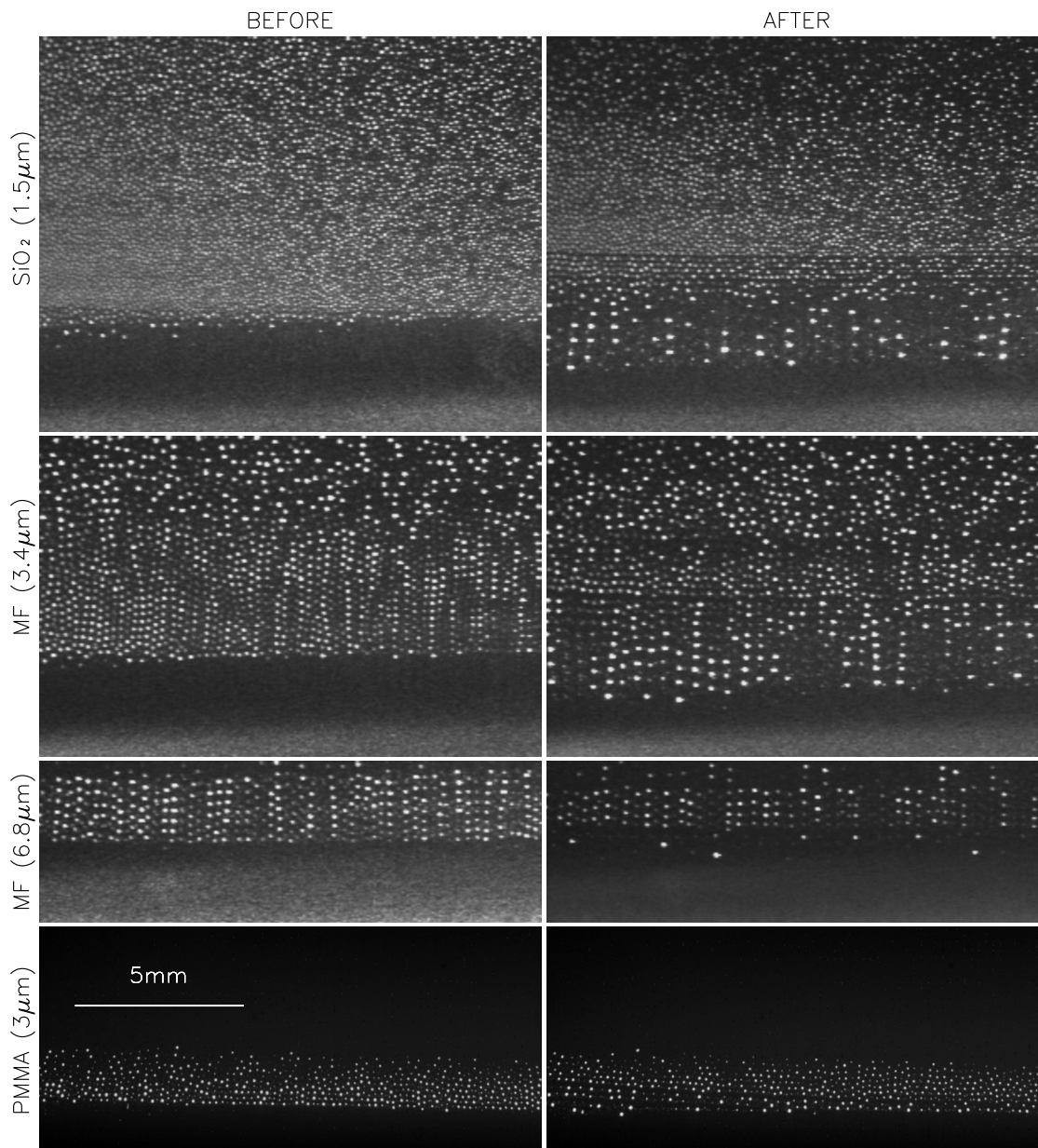


FIG. 1. Particle cloud before the dust density waves were triggered (first column) and after the waves were stopped (second column). Shown are the results of the experiments with different particles: the first row represents SiO_2 particles of $1.5 \mu\text{m}$ in diameter, the second row—MF particles of $3.4 \mu\text{m}$ in diameter, the third row—MF particles of $6.8 \mu\text{m}$ in diameter, and the fourth row—PMMA particles of $3 \mu\text{m}$ in diameter.

there were only a few bigger particles near the lower edge. The similar situation was also observed for melamine-formaldehyde (MF) particles of $3.4 \mu\text{m}$ and $6.8 \mu\text{m}$ in diameter (second and third row, respectively) as well as for polymethyl-methacrylate (PMMA) particles of $3 \mu\text{m}$ in diameter (fourth row).

In order to take a closer look at the structure of the aggregates, we used a long-distance microscope (with a diffusive light source from the opposite side of the chamber), which allowed us to perform *in situ* observations. Due to the limited resolution of the microscope, we were only able to analyze the experiments with sufficiently large particles. The

results are presented in Fig. 2. In the experiments with MF, PMMA, and “magnetic polystyrene”²² (MPS) particles of about $3 \mu\text{m}$ in diameter (first, second, and third rows, respectively), the aggregates were usually composed of several particles and had rather irregular (often elongated) structure. For larger MF particles of $6.8 \mu\text{m}$ in diameter (fourth row), the aggregates were typically formed of two to three particles. It is noteworthy that for silver-coated polystyrene (PS) particles of $5 \mu\text{m}$ in diameter (fifth row), the agglomeration was also possible and in fact very effective, resulting in the formation of relatively large elongated aggregates. This strongly suggests that the agglomeration of microparticles in

a plasma is a quite generic phenomenon occurring both for dielectric and conductive particles.

III. ANALYSIS

The agglomeration in a plasma can only be achieved if heavily charged particles acquire the kinetic energy, which is sufficiently high to overcome the interparticle repulsion. In our experiment, the particles were accelerated by the dust-acoustic waves (which were presumably triggered by the ion streaming instability⁸). In order to track the individual particles inside the wave, we performed a series of experiments with MF particles of 2.5 μm in diameter and recorded their motion for 2 s. We used a high-speed camera at 2000 frames/s with full exposure, recording the field of view of 3 mm \times 3 mm (at a spatial resolution of 210 pixels/mm). The waves propagated mostly vertically, with an average wave period of about 60 ms (at a gas pressure of 20 Pa). The waves were highly nonlinear, with a minor fraction of particles moving in one direction at rather high velocities, while most of them were moving slowly in the opposite direction. To visualize the particle trajectories, five consecutive video frames were color-coded and overlapped, as shown in Fig. 3(a).

In order to analyze the agglomeration process in detail, we first have to evaluate the parameters that determine the interparticle interaction. Obviously, the most critical parameter for such analysis is the charge of microparticles; if it is too high the coagulation is inhibited. A simple estimate of the charge from the orbit-motion-limited theory is just not possible for our conditions since the plasma parameters in dense particle clouds are poorly known. As an alternative, we were able to derive the charge from rarely occurring *scattering* collisions of two particles. We supposed that the observed collision events are representative, in the sense that charges of the colliding particles are close to the mean particle charge in the whole cloud. An example of the collision event is shown in Figs. 3(b)–3(f). For the analysis, we assumed the Debye–Hückel interaction potential, which depends on two unknown parameters: the charge Q and the screening length λ . These parameters were derived by simulating the pair collisions and fitting the resulting trajectories to the observed ones. We took into account neutral gas friction²³ and used the particle velocities and coordinates measured before the collision as the initial conditions. Since the velocities and coordinates were naturally measured with some errors, the fittings of Q and λ were performed by varying the initial conditions within the estimated error bars. The best fit was then defined by maximizing the correlation between the simulated and measured trajectories, which is illustrated in Fig. 4. We found that the fit is practically insensitive to the value of λ apparently because the relative velocities of colliding particles were so high that the scattering mostly occurred at distances smaller than the screening length. This observation significantly simplified the subsequent analysis and allowed us to directly employ the Rutherford's scattering theory.^{18,24} Given the fact that the typical collision event is much shorter than the gas damping timescale, the charge can be obtained from the formula $Q = -\sqrt{2Eb \tan(\theta/2)}$, where

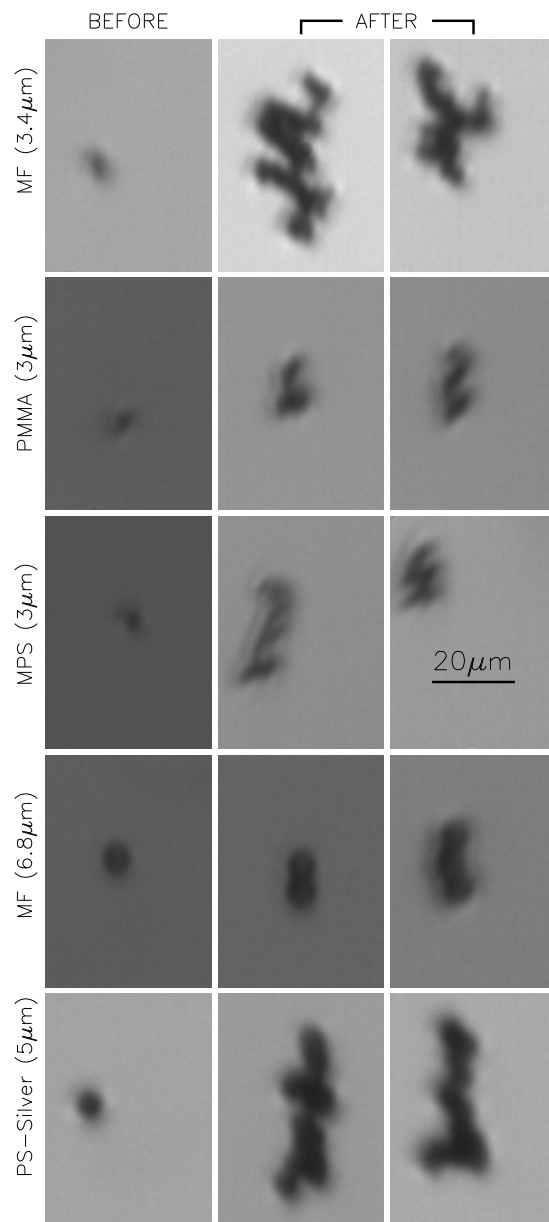


FIG. 2. Single microparticles before the waves were triggered (first column) and examples of aggregates after the waves were stopped (second and third column), all observed with a long-distance microscope. Experiments were performed with different particles, the first row—MF particles of 3.4 μm in diameter, the second row—PMMA particles of 3 μm in diameter, the third row—MPS particles of 3 μm in diameter, the fourth row—MF particles of 6.8 μm in diameter, and the fifth row—silver-coated PS particles of 5 μm in diameter.

$E = \mu v^2/2$ is the center-of-mass energy of the relative particle motion ($\mu = m/2$ is the reduced mass, m is the mass of a single particle, and v is the relative velocity), θ is the scattering angle, and b is the impact parameter for colliding particles. This yields the charge $Q = -(1650 \pm 170)e$, where the uncertainty is given by the standard deviation averaged over ten collision events. However, one should keep in mind that the actual uncertainty is somewhat larger because the collision plane (in the center-of-mass reference frame) is never perfectly parallel to the illuminating laser sheet (which has a finite thickness), as one can see from Fig. 4.

Two colliding particles can touch each other only if their

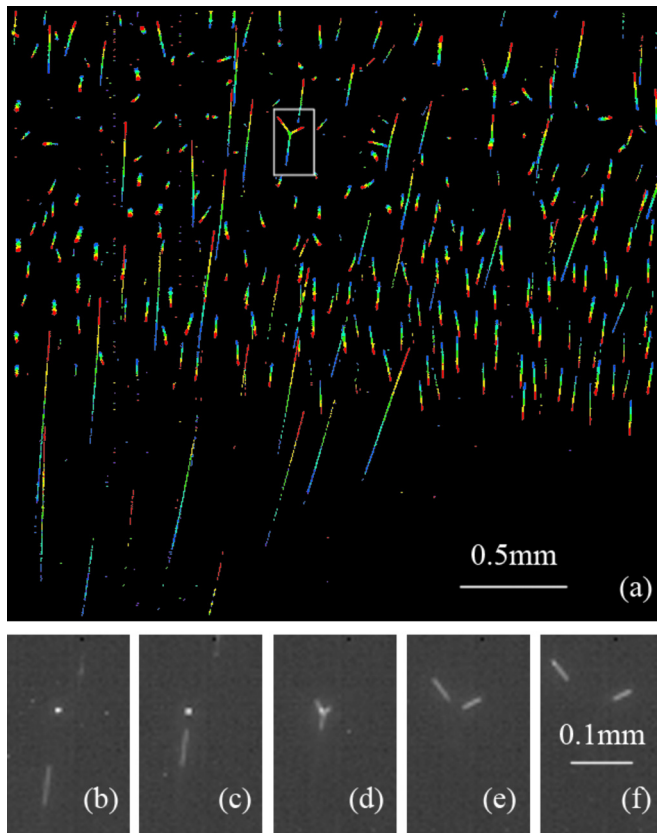


FIG. 3. (Color online) Trajectories of individual microparticles in the wave. (a) The trajectories are depicted by superimposing five consecutive video frames (color-coded from dark blue to red online). [(b)–(f)] Example of a two-particle scattering collision [magnified rectangular box from (a)], the scattering is shown as a sequence of five consecutive frames. The results are for MF particles of $2.5 \mu\text{m}$ in diameter.

relative velocity exceeds a critical (threshold) value determined by the Coulomb repulsion. Using the same assumptions as above, we readily obtain the critical velocity,

$$v_{\text{cr}} = \frac{|Q|}{\sqrt{\frac{1}{2}ma}}, \quad (1)$$

which has the following scaling on the particle size: $v_{\text{cr}} \propto a^{-1}$ (here we also assume $Q \propto a$). For the experiment shown in Fig. 3, we get $v_{\text{cr}} \approx 270 \text{ mm/s}$. In order to evaluate the probability for particles in the cloud to reach the critical velocity, we tracked the individual particles manually and estimated their velocities from the lengths of the trajectories at each video frame. From this analysis, we deduced the *relative velocity* distribution (normalized to unity), $f_{\text{rel}}(v)$, which is shown in Fig. 5 for different phases ϕ of the wave. This plot clearly demonstrates that for certain ϕ there is a small fraction of particles with the relative velocities exceeding v_{cr} .

Using these results, we estimated the agglomeration rate for pair collisions (per unit volume, assuming that the sticking probability upon collision is unity),

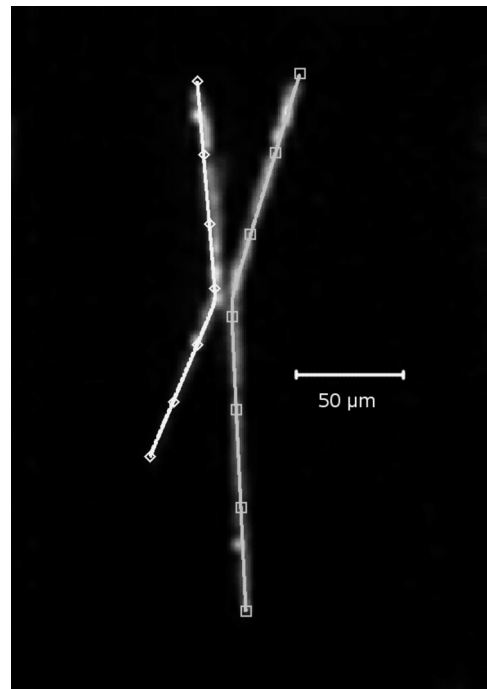


FIG. 4. Comparison of a two-particle scattering collision with the simulations. The simulated trajectories (marked by diamonds and squares) are overlapped with the observed particle trajectories (from the experiment shown in Fig. 3). One of the trajectories (diamonds) becomes noticeably dimmer at one end, suggesting that the scattering plane (in the center-of-mass reference frame) is not parallel to the illuminating laser sheet.

$$R = \frac{1}{T} \int_0^T dt n^2 \int_0^\infty dv \sigma v f_{\text{rel}}, \quad (2)$$

where $n(t)$ is the (time-dependent) particle number density in the cloud, T is the wave period, and the collision cross section σ ,

$$\sigma(Q, v) = \begin{cases} 0, & v \leq v_{\text{cr}} \\ 4\pi a^2 (1 - v_{\text{cr}}^2/v^2), & v > v_{\text{cr}} \end{cases}$$

is determined by the critical velocity given by Eq. (1). The calculations yield $R \approx 0.8 \text{ mm}^{-3} \text{ s}^{-1}$ for the experiment illustrated in Figs. 3–5. In order to compare these estimates with the experiment, we selected a part of the visible cloud (assuming the horizontal homogeneity), which represents a slice with thickness of $\approx 0.1 \text{ mm}$ (about the thickness of the illuminating laser sheet), width of 3 mm , and height of 5.8 mm (full height of the cloud). The number of (double) aggregates predicted by Eq. (2) to appear in this volume after 5 min of the unstable regime is ≈ 450 , which is five to six times larger than the number of aggregates (82) we actually observed. Taking into account that the sticking probability of the colliding particles can be substantially smaller than unity, and also that the aggregates in the considered experiment consisted (on average) of more than two particles, we conclude that the theory provides reasonable agreement with the experiment.

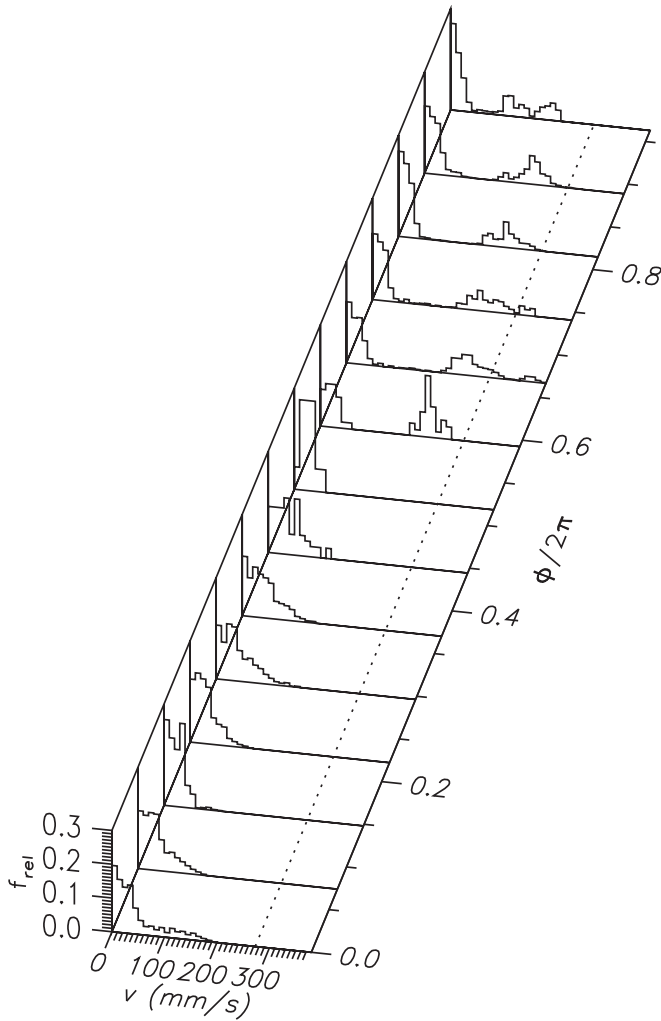


FIG. 5. Relative velocity distribution of microparticles, $f_{rel}(v)$, for different phases ϕ of the wave period (for the experiment shown in Fig. 3). The distribution is normalized to unity, the dash line corresponds to the critical velocity $v_{cr}(=270 \text{ mm/s})$.

IV. DISCUSSION AND CONCLUSION

Let us discuss the mechanisms that can effectively bind particles in a plasma. If we assume a homogeneous charge distribution over the spherical particle surfaces, the repulsive Coulomb force F_C between them is equivalent to that between the two point charges Q located at the centers of the spheres. Therefore, the force at the contact,

$$F_C = \frac{Q^2}{4a^2}, \quad (3)$$

does not depend on a . On the other hand, the charge at one particle induces a dipole moment at another particle. This results in the attractive force that depends on the permittivity of the particle material and also scales as $\propto(Q/a)^2$, thus tending to balance F_C .

However, there are (at least) two other very efficient attraction mechanisms that can overcome the repulsive force (3). One of them is due to the van der Waals interactions

between individual molecules of microparticles. For two identical spherical particles, Hamaker²⁵ gave the following expression of the attractive force:

$$F_{vdW} = \frac{A_H a}{12\delta^2}, \quad (4)$$

where A_H is the material-dependent Hamaker constant and $\delta(\ll a)$ is the effective distance between surfaces of two particles at the contact.^{2,25} (If the polarization of spheres is neglected, then $A_H = \pi^2 \rho^2 \alpha$, where ρ is the number density of molecules and α is the corresponding London–van der Waals constant.) By comparing Eqs. (3) and (4), we see that the van der Waals attraction is stronger than the Coulomb repulsion when $A_H > Q^2 \delta^2 / a^3 (\propto a^{-1})$. Let us consider an aggregate composed of two SiO_2 particles ($A_H = 6.5 \times 10^{-20} \text{ J}$) with a diameter of $1.5 \mu\text{m}$ (the smallest particles used in the experiments, see the first row in Fig. 1). Assuming that the particles carry the charge $Q = -1000e$ each and are separated by $\delta \approx 3 \text{ \AA}$ at the contact, we obtain that F_{vdW} is two orders of magnitude stronger than F_C . Note that for metal particles (such as Au, Ag, and Cu), A_H is typically in the range of $(25\text{--}40) \times 10^{-20} \text{ J}$,²⁶ and therefore the binding force for them should be even stronger. One should also point out that the particle coating (see, e.g., the fifth row in Fig. 2) may affect van der Waals attraction, provided the coating thickness is comparable to or exceeds δ and the α constant of the coating material is different from that of the particle material.

The second mechanism of attraction can be associated with the discreteness of the charge distribution over the particle surface (here, we do not discuss the physics of the electron states at dielectric surfaces). The “mean distance” between the electrons at the surface, which can be estimated as $\Delta_e \sim a\sqrt{4\pi e/|Q|} \propto a^{1/2}$, is typically of a few dozens of nanometers. Therefore, when particles get in contact, their interaction should strongly depend on whether there are individual electrons in a close proximity of the contact spot. For instance, if there is one electron *at each* particle surface near the contact spot, this will exert an additional repulsive force which can be as large as $\sim e^2/\delta^2$. However, if an electron is only attached to *one* of the particles, this results in the additional *attraction* between them due to the local polarization of the particle material. Simple calculations (representing each particle as an infinite half-space filled with a material of high complex permittivity) yield the following attractive force due to the “charge discreteness:”

$$F_{disc} = \frac{e^2}{4\delta^2}. \quad (5)$$

By comparing Eq. (5) with Eq. (3), we obtain that the charge discreteness force should overcome the Coulomb repulsion when $(a/\delta)^2 > (Q/e)^2$, and this condition does not depend on a . For SiO_2 particles considered above (to illustrate the van der Waals attraction), F_{disc} is an order of magnitude stronger than F_C and hence can also contribute to the binding. Note that F_{disc} is really of short range and can only be important when particles get very close to each other ($\delta \lesssim \Delta_e$); otherwise, the interaction is described by usual “mean-field” formulas. Also, F_{disc} must be strongly depen-

dent on the particle (surface) conductivity and presumably be much larger for dielectric particles than for conductive (or coated) ones.

One should make a common remark concerning both binding mechanisms discussed above. In our calculations, we used rather crude assumption that the charges of individual particles in a plasma and charges of particles bound in a cluster are the same. This assumption is quite justified as the “first approach” since the estimated binding forces turn out to be much stronger than the Coulomb repulsion. However, for a more careful analysis of the problem one should take into account the mutual influence of the neighboring particles on their charges (see, e.g., Refs. 27 and 28). In fact, the binding force should strongly depend not only on the magnitude of the particle charge but also on the charge distribution over the particle surface. This very complex issue undoubtedly requires further careful analysis.

To summarize, by triggering dust-acoustic waves in a cloud of microparticles suspended in the presheath region of a low pressure rf discharge (which is referred to as the unstable regime), we were able to accelerate the particles to velocities that were sufficiently high to overcome their mutual Coulomb repulsion. This resulted in the agglomeration—the formation of clusters consisting of two, three, or more particles—yet this effect was observed for particles of different sizes and materials. By tracking individual particles and resolving their scattering collisions with a high-speed camera, we calculated the mean particle charge and reconstructed the relative velocity distribution function. This allowed us to estimate the coagulation rate during the unstable regime and compare it with the experimental observations. Additionally, by using a long-distance microscope we were able to observe the aggregates *in situ*, levitated in a plasma after the wave excitation.

The results presented in this paper unambiguously demonstrate that microparticles, even exposed in a plasma environment, can form stable clusters due to strong short-range binding forces. We believe that these results can be of great importance to various fields ranging from plasma processing (where this effect can be utilized, e.g., to remove dust contamination) to astrophysics (where the effect can have a strong impact on the coagulation of cosmic dust).

ACKNOWLEDGMENTS

The authors would like to acknowledge the valuable discussions with M. Schwabe, S. Shimizu, and T. Shimizu as well as the technical support from T. Hagl. This research was

funded by the “Die Raumfahrt-Agentur des Deutschen Zentrums für Luft und Raumfahrt e. V. mit Mitteln des Bundesministeriums für Wirtschaft und Technologie aufgrund eines Beschlusses des Deutschen Bundestages unter dem Förderkennzeichen 50 WP 0203.”

- ¹A. Chokshi, A. Tielens, and D. Hollenbach, *Astrophys. J.* **407**, 806 (1993).
- ²J. Blum, *Adv. Phys.* **55**, 881 (2006).
- ³M. Lin, H. Lindsay, D. Weitz, R. Ball, R. Klein, and P. Meakin, *Nature (London)* **339**, 360 (1989).
- ⁴J. A. Wood, *Astrophys. J.* **503**, L101 (1998).
- ⁵C. Xiong and S. Friedlander, *Proc. Natl. Acad. Sci. U.S.A.* **98**, 11851 (2001).
- ⁶J. Winter, *Plasma Phys. Controlled Fusion* **40**, 1201 (1998).
- ⁷A. Bouchoule, *Dusty Plasma* (Wiley, Chichester, 1999).
- ⁸V. Fortov, S. Khrapak, A. Ivlev, A. Khrapak, and G. Morfill, *Phys. Rep.* **421**, 1 (2005).
- ⁹Y. Watanabe, *J. Phys. D* **39**, R329 (2006).
- ¹⁰L. Boufendi and A. Bouchoule, *Plasma Sources Sci. Technol.* **3**, 262 (1994).
- ¹¹S. Nunomura, M. Shiratani, K. Koga, M. Kondo, and Y. Watanabe, *Phys. Plasmas* **15**, 080703 (2008).
- ¹²L. Ravi and S. Girshick, *Phys. Rev. E* **79**, 026408 (2009).
- ¹³Y. Mankelevich, M. Olevanov, A. Pal', T. Rakhimova, A. Ryabinkin, A. Serov, and A. Filippov, *Plasma Phys. Rep.* **35**, 191 (2009).
- ¹⁴R. Bingham and V. Tsytovich, *IEEE Trans. Plasma Sci.* **29**, 158 (2001).
- ¹⁵S.-H. Hong, J. Räscher, and J. Winter, *Proceedings of the 33rd EPS Conference on Plasma Physics* (European Physical Society, Rome, 2006).
- ¹⁶J. Winter (private communication), 2010.
- ¹⁷V. Fortov, A. Nefedov, V. Molotkov, M. Poustylnik, and V. Torchinsky, *Phys. Rev. Lett.* **87**, 205002 (2001).
- ¹⁸M. Schwabe, M. Rubin-Zuzic, S. Zhdanov, H. Thomas, and G. Morfill, *Phys. Rev. Lett.* **99**, 095002 (2007).
- ¹⁹A. Ivlev, G. Morfill, and U. Konopka, *Phys. Rev. Lett.* **89**, 195502 (2002).
- ²⁰U. Konopka, F. Mokler, A. V. Ivlev, M. Kretschmer, G. E. Morfill, H. M. Thomas, H. Rothermel, V. E. Fortov, A. M. Lipaev, V. I. Molotkov, A. P. Nefedov, Y. M. Baturin, Y. Budarin, A. I. Ivanov, and M. Roth, *New J. Phys.* **7**, 227 (2005).
- ²¹H. Thomas, G. Morfill, V. Fortov, A. Ivlev, V. Molotkov, A. Lipaev, T. Hagl, H. Rothermel, S. Khrapak, R. Sütterlin, M. Rubin-Zuzic, O. F. Petrov, V. I. Tokarev, and S. K. Krikalev, *New J. Phys.* **10**, 033036 (2008).
- ²²We used microspheres with an even dispersion of magnetic material (gamma Fe₂O₃ and Fe₃O₄) throughout the PS bead. The particles contain 20% iron and were superparamagnetic (i.e., with no residual magnetism).
- ²³P. Epstein, *Phys. Rev.* **23**, 710 (1924).
- ²⁴U. Konopka, *Simple particle identification and tracking*, see <http://robert3.mpe.mpg.de/~plasma/spit/doc/masterindex.html>.
- ²⁵H. Hamaker, *Physica (Amsterdam)* **4**, 1058 (1937).
- ²⁶J. Israelachvili, *Intermolecular and Surface Forces* (Academic, San Diego, 1992).
- ²⁷J. Manweiler, T. Cravens, and T. Armstrong, *Adv. Space Res.* **13**, 175 (1993).
- ²⁸S. Vladimirov, S. Maiorov, and N. Cramer, *Phys. Rev. E* **67**, 016407 (2003).

Interaction of two-dimensional plasma crystals with upstream charged particles

C.-R. DU^(a), V. NOSENKO, S. ZHDANOV, H. M. THOMAS and G. E. MORFILL

Max Planck Institute for Extraterrestrial Physics - Giessenbachstraße, 85748 Garching, Germany, EU

received 6 July 2012; accepted 7 August 2012

published online 13 September 2012

PACS 52.27.Lw – Dusty or complex plasmas; plasma crystals

PACS 52.25.Fi – Transport properties

PACS 52.27.Gr – Strongly-coupled plasmas

Abstract – Two-dimensional plasma crystals are characterized by a strong up-and-down asymmetry not only due to gravity but also due to the presence of plasma flow at the location of particles. We study for the first time the interaction of a single-layer plasma crystal with charged extra particles located above it (upstream of the flow of ions). Upstream extra particles tend to move between the rows of particles in the crystal, accelerate to supersonic speeds, and excite attraction-dominated Mach cones and wakes in the crystal.

Copyright © EPLA, 2012

Introduction. – A complex plasma is a weakly ionized gas containing ions, electrons, as well as small solid particles [1,2]. The particles are usually negatively charged due to the high thermal speed of electrons. The charge of particles ranges from a few hundreds to several thousands of elementary charges depending on the particle size and discharge conditions. In ground-based experiments the particles can levitate in the pre-electrode area against gravity by a strong electric field. Under certain experimental conditions they can be confined in a single layer and self-organize in a triangular lattice with hexagonal symmetry. Such system is known as 2D plasma crystal. The in-plane interaction between particles in this system is well described by screened Coulomb (Yukawa) potential with the screening length defined mainly by electrons [3–5].

Since the discovery of plasma crystals [6–8], various experiments have been performed with 2D plasma crystals including melting [9,10], recrystallization [11], defect transport [12], etc. In the course of such experiments, one often observes *extra* particles apart from the main 2D lattice layer after injecting particles into plasma. Those particles, which can be agglomerates or contaminations, sometimes move at a high speed, disturb the lattice, and can easily spoil the desired experiments by creating wave patterns within the lattice layer. When the extra particle speed is higher than the sound speed of the lattice, the disturbance forms a Mach cone. The Mach cones and

wakes associated with extra particles moving beneath the lattice layer were well studied in the past decade [13–17]. This phenomenon can be used for diagnostic purpose. In fact, by measuring the angle of a Mach cone and the speed of the source of disturbance, the sound speed of the crystalline lattice can be directly estimated. This method was used for 2D as well as 3D plasma crystals [17–19]. Besides measuring the sound speed of a plasma crystal, one can also use the extra particles to heat the crystalline lattice [20].

However, in many cases one needs an undisturbed 2D plasma crystal to perform some delicate experiments, *e.g.*, to investigate the dynamics of a perfect crystal. It is relatively easy to get rid of the extra particles beneath the lattice layer (downstream of the flow of ions). In practice one can drop those extra particles on the bottom electrode by reducing the discharge power at higher pressure. We call this process “purification”.

In the experiments performed in our laboratory, Mach cones and related wakes were sometimes observed in 2D plasma crystals even after purification. Such wave patterns happened to be induced by extra particles located *above* the lattice layer (upstream of the flow of ions), and showed many different features.

In this letter we report for the first time on the observation of channeling and leapfrog motion of upstream extra particles, accompanied by the excitation of attraction-dominated wakes in the lattice.

Experimental setup and conditions. – The experiments were performed in a modified Gaseous

^(a)E-mail: chengran.du@mpe.mpg.de

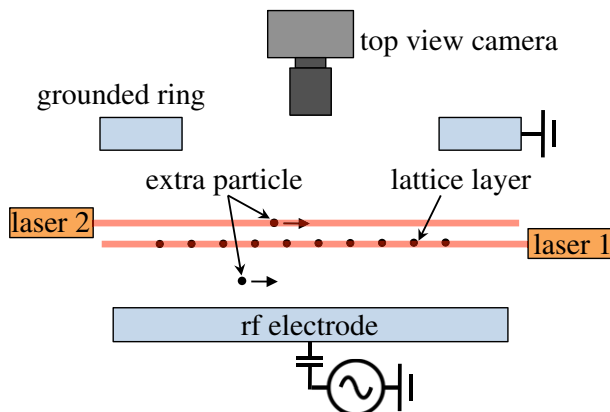


Fig. 1: Sketch of experimental setup with a modified GEC chamber. The bottom electrode is powered by rf generator at 13.56 MHz, the upper grounded ring and the chamber walls (not shown here) serve as the counter-electrode. Laser 1 shines a horizontal laser sheet to illuminate the lattice layer of 2D plasma crystal while laser 2 illuminates an extra particle outside the lattice layer. The optical axes of the lasers are actually oriented at 90° to each other. Particle motion in the lattice layer as well as of the extra particle can be simultaneously recorded by a video camera with top view.

Electronics Conference (GEC) rf reference cell [21], see fig. 1. Argon plasma was sustained using a capacitively coupled rf discharge at 13.56 MHz. The input power was set at 20 W.

We used monodisperse melamine formaldehyde (MF) and polystyrene (PS) particles to create 2D plasma crystals suspended above the bottom rf electrode. The MF particles have a diameter of $9.19 \pm 0.09 \mu\text{m}$ and mass density of 1.51 g/cm^3 , while the PS particles have a diameter of $11.36 \pm 0.12 \mu\text{m}$ and mass density of 1.05 g/cm^3 . Gas pressure was maintained at about 0.65 Pa; the corresponding neutral gas damping rate was $\gamma \simeq 0.77 \text{ s}^{-1}$ for MF particles and $\gamma \simeq 0.91 \text{ s}^{-1}$ for PS particles [22]. Further experimental parameters are listed in table 1. The lattice layer was illuminated by a horizontal laser sheet shining through a side window of the chamber. A high-resolution video camera (Photron FASTCAM 1024 PCI) was mounted above the chamber, capturing a top view with a size of $42 \times 42 \text{ mm}^2$, as sketched in fig. 1. The recording rate was set at 60 frames per second.

Mach cones and wakes. – We performed two separate experiments intended to observe two different types of Mach cones. For the sake of simplicity, in this letter we name the Mach cones in the lattice observed after its purification the “type-I” Mach cones. In contrast, the well-known Mach cones excited by extra particles beneath the lattice layer are called the “type II”. To observe the type-II Mach cones, we did not purify the plasma crystal so that big extra particles remained in the discharge. To make the results comparable, two cases with the

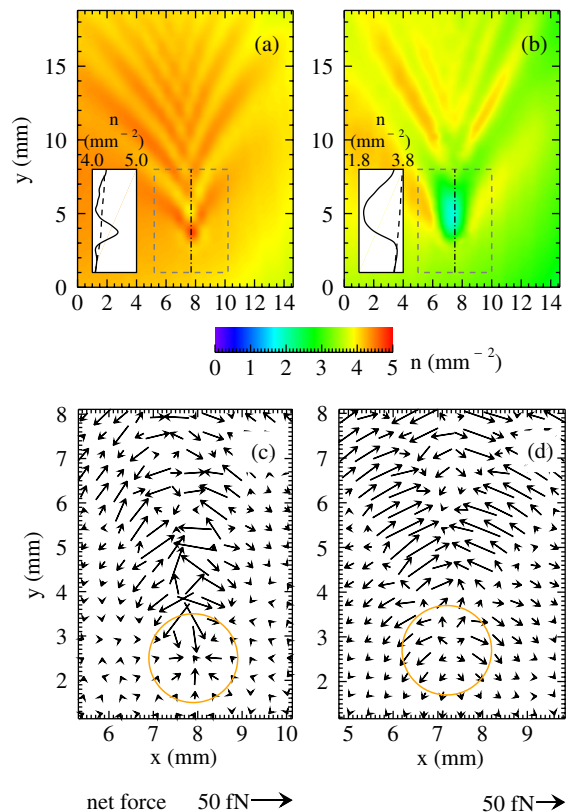


Fig. 2: Comparison of the particle areal number density n and net force between (a), (c) type-I (experiment 1 in table 1) and (b), (d) type-II (experiment 2 in table 1) Mach cones. The maps for type-I and type-II Mach cones are averaged from data for 30 and 20 consecutive video frames, respectively. The insets show the density profile (solid lines) along the symmetry axis (marked by the dash-dotted lines). The dashed lines in the insets represent the density profile for the undisturbed lattice. The net force $\mathbf{F}_n = m\mathbf{a} + \gamma m\mathbf{v}$ acting on the particles in the lattice at the apex of the Mach cone (marked by the dashed rectangle in (a) and (b)) is shown in panels (c) and (d). The orange circles highlight the apex of the Mach cones.

similar Mach numbers¹ but related to two different excitation sources were selected, see fig. 2. The particle areal number density map and the net force vector field corresponding to the type-I Mach cone are shown in the left panels in fig. 2. The wings of the Mach cone are clearly recognizable in both plots. The half-opening angle between the wings (“cone angle” in what follows) is measured to be $\mu = 55^\circ \pm 10^\circ$. By using the well-known Mach cone relation $\sin \mu = M^{-1}$, where $M > 1$, one can obtain $M \simeq 1.2$. The measured Mach number agrees well with the value estimated using the phonon spectrum method [23]. Note that the lateral wakes are also well resolved in the density map; these can be used for diagnostic purpose [24].

In the density map, fig. 2(a), there is a density increase at the apex of the type-I Mach cone. Compared to the

¹The Mach number is defined as $M = v_d/C_L$, where v_d is the speed of disturbance (extra particle) and C_L is the longitudinal sound speed of the crystalline lattice.

Table 1: Experimental parameters^a including the particle material and diameter d , charge number $Z = -Q/e$, interparticle distance^b Δ , screening length λ_D , longitudinal sound speed C_L , extra particle speed v_d , Mach number M , and Mach cone type (see text for details). The particles were suspended in an argon discharge at the pressure of 0.65 Pa and discharge power of 20 W.

Experiment	Particle material	d (μm)	Z	Δ (μm)	λ_D (μm)	C_L (mm/s)	Extra particle	v_d (mm/s)	M	Mach cone type
1	MF	9.19	15400	520	390	27	upstream	32	1.2	I
2	MF	9.19	16300	560	600	33	downstream	42	1.3	II
3	MF	9.19	15000	610	300	17	upstream	24	1.4	I
4	MF	9.19	16100	560	400	26	downstream	42	1.6	II
5	PS	11.36	19000	650	560	27	upstream	29	1.1	I

^aError bars: $\pm 13\%$ for Z , $\pm 45\%$ for λ_D , $\pm 15\%$ for C_L , $\pm 5\%$ for v_d , and $\pm 15\%$ for M .

^b Δ is obtained from the first peak of the pair correlation function. The crystalline lattice is slightly inhomogeneous (2% at the most).

undisturbed value² the particle density increases from 4 mm^{-2} to 4.5 mm^{-2} . The reason for that is simple: The particles in the lattice layer are dragged toward each other, resulting in an increase of the local particle density. This is clearly seen in the net force vector field shown in fig. 2(c).

As to the “conventional” type-II Mach cone, the density at the apex drops down sharply from 3.7 mm^{-2} (undisturbed particle density) to 1.9 mm^{-2} , producing a hole in the lattice clearly seen in fig. 2(b). The density drops because the lattice particles at the apex of the Mach cone are repelled by the extra particle, see fig. 2(d). The repulsion is caused by the Yukawa repulsive force between the extra particle and the particles in the lattice layer, all of which are negatively charged. The cone angle³ is $\mu = 50^\circ \pm 6^\circ$.

Extra particle diagnostics. – In order to trace the extra particle originating the Mach cone, we installed a second laser at 90° to the first one. This laser shines a laser sheet, which is parallel to the first laser sheet, as shown in fig. 1. The height of the laser can be finely adjusted with accuracy of $10\ \mu\text{m}$. Using two lasers simultaneously and registering the light scattered by the particles with the same camera allowed us to image the lattice layer together with the extra particle. (The depth of field of the camera lens is larger than the distance between the extra particle and the lattice layer.) The trajectory of the extra particle is therefore overlapped with the trajectories of particles in the lattice layer, see figs. 3(a), (b). That fits well with our goals.

The extra particles beneath the lattice layer moved at much lower heights. They could be observed if we lowered the height of the second laser. For brevity, we call these particles “downstream” because they are located downstream of the ion flow in the (pre)sheath comparing to the particles in the lattice layer. As shown in fig. 3(b), the trajectory of this extra particle beneath the lattice layer is well resolved as well as the displacement of individual particles in the lattice layer. The extra particle

trajectory is rather smooth and apparently not influenced by the local structure of the lattice layer above it. By measuring the height difference between two laser sheets, we estimate the vertical distance of extra particle from the lattice layer to be $\Delta h = 800\ \mu\text{m}$. The Mach cone can already be seen in fig. 3(b). However, the cone structure is better resolved in the velocity vector field, fig. 3(d). It is clear that the extra particle repels the particles in the lattice layer right above it due to the Yukawa repulsion. The apex of the Mach cone follows this extra particle closely.

It is more difficult to find the source of type-I Mach cone. We scan the second laser vertically with small height steps to catch the trace of any possible source of disturbance. It turns out that the source of type-I Mach cone is an extra particle moving above the lattice layer. For the reason explained above, we call these particles “upstream”. The relative height of these particles above the lattice layer is estimated to be $\Delta h = 200\ \mu\text{m}$. There are several reasons why it is hard to visualize or in fact even notice the existence of such particles: i) This type of extra particles appears in a plasma crystal much less often than downstream particles, ii) these particles are generally smaller in size, resulting in a very dim trajectory recorded by the video camera, iii) the influence of such particle on the lattice layer is relatively small. As we already see in the density maps in fig. 2, the density variation caused by an upstream particle is much smaller than that caused by downstream particle. Thus it is easy to overlook such effect without careful analysis.

As a rule, the upstream particles appear to move slower than downstream particles. Their average velocity depends on the gas pressure, discharge power, particle size, etc. Such dependence is not the focus of this letter and will be reported elsewhere.

Extra particle-lattice interaction at the cone apex. – The computed velocity of particles in the lattice layer with Mach cones excited by upstream and downstream particles are shown in fig. 3(c) (type I) and fig. 3(d) (type II), respectively. It is immediately clear that they are strikingly different. First, in the vicinity of the apex

²Note that the unperturbed crystalline lattice inhomogeneity is small compared to the density variation caused by the extra particle.

³Measured in the particle speed map (not shown here).

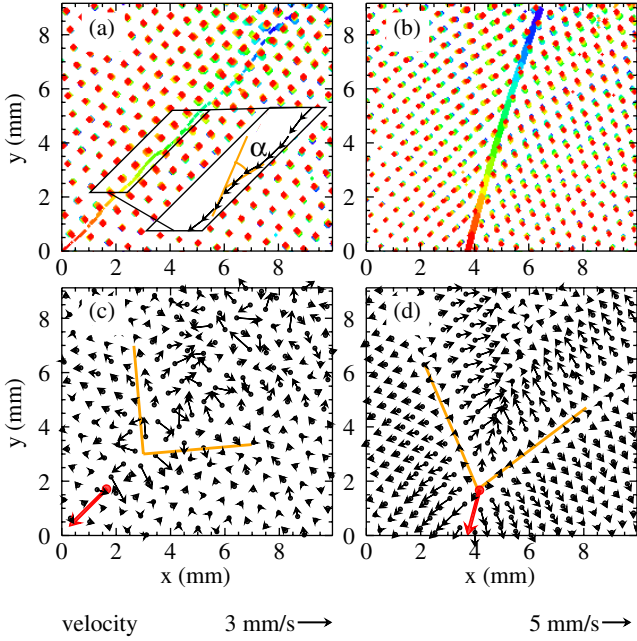


Fig. 3: Trajectories of upstream (a) and downstream (b) extra particles (experiments 3 and 4 in table 1). The particle positions are presented by superimposing a series of consecutive experimental images for 0.45 s (a) and 0.22 s (b) (color coded from blue to red). The trajectory of the upstream particle, showing a clear zig-zag feature, is magnified in the inset in (a). The scattering angle is $\alpha = 25^\circ \pm 3^\circ$. Panels (c) and (d) show snapshots of positions (black dots) and velocities (black scaled arrows) of particles in the lattice layer in a single frame as well as positions (red dots) of upstream and downstream particles and their velocities (red arrows, scaled 1:5), respectively. In (c) and (d) the Mach cone is highlighted by orange lines. The cone angles are $44^\circ \pm 12^\circ$ (c) and $38^\circ \pm 8^\circ$ (d).

of type-I cone, the lattice layer particles move toward the upstream particle (fig. 3(c)), whereas they are visibly repelled by the downstream particle (fig. 3(d)). Second, the apex of the Mach cone in fig. 3(c) has an elongated shape along the direction of the motion of the extra particle. The conjunction of the wings of the cone is therefore located slightly behind the moving upstream particle at a distance $\sim(2-3)\Delta$. In contrast, the apex of the type-II cone follows the extra particle position closely, as shown in fig. 3(d).

Importantly, the force field in figs. 2(c), (d) and the velocity field in figs. 3(c), (d) are similarly “polarized”, *i.e.*, both fields are simultaneously directed toward or away from the instantaneous location of the extra particle. Based on what we observed, the extra particle-lattice layer interaction is dominantly *attractive* for type-I cone (upstream particle) or dominantly *repulsive* for type-II cone (downstream particle).

We attribute the particle-lattice layer attraction to the *ion wake* formed underneath the upstream extra particle⁴.

⁴As is the case for any particle levitating in a discharge (pre) sheath.

Positive ions that concentrate locally below the extra particle exert an attractive force on the negatively charged particles of the lattice layer. This phenomenon is well known as the ion-wake effect causing, *e.g.*, the particles to pair [2,25–28]. The particle-lattice repulsion resulting from the Yukawa repulsive force at the apex of the type-II cone is a well-established effect [13–17].

Finally, the situation appears to be more complicated, and the particle-lattice interaction cannot be reduced only to the dominantly attractive or dominantly repulsive interactions. The examples discussed below can be properly addressed only suggesting the presence of competing repulsive-attractive interactions (which are also considered to be important for colloids [29]).

Channeling effect. – There is one more surprising observation regarding upstream particles: The long-term behavior of these particles demonstrates anomalous transport properties and elements of “strange kinetics” [30]. For instance, the particle is apparently able to channel⁵ between two aligned rows of particles in the crystalline layer (“wall particles” below), as seen in fig. 3(a).

Confinement force. The upstream particle is well confined in the channel. Comparing to the smooth trajectory of the downstream particle, fig. 3(b), the trajectory in fig. 3(a) has a zig-zag shape (see inset where a part of the trajectory in question is magnified). In other words, the extra particle, interacting with the crystal particles comprising the channel, evidently bounces and hence the effect of the wall particles on the extra particle is dominated by *repulsion*. By measuring the scattering angle α , one can estimate the confinement force F_c by using the relation $F_c \Delta t = m \langle v_d \rangle (1 - \cos \alpha)$, implying momentum conservation, where $\Delta t \simeq 0.08$ s is the time of scattering, m and $\langle v_d \rangle$ are the mass and mean (longitudinal) velocity of the extra particle, respectively. In the experiment presented here, the angle is measured to be $\alpha = 25^\circ \pm 3^\circ$, $v_d = 29 \pm 2$ mm/s, and the confinement force is estimated as $F_c \simeq 21$ fN. This value is about twice the neutral gas friction force $F_n \simeq 13$ fN.

Non-reciprocal interaction. The extra particle, passing through the channel, in turn exerts a force on the wall particles. This force deforms the lattice cells when the extra particle moves through. Studying this deformation, a certain conclusion can be made about the wall particle-extra particle interaction. From fig. 3(a) it follows immediately that this interaction is *non-reciprocal* because the wall particles behave as if they were attracted to rather than repelled by the similarly charged extra particle. This kind of non-reciprocity is indeed easy to address taking into account the ion wake (ion focus [2]) formed beneath the upstream particle.

Lattice cell deformation. In order to investigate the deformation of the lattice cell caused by the passage

⁵Channeling is a process that constrains the path of a charged particle in a crystalline solid [31].

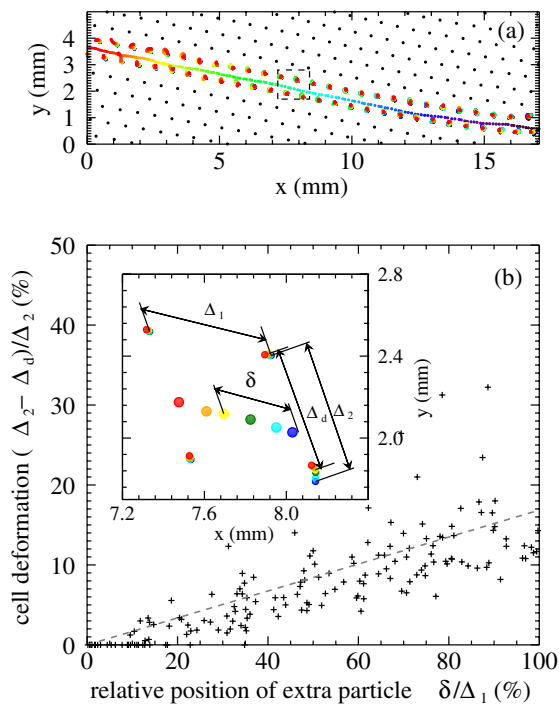


Fig. 4: Channeling of an upstream particle (a) and related cell deformation (b) (experiment 5 in table 1). Panel (a): black dots represent the lattice particles, colored dots represent positions of the extra particle and the “wall” particles color coded from blue to red for 0.66 s. Panel (b), inset: A magnified single cell (marked by a dashed-line rectangle in (a)) with color-coded particle positions (from blue to red with a time step of 4 ms). The dashed line is the least squares linear fit.

of extra particle in more detail, we performed another experiment with higher recording rate of 250 frames per second (experiment 5 in table 1). Accordingly, we used particles with larger diameter so that they can be well illuminated with the same illumination laser power without a significant change of the recording quality. An (unexpected) advantage of this case is that the extra particle above the lattice layer can even be traced using the same laser. This implies that the height difference is roughly of the laser sheet width or even smaller, $\Delta h \leq 100 \mu\text{m}$. This height difference is about one-fifth of the characteristic length $L_E = E/E'_h$ at the levitation height in the (pre)sheath, where E is the local electric field⁶. The expected difference in particle mass $\Delta m/m \approx 1.5\Delta h/L_E$ is less than 30–35%.

The extra particle track and the accompanying cell deformation are shown in fig. 4. The extra particle moves along the channel, which even bends slightly at $x > 14 \text{ mm}$ as shown in fig. 4(a). The deviation from the major track is small and a zig-zag feature is barely visible in this figure, indicating stronger confinement as compared to fig. 3(a). Let us focus on the dynamics of a single cell,

⁶Note that both PS and MF particles levitated at approximately the same height.

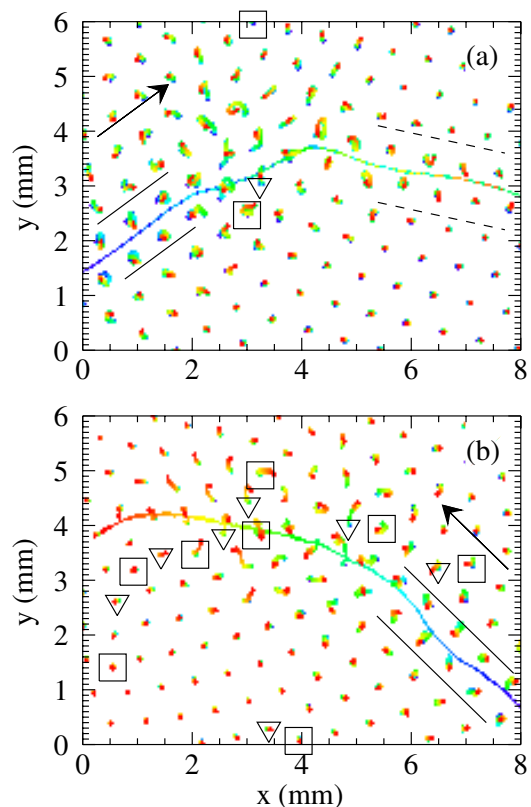


Fig. 5: Interaction of upstream particles with defects in the crystalline lattice. The particle positions obtained for the time interval of 0.4 s are shown as the solid dots color coded from blue to red. Initially in both cases the extra particles move in the channel (highlighted by two parallel solid lines). The initial velocities are approximately the same $v_d = 26 \pm 1 \text{ mm/s}$. (a) Single point defect scattering; the scattered particle is captured in a new channel (highlighted by two parallel dashed lines) where it moves with the velocity $v_d = 27 \pm 1 \text{ mm/s}$. (b) Interaction with a large-angle grain boundary; the extra particle, being initially scattered by a single defect, left the channel and penetrated the chain of defects, jumping from one position to another with the mean velocity $v_d = 19 \pm 3 \text{ mm/s}$. The 7-fold cells are marked by triangles, and the 5-fold cells are marked by squares.

see the inset in fig. 4(b). When the extra particle enters (through the right boundary in the case considered) the cell deforms as indicated by the color coding in the inset. In order to quantify this deformation, we introduce the relative cell deformation $(\Delta_2 - \Delta_d)/\Delta_2$, where $\Delta_{2(d)}$ is the undisturbed (disturbed) length of the cell side transversal to the extra particle track; the relative position of the extra particle inside the cell δ/Δ_1 , where Δ_1 is the length of the side of the undisturbed cell along the track, and δ is the displacement of the extra particle measured from the right boundary of the cell, as shown in fig. 4. The deformation depends linearly on the relative position of extra particle: $\delta/\Delta_1 = k(\Delta_2 - \Delta_d)/\Delta_2$, where $k = 0.14 \pm 0.01$. Note also that in fact the deformation does not only depend on the relative position of the extra particle, but also on its

velocity: At a fixed δ/Δ_1 , the slowing-down of the particle leads to a higher deformation of the lattice up to 30%, as seen in fig. 4(b).

Interaction with lattice defects. The character of the upstream extra particle motion depends on the local structure of the lattice layer. Sometimes the extra particles move in irregular trajectories as we observed in a number of experiments (two examples are shown in fig. 5). This can be explained by the channel distortion. For instance, when the channel is blocked by a structural defect the extra particle collides with the defect and scatters leaving the channel. Depending on the relative kinetic energy the collision might be elastic or inelastic. After the collision the particle is often again involved in the channeling process, see fig. 5(a), being again captured by and accelerated along a channel with a new orientation. Sometimes it is a challenge for an extra particle to find a new suitable channel, and it remains quasi-free “leapfrog” jumping for a longer time from one position to another one but at an essentially lower velocity, see fig. 5(b). This requires further careful analysis.

To conclude, the upstream extra particles happened to be an extremely useful tool to effectively test the anomalous kinetics effects and the particle-lattice interaction. Those particles appeared to be weakly, quasi-elastically interacting with a strongly coupled 2D complex plasma. That allowed us to explore the anomalous long-term channeling, leapfrog motion, attraction-dominated wakes in the lattice, all at the “atomistic” level.

We thank ALEXEI IVLEV for valuable discussions. The research leading to these results has received funding from the European Research Council under the European Union’s Seventh Framework Programme (FP7/2007-2013)/ERC Grant agreement 267499.

REFERENCES

- [1] FORTOV V. E., KHRAPAK A. G., KHRAPAK S. A., MOLOTKOV V. I. and PETROV O. F., *Phys. Usp.*, **47** (2004) 447.
- [2] MORFILL G. E. and IVLEV A. V., *Rev. Mod. Phys.*, **81** (2009) 1353.
- [3] HOMANN A., MELZER A., PETERS S. and PIEL A., *Phys. Rev. E*, **56** (1997) 7138.
- [4] ROSENBERG M. and KALMAN G., *Phys. Rev. E*, **56** (1997) 7166.
- [5] IVLEV A. V., ZHDANOV S. K., KHRAPAK S. A. and MORFILL G. E., *Phys. Rev. E*, **71** (2005) 016405.
- [6] CHU J. H. and I L., *Phys. Rev. Lett.*, **72** (1994) 4009.
- [7] THOMAS H., MORFILL G. E., DEMMEL V., GOREE J., FEUERBACHER B. and MÖHLMANN D., *Phys. Rev. Lett.*, **73** (1994) 652.
- [8] HAYASHI Y. and TACHIBANA K., *Jpn. J. Appl. Phys.*, **33** (1994) L804.
- [9] NOSENKO V., ZHDANOV S., IVLEV A. V., MORFILL G., GOREE J. and PIEL A., *Phys. Rev. Lett.*, **100** (2008) 025003.
- [10] NOSENKO V., ZHDANOV S. K., IVLEV A. V., KNAPEK C. A. and MORFILL G. E., *Phys. Rev. Lett.*, **103** (2009) 015001.
- [11] KNAPEK C. A., SAMSONOV D., ZHDANOV S., KONOPKA U. and MORFILL G. E., *Phys. Rev. Lett.*, **98** (2007) 015004.
- [12] NOSENKO V., ZHDANOV S. and MORFILL G., *Phys. Rev. Lett.*, **99** (2007) 025002.
- [13] SAMSONOV D., GOREE J., MA Z. W., BHATTACHARJEE A., THOMAS H. M. and MORFILL G. E., *Phys. Rev. Lett.*, **83** (1999) 3649.
- [14] SAMSONOV D., GOREE J., THOMAS H. M. and MORFILL G. E., *Phys. Rev. E*, **61** (2000) 5557.
- [15] DUBIN D. H. E., *Phys. Plasmas*, **7** (2000) 3895.
- [16] SCHWEIGERT V. A., SCHWEIGERT I. V., NOSENKO V. and GOREE J., *Phys. Plasmas*, **9** (2002) 4465.
- [17] HAVNES O., HARTQUIST T. W., BRATTLI A., KROESEN G. M. W. and MORFILL G., *Phys. Rev. E*, **65** (2002) 045403.
- [18] JIANG K., NOSENKO V., LI Y. F., SCHWABE M., KONOPKA U., IVLEV A. V., FORTOV V. E., MOLOTKOV V. I., LIPAEV A. M., PETROV O. F., TURIN M. V., THOMAS H. M. and MORFILL G. E., *EPL*, **85** (2009) 45002.
- [19] SCHWABE M., JIANG K., ZHDANOV S., HAGL T., HUBER P., IVLEV A. V., LIPAEV A. M., MOLOTKOV V. I., NAUMKIN V. N., SÜTTERLIN K. R., THOMAS H. M., FORTOV V. E., MORFILL G. E., SKVORTSOV A. and VOLKOV S., *EPL*, **96** (2011) 55001.
- [20] NUNOMURA S., ZHDANOV S., SAMSONOV D. and MORFILL G., *Phys. Rev. Lett.*, **94** (2005) 045001.
- [21] NOSENKO V., IVLEV A. V. and MORFILL G. E., *Phys. Rev. Lett.*, **108** (2012) 135005.
- [22] LIU B., GOREE J., NOSENKO V. and BOUFENDI L., *Phys. Plasmas*, **10** (2003) 9.
- [23] NUNOMURA S., GOREE J., HU S., WANG X. and BHATTACHARJEE A., *Phys. Rev. E*, **65** (2002) 066402.
- [24] NOSENKO V., GOREE J., MA Z. W., DUBIN D. H. E. and PIEL A., *Phys. Rev. E*, **68** (2003) 056409.
- [25] LAMPE M., JOYCE G., GANGULI G. and GAVRISHCHAKA V., *Phys. Plasmas*, **7** (2000) 3851.
- [26] MELZER A., SCHWEIGERT V. A. and PIEL A., *Phys. Scr.*, **61** (2000) 494.
- [27] IO C.-W., CHAN C.-L. and I L., *Phys. Plasmas*, **17** (2010) 053703.
- [28] KROLL M., SCHABLINSKI J., BLOCK D. and PIEL A., *Phys. Plasmas*, **17** (2010) 013702.
- [29] OLSON REICHHARDT C. J., REICHHARDT C. and BISHOP A. R., *Phys. Rev. Lett.*, **92** (2004) 016801.
- [30] SHLESINGER M. F., ZASLAVSKY G. M., KLAFTER J. and MORFILL G., *Nature*, **363** (1993) 31.
- [31] FELDMAN L. C., MAYER J. W. and PICRAUX S. T., *Materials Analysis by Ion Channeling* (Academic Press, New York) 1982.

Lane formation in binary complex plasmas: Role of non-additive interactions and initial configurations

K. JIANG^(a), C.-R. DU, K. R. SÜTTERLIN, A. V. IVLEV and G. E. MORFILL

Max Planck Institute for Extraterrestrial Physics - 85741 Garching, Germany, EU

received 27 September 2010; accepted in final form 30 November 2010

published online 12 January 2010

PACS 52.27.Lw – Dusty or complex plasmas; plasma crystals

PACS 64.75.Cd – Phase equilibria of fluid mixtures, including gases, hydrates, etc.

PACS 64.75.Gh – Phase separation and segregation in model systems (hard spheres, Lennard-Jones, etc.)

Abstract – In this letter, we study the influence of non-additive interactions on lane formation, using Langevin dynamics simulations. Lane formation and positive non-additivity have recently been observed in binary complex plasmas on board the International Space Station (ISS). Positive non-additivity of particle interactions is known to stimulate phase separation (demixing), but its effect on lane formation is unknown. We show that there is a non-additivity–stimulated crossover from the normal laning mode to a demixing-dominated laning mode. To analyze this crossover on the individual particle level we applied a very sensitive order parameter for lane formation based on anisotropic scaling indices. Extensive numerical simulations enabled us to identify a critical value of the non-additivity parameter Δ for the crossover. In addition the simulations revealed that the dynamics of lane formation is strongly influenced by the exact spatial configurations at the very moment of contact between two different complex plasmas.

Copyright © EPLA, 2010

Introduction. – The formation of lanes can be found pervasively in nature when two species are moving toward and penetrating into each other. It is commonly known from pedestrian dynamics in highly populated pedestrian areas [1] that human beings tend to form lanes to maximize the traffic flow. A similar phenomenon was also found in army ants, the formation of distinct traffic lanes is favorable in order to minimize congestion [2]. Lane formation, as an instability on the particle scale, also drew significant attention in different branches of physics, such as colloidal dispersions [3–6], lattice gases [7], molecular ions [8], and recently, in complex plasmas [9,10].

Complex plasmas consist of micron-sized particles immersed in a plasma, where dust particles are normally negatively charged and interact with each other via a screened Coulomb potential [11–13]. The first lane formation experiments in binary complex plasmas [9] were carried out under microgravity conditions with a rf discharge in the PK-3 Plus laboratory [14]. In these experiments, two different sizes of spherical melamine-formaldehyde (MF) microparticles were used. Small microparticles were driven and penetrated into a fairly homogeneous cloud formed by large particles. The

penetration featured remarkable streaming lanes, as can be seen in fig. 1. In refs. [9] and [10] this phenomenon was compared to Langevin dynamics (LD) simulations assuming an additive Yukawa interaction between particles to emphasize the physics leading to lane formation. Even though demixing was noticed in the same experiment the influence of it was specifically neglected in these previous publications. In binary complex plasmas the inter-particle interaction exhibits asymmetry, *i.e.*, for point particles of type “1” and “2” with purely repulsive interaction, the 1-2 (inter-species) interaction is always more repulsive than the geometric mean of 1-1 and 2-2 interactions [15]. This asymmetry in the mutual interaction is called “interaction non-additivity”, and in the case of complex plasma it is always positive, which will stimulate demixing (phase separation). Numerical simulations of the phase separation in the absence of lane formation have been performed [16,17].

In this letter, we present extensive numerical simulations regarding lane formation in non-additive binary complex plasmas. This complements the previous studies on dynamics of lane formation in two fundamental ways. First, we could confirm the significant effect of initial configurations on both the onset and evolution of lanes, which was believed to be important in

^(a)E-mail: jiang@mpe.mpg.de

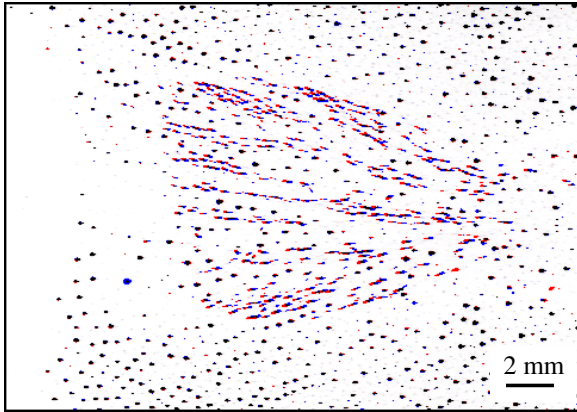


Fig. 1: (Color online) Lane formation in complex plasmas. A short burst of small ($3.4\ \mu\text{m}$) particles —seen as elongated red-blue streaks— is injected into a cloud of large ($9.2\ \mu\text{m}$) background particles —the almost round black spots. Small particles are driven towards the right. Lanes are formed by both small and large particles. The image is an overlay of two consecutive frames recorded in the experiment with a frame rate of 50 Hz, color coded red for first frame and blue for second frame.

the non-equilibrium laning transition [10]. Second, our analysis shows a crossover from normal laning mode to demixing-stimulated laning mode.

Non-additivity in binary complex plasmas. – For both large and small particles in the binary mixture of complex plasmas we assume that they can be treated as point-like and that their electric potential is screened exponentially with the same screening length λ (plasma screening length), but different interaction magnitudes ε_{ij} . The general form of inter-particle interaction can then be written as

$$\phi_{ij}(r) = \varepsilon_{ij} \frac{\exp(-r/\lambda)}{r}. \quad (1)$$

For like-particle interaction, $\varepsilon_{ij} = \varepsilon_{SS/LL}$ is the product of the effective charge and the real charge $Z_{S/L}$ [15] (subscripts S and L denote small and large particles, respectively). According to the Lorentz-Berthelot mixing rules [18] for the interaction between unlike particles one gets

$$\varepsilon_{ij} = \varepsilon_{LS} = \varepsilon_{SL} = (1 + \Delta) \sqrt{\varepsilon_{SS}\varepsilon_{LL}}. \quad (2)$$

Δ is the non-additivity parameter [15], which represents the asymmetry in the mutual interaction between unlike particles. Δ is always positive in binary complex plasmas [15]. Our model reduces to a typical Yukawa potential when $\Delta = 0$, which is the exact interaction model adopted in ref. [9].

Simulation. – In complex plasmas, dust particle motion can be described by the Langevin equation, which is a stochastic differential equation involving damping from neutral gas and Brownian motion of the dust particles:

$$\dot{\mathbf{p}}_i = \mathbf{F}_i - \gamma_i \mathbf{p}_i + \mathbf{R}_i, \quad (3)$$

where \mathbf{p}_i is the momentum of dust particle i , γ_i is the dust neutral gas collision frequency, and is given as $\gamma_i = 1.48 \frac{4\pi}{3} N_n m_n v_n \sigma_i^2 / m_i$ as in [19,20], where N_n , m_n and v_n are the density, mass and thermal velocity of the neutral gas, and σ_i is the diameter of the particles, m_i is the mass of the dust particle. $\mathbf{F}_i = -\sum \nabla \phi + \mathbf{F}_{ext}$ in eq. (3) is the deterministic force comprised of interparticle interactions and external force fields. The last term, $\mathbf{R}_i(t)$, is a stochastic force representing the Brownian motion of dust particles in plasma. It is commonly described by a delta-correlated stationary Gaussian process with zero-mean satisfying

$$\langle \mathbf{R}_i(0) \mathbf{R}_i(t) \rangle = 2\gamma_i k_B T m_i \delta(t). \quad (4)$$

Here, δ is the Dirac delta. The stochastic force and friction are related through the fluctuation-dissipation theorem [21] (the cooling by friction should cancel the heating by noise). The Langevin equation, eq. (3), is numerically integrated using an extended Beeman [22] algorithm as described in refs. [18,23].

All the plasma and particle parameters are chosen according to the experiments established in refs. [9,10]: screening length $\lambda = 150\ \mu\text{m}$, charges $Z_S = 4000e$ and $Z_L = 11000e$, particle diameter $\sigma_S = 3.4\ \mu\text{m}$ and $\sigma_L = 9.2\ \mu\text{m}$; mass density of MF particles $\rho_S = \rho_L = 1.5\ \text{g/cm}^3$. This results in friction coefficients $\gamma_S = 250\ \text{s}^{-1}$ and $\gamma_L = 92.4\ \text{s}^{-1}$. The mean inter-particle distances (before the penetration) are $a_S = 464\ \mu\text{m}$ and $a_L = 493\ \mu\text{m}$, respectively. The simulation was performed for a binary mixture of 5759 small and 12287 large particles within a simulation domain of $4.4\ \text{cm} \times 0.8\ \text{cm} \times 0.8\ \text{cm}$ in the x , y and z directions. Periodic boundary conditions are used for the y and z directions and a free boundary is adopted for the x -direction. Large particles are confined with an external parabolic potential at two edges within a region of 2.2 cm width along x at the center of the simulation domain. Small particles are initially confined and equilibrated within a region of 0.7 cm width along x separated by 0.3 cm from the large particles. Then $\mathbf{F}_{ext} = 0.08\mathbf{e}_x$ pN, the force driving small particles into the large-particle cloud, was instantaneously applied. Simulation snapshots are shown in fig. 2.

In order to study the effect of the non-additivity on the laning pattern, a set of 1000 statistically independent initial particle configurations had been prepared. The random seeds for homogeneous distribution of small and big particles had been varied. Both species were equilibrated for a short time to remove the artificial heat. Then the system was evolved with five different values of Δ (0.0, 0.1, 0.2, 0.3, 0.5). This resulted in a total of 5000 different penetration events. In addition to finding a systematic dependance of lane formation on Δ , this enabled us to study the effect of initial configurations on lane formation phenomena.

Analysis. – In order to quantify the lane formation in the LD simulations, we employed an anisotropic scaling

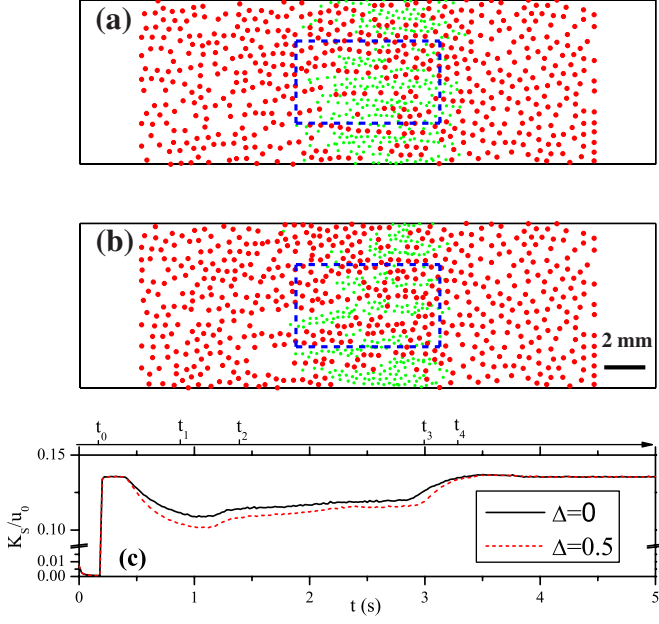


Fig. 2: (Color online) Comparison of two snapshots of lane formation in LD simulation for $\Delta = 0$ (a) and $\Delta = 0.5$ (b) taken at the same time step. Small particles (green) are driven from the left to the right through the cloud of large particles (red). Interestingly enough, small particles are able to penetrate faster for $\Delta = 0$. Also the lanes formed by both species are wider for larger Δ . The blue dashed box in each picture indicates the ROI in which we apply our analysis method. The evolution of the mean kinetic energy K_S of a single small particle during the whole penetration is shown in (c) with solid line representing the case of $\Delta = 0$ and dashed line representing $\Delta = 0.5$.

index method (ASIM) to realize a local nonlinear measure for structure characterization. Based on the weighted scaling index method [24], the anisotropic scaling index α is defined as

$$\alpha(\mathbf{r}_i, \xi, \epsilon, \theta) = \frac{2 \sum_{j=1}^N (d_{ij}/\xi)^2 e^{-(d_{ij}/\xi)^2}}{\sum_{j=1}^N e^{-(d_{ij}/\xi)^2}}, \quad (5)$$

where $d_{ij} = d(\mathbf{r}_i, \mathbf{r}_j, \epsilon, \theta)$ is the distance between particle i and j in a space stretched by ϵ along direction $\mathbf{u} = \begin{pmatrix} \cos \theta \\ \sin \theta \end{pmatrix}$, $-\pi/2 \leq \theta \leq \pi/2$. The coordinates in the new space can be expressed by applying a stretch matrix $\Lambda = \begin{pmatrix} 1 & 0 \\ 0 & \epsilon \end{pmatrix}$ and rotation matrix $\Omega = \begin{pmatrix} \cos \theta & \sin \theta \\ \sin \theta & -\cos \theta \end{pmatrix}$ on the simulation coordinate, *i.e.*, $\mathbf{r}'_i = \Lambda \Omega \mathbf{r}_i$, and thus, $d_{ij} = |\mathbf{r}'_i - \mathbf{r}'_j|$. The parameter ξ defines a spatial scale on which the α index is sensitive. By determining the value of θ that maximizes the difference $\alpha(\mathbf{r}_i, \xi, \epsilon, \theta + \pi/2) - \alpha(\mathbf{r}_i, \xi, \epsilon, \theta)$ we obtained a “preferred” direction \mathbf{u}_i associated with particle i , signifying the local anisotropy. The “length” of this anisotropy is given by ξ and ϵ describes the ratio between its “length” and “width”. The ASIM has been applied not only in complex plasma [9,10,25] but also in, *e.g.*, cosmology [24] and medical technology [26].

In order to characterize the global laning, we defined a laning-order parameter S , which is the largest eigenvalue of a second-rank tensor $Q = 2N^{-1} \sum_{i=1}^N \mathbf{u}_i \otimes \mathbf{u}_i - I$, where I is identity matrix. $S = 1$ denotes a perfect alignment while $S = 0$ represents a perfectly random phase.

Following ref. [9], we divided the volume of the simulation box into several slabs ($350 \mu\text{m}$ wide) in the z -direction (perpendicular to \mathbf{F}_{ext}) and analyzed the quasi-2D stringlike structure in the (x, y) -plane. To allow the direct comparison of our results, we used the same spatial scale ξ and anisotropic aspect ratio ϵ , *i.e.*, $\xi = 1200 \mu\text{m}$ and $\epsilon = 5$ for large particles. In order to reduce boundary effects in the analysis, we selected a fixed region of interest (ROI) in the center of the large-particle cloud (see fig. 2). For the calculation of S , only large particles inside the ROI were taken into account.

As suggested in ref. [9], we expected lane formation to be very sensitive to the initial spatial configuration of both particle species. A slight topological deviation in the initial encounter of two particle clouds could result in large differences of the laning pattern and penetration speed, introducing a large variance in the evolution of the global laning-order parameter S . To evaluate the influence of initial particle configuration and to separate it from the systematic effect induced by non-additivity we analyzed a large set of statistically independent numerical simulations as described in the simulation part. Eventually, we end up with a family of functions $S_k(\Delta, t)$, where the index k denotes the specific initial configuration. For fixed Δ and t the values of S_k form a Gaussian-like distribution, for which we determined the mean $\langle S \rangle$ and standard deviation \bar{S} . As an example the results for $\Delta = 0$ are shown in fig. 3.

Results and discussions. – The penetration of small particles into a large-particle cloud can be sectioned into the following stages. After the initial equilibration of both species, the driving force was applied on small particles at time t_0 . Small particles were driven toward the large-particle cloud until $t_1 \sim 50\%$ of the small particles entered the cloud of large particles. Both species formed lane structures during the penetration. For the convenience of analysis, we defined the time when the small particles moved into and out of ROI as t_2 and t_3 , respectively. Eventually at t_4 50% of small particles moved out of the large-particle cloud.

Two snapshots of laning with non-additivity parameter $\Delta = 0$ and $\Delta = 0.5$ are shown in fig. 2. One can see the normal laning phenomenon in fig. 2(a), where narrow lanes—at most 2 particles across—can be observed for both small and large particles. Whereas in fig. 2(b), one can see the demixing-stimulated laning mode. Like particles try to cluster due to the non-additivity and a demixing-stimulated laning mode is achieved. The averaged kinetic energy of small particles (total kinetic energy divided by small particle number), K_S , is shown in fig. 2(c), where the normalized factor $u_0 = 1.2 \times 10^{-10}$ erg. One can also see that K_S increases significantly after applying the driving

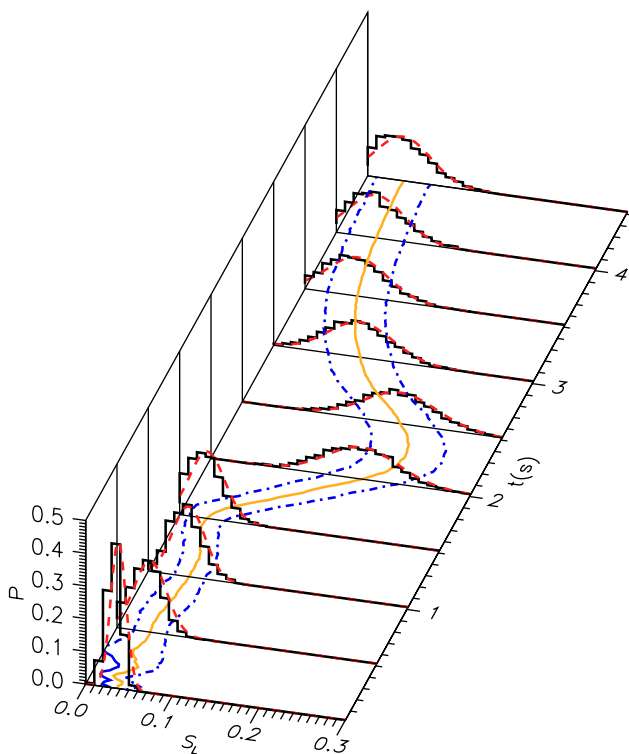


Fig. 3: (Color online) Role of the initial configurations. Temporal evolution of S_L , the global laning-order parameter for large particles, for $\Delta = 0$. The solid line (orange) shows the evolution of the mean value $\langle S_L \rangle$, the dash-dotted lines (blue) give the standard deviation \bar{S} . Normalized histograms of the original distribution of S_L at ten equidistant timesteps are displayed (solid black) for reference. Dashed lines (red) highlight the Gaussian fit to these histograms. For the first 0.5 s $\langle S_L \rangle$ shows some fluctuations due to incomplete thermalization. Small particles enter the ROI at $t \sim 1.5$ s. S_L has significant variance reflecting the strong influence of the initial particle configuration on lane formation.

force and then decreases when the initial contact between small particles and large-particle cloud occurs. Then K_S increases gradually between t_2 and t_3 when the lanes are formed. It is clear that the penetration speed $\langle v_S \rangle$ is slower in the case of $\Delta = 0.5$ than $\Delta = 0$ (both in the order of 1 cm/s), which can also be seen from the snapshots (cf. fig. 4(a)).

As mentioned in the simulation part, the initial configurations were varied. This resulted in different spatial configurations of the initial contact at t_1 , which consequently leads to the variance of S_L , as shown in fig. 3. Initially at t_0 the distribution of $S_k(\Delta, t)$ for large particles in the ROI is peaked very strongly, and broadens slightly till the impact of small particles at t_1 , mainly due to thermalization of the initial configurations. The distribution of S_k stays relatively stable until at t_2 small particles start to flow into the ROI, when the initial spatial deviations are magnified by the lane formation process. The standard deviation \bar{S}_L is doubled. Even after t_3 when the small particles leave the ROI and the large particles approach their undisturbed equilibrium, the variance

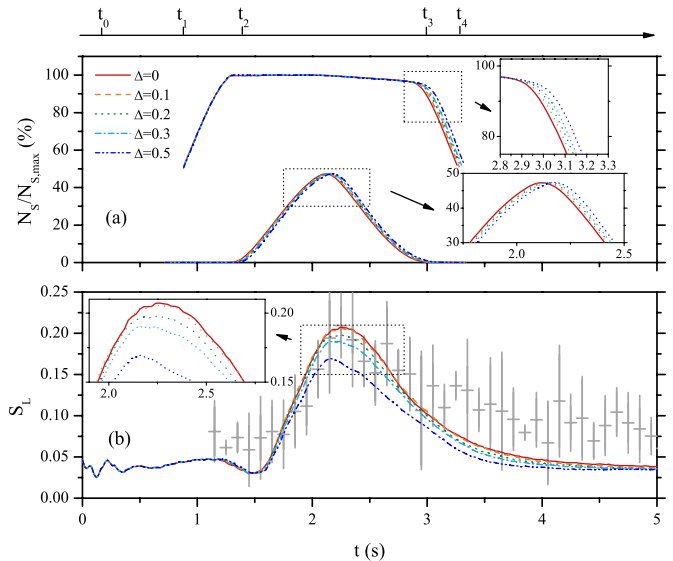


Fig. 4: (Color online) Dependence of lane formation on the non-additivity parameter Δ . (a) Percentage of small particles inside the cloud of large particles (upper curves) and the ROI (lower curves). Penetration speed depends on Δ , small particles need more time to cross the cloud of big particles for larger values of Δ . (b) The temporal evolution of $\langle S_L \rangle$. The values of $\langle S_L \rangle$ decreases systematically with increasing Δ . For comparison, the experiment results including error bars are overlotted.

in the distribution of S_k is not decreased in this relaxation process. This information is critical for experimental and numerical studies since one should not make decisive conclusions based on a few events. A rather large ensemble is necessary to separate the random influence of initial configurations from the systematic derivation that researchers are interested in, such as the non-additivity effect in this letter.

The systematic influence of non-additivity on the laning mode is studied using the average speed of small particles inside the cloud of large particles (fig. 4(a)) and the mean global order parameter for large particles $\langle S_L \rangle(\Delta, t)$ (fig. 4(b)). For $\Delta = 0$ small particles leave the large-particle cloud earlier than for higher non-additivity. This translates directly to a higher penetration speed $\langle v_S \rangle$. From the insert in fig. 4(a) it is clear that $\langle v_S \rangle$ decreases with Δ as we have shown in fig. 2(c).

The role of non-additivity can be very well probed by the mean global order parameter for large particles $\langle S_L \rangle(\Delta, t)$ as shown in fig. 4(b). The fluctuation of $\langle S_L \rangle$ between t_0 and t_1 are unrelated to the value of Δ . Small particles are not playing a role at this stage—due to the short range of the inter-particle interaction potential—and therefore non-additivity does not yet have any influence on $\langle S_L \rangle$. The cloud of large particles is still equilibrating, and reaches some intermediate plateau $\langle S_L \rangle \sim 0.02$ at $t \sim 0.5$ s. This finite initial value can be explained by the small number of large particles inside the ROI $\langle N_L \rangle \sim 100$, which limits the “homogeneity” of the ensemble.

Right before the penetration of small particles into the ROI at t_2 , large particles inside this area are compressed by the wave front excited by small particles and $\langle S_L \rangle$ shows a dip. The damping length of acoustic waves in the large-particle cloud is estimated to be $l_D = \omega_L \lambda / \gamma_L = 110 \mu\text{m}$ (within $1 a_L$), where ω_L is the dust plasma frequency of big particles. This explains why the dip of $\langle S_L \rangle$ starts to emerge slightly before the small particles entering the ROI. Between t_1 and t_2 , lanes are formed inside the ROI and $\langle S_L \rangle$ peaks up. The main effect of non-additivity on the evolution of $\langle S_L \rangle$ is the decrease of the peak value from 0.21 for $\Delta = 0$ to 0.17 for $\Delta = 0.5$ (see insert in fig. 4(b)). This can be explained by the change in morphology of the lanes formed by the particles. The global order parameter is sensitive to structures as defined by the parameters $\xi = 1200 \mu\text{m}$ and $\epsilon = 5$ chosen for the ASIM. These values were taken from refs. [9,10], that were optimized for simulations of additive particle interactions. The peak value therefore relates to the deviation from long narrow lines in the cases of increasing non-additivity.

After t_4 when most small particles have left the ROI, the large particles relax towards thermal equilibrium, $\langle S_L \rangle$ slowly decaying towards its base value ($\langle S_L \rangle \sim 0.03$). Still the system is in a different state than before the penetration of small particles. This can be derived from the change of \bar{S}_L and histogram of S_L at the initial stage of evolution as can be seen in fig. 3.

Conclusions. – Langevin dynamics simulations are employed to investigate the lane formation phenomenon with additive and non-additive particle interactions in binary complex plasmas under microgravity conditions. A crossover from the normal laning mode to a demixing-dominated laning mode is observed. This is similar to the transition from lane formation to classical Rayleigh-Taylor instability. For regular fluids this can be described in terms of the Weber number, which is the ratio of kinetic energy to surface tension [6]. However in mesoscopic systems hydrodynamic parameters like the surface tension are not well defined. Furthermore, for dissipative systems (such as complex plasmas or colloidal suspensions) the concept of a driving force (rather than energy) is more appropriate. Therefore F_{ext}/Δ , the ratio of the magnitude of the driving force to the non-additivity parameter (the microscopic source for surface tension), is the unambiguous way to describe the crossover, which is investigated for fixed F_{ext} by increasing Δ . For a vanishing non-additivity parameter, $\Delta = 0$, which would correspond to an infinite Weber number in the macroscopic case, small particles driven by an external force penetrate into large-particle clouds and form lane structures. When Δ is increased, the non-additivity-induced surface tension is built up, which would correspond to a decrease of the Weber number in a macroscopic system. Droplet-like lanes are formed and clear interfaces between unlike species emerge. A sensitive order parameter based on anisotropic scaling indices enabled us to measure the influence of non-additivity

and to identify the critical value of the non-additivity parameter ($\Delta > 0.1$) for the crossover. A huge number of simulations is necessary not only to reduce the influence of random fluctuations, but also to highlight the importance of the initial configurations. Even though the initial configurations are thermodynamically equivalent, the minuscule details of single-particle kinetics define the dynamics of laning.

The authors would like to thank A. WYSOCKI, H. LÖWEN, L.-J. HOU and C. RÄTH for helpful discussions, the members of the theory group of Max-Planck-Institute for extraterrestrial physics, for supplying ample computing time on their XGRID cluster. This work was supported by “Die Raumfahrt-Agentur des Deutschen Zentrums für Luft und Raumfahrt e. V. mit Mitteln des Bundesministeriums für Wirtschaft und Technologie aufgrund eines Beschlusses des Deutschen Bundestages unter dem Förderkennzeichen 50 WP 0203”.

REFERENCES

- [1] HELBING D., FARKAS I. J. and VICSEK T., *Phys. Rev. Lett.*, **84** (2000) 1240.
- [2] COUZIN I. D. and FRANKS N. R., *Proc. R. Soc. London, Ser. B*, **270** (2003) 139.
- [3] DZUBIELLA J., HOFFMANN G. P. and LÖWEN H., *Phys. Rev. E*, **65** (2002) 021402.
- [4] LEUNISSEN M. E., CHRISTOVA C. G., HYNINEN A.-P., ROYALL C. P., CAMPBELL A. I., IMHOF A., DIJKSTRA M., VAN ROIJ R. and VAN BLAADEREN A., *Nature*, **437** (2005) 235.
- [5] REX M. and LÖWEN H., *Eur. Phys. J. E*, **26** (2008) 143.
- [6] WYSOCKI A. and LÖWEN H., *J. Phys.: Condens. Matter*, **16** (2004) 7209.
- [7] SCHMITTMANN B. and ZIA R. K. P., *Phys. Rep.*, **301** (1998) 45.
- [8] NETZ R. R., *Europhys. Lett.*, **63** (2003) 616.
- [9] SÜTTERLIN K. R., WYSOCKI A., IVLEV A. V., RÄTH C., THOMAS H. M., RUBIN-ZUZIC M., GOEDHEER W. J., FORTOV V. E., LIPAЕV A. M., MOLOTKOV V. I., PETROV O. F., MORFILL G. E. and LÖWEN H., *Phys. Rev. Lett.*, **102** (2009) 085003.
- [10] SÜTTERLIN K., THOMAS H., IVLEV A., MORFILL G., FORTOV V., LIPAЕV A., MOLOTKOV V., PETROV O., WYSOCKI A. and LÖWEN H., *IEEE Trans. Plasma Sci.*, **38** (2010) 861.
- [11] SHUKLA P. K. and MAMUN A. A., *Introduction to Dusty Plasma Physics* (Institute of Physics Publishing, Bristol, Philadelphia) 2002.
- [12] SHUKLA P. K. and ELIASSON B., *Rev. Mod. Phys.*, **81** (2009) 25.
- [13] MORFILL G. E. and IVLEV A. V., *Rev. Mod. Phys.*, **81** (2009) 1353.
- [14] THOMAS H. M., MORFILL G. E., FORTOV V. E., IVLEV A. V., MOLOTKOV V. I., LIPAЕV A. M., HAGL T., ROTHERMEL H., KHRAPAK S. A., SÜTTERLIN K. R., RUBIN-ZUZIC M., PETROV O. F., TOKAREV V. I. and KRIVALEV S. K., *New J. Phys.*, **10** (2008) 033036.

- [15] IVLEV A. V., ZHDANOV S. K., THOMAS H. M. and MORFILL G. E., *EPL*, **85** (2009) 45001.
- [16] WYSOCKI A., RÄTH C., IVLEV A. V., SÜTTERLIN K. R., THOMAS H. M., KHRAPAK S., ZHDANOV S., FORTOV V. E., LIPAEV A. M., MOLOTKOV V. I., PETROV O. F., LÖWEN H. and MORFILL G. E., *Phys. Rev. Lett.*, **105** (2010) 045001.
- [17] JIANG K., HOU L. J., IVLEV A. V., LI Y. F., SÜTTERLIN K. R., DU C.-R., THOMAS H. M. and MORFILL G. E., to be submitted to *EPL*.
- [18] ALLEN M. P. and TILDESLEY D. J., *Computer Simulation of Liquids* (Clarendon Press, Oxford) 1987.
- [19] EPSTEIN P. S., *Phys. Rev.*, **23** (1924) 710.
- [20] KONOPKA U., *Wechselwirkungen geladener Staubteilchen in Hochfrequenzplasmen*, PhD thesis, Ruhr-Universität-Bochum (July 2007).
- [21] LEMONS D. S., *An Introduction to Stochastic Processes* (John Hopkins University Press) 2002.
- [22] BEEMAN D., *J. Comput. Phys.*, **20** (1976) 130.
- [23] HOU L. J., MIŠKOVIĆ Z. L., PIEL A. and SHUKLA P. K., *Phys. Plasmas*, **16** (2009) 053705.
- [24] RÄTH C., BUNK W., HUBER M. B., MORFILL G. E., RETZLAFF J. and SCHUECKER P., *Mon. Not. R. Astron. Soc.*, **337** (2002) 413.
- [25] IVLEV A. V., MORFILL G. E., THOMAS H. M., RÄTH C., JOYCE G., HUBER P., KOMPANEETS R., FORTOV V. E., LIPAEV A. M., MOLOTKOV V. I., REITER T., TURIN M. and VINOGRADOV P., *Phys. Rev. Lett.*, **100** (2008) 095003.
- [26] RÄTH C., MONETTI R., BAUER J., SIDORENKO I., MÜLLER D., MATSUURA M., LOCHMÜLLER E.-M., ZYSSET P. and ECKSTEIN F., *New J. Phys.*, **10** (2008) 125010.

Experimental investigation on lane formation in complex plasmas under microgravity conditions

C-R Du^{1,4}, K R Sütterlin¹, K Jiang¹, C R ath¹, A V Ivlev¹,
S Khrapak¹, M Schwabe^{1,5}, H M Thomas¹, V E Fortov²,
A M Lipaev², V I Molotkov², O F Petrov², Y Malentschenko³,
F Yurtschichin³, Y Lonchakov³ and G E Morfill¹

¹ Max-Planck-Institute for Extraterrestrial Physics, 85748 Garching, Germany

² Joint Institute for High Temperatures, 125412 Moscow, Russia

³ Yu A Gagarin Cosmonaut Training Center, 141160 Star City, Russia

E-mail: chengran.du@mpe.mpg.de

New Journal of Physics **14** (2012) 073058 (17pp)

Received 15 November 2011

Published 31 July 2012

Online at <http://www.njp.org/>

doi:10.1088/1367-2630/14/7/073058

Abstract. A series of experiments dedicated to probing the phenomenon of lane formation in binary complex plasmas over a broad range of parameters has been performed with the PK-3 Plus laboratory on board the International Space Station (ISS) under microgravity conditions. In the experiments, bunches of small particles were driven through a background of big particles. We show that the dynamics of lane formation varies considerably with the density of the background and the size ratio between small and big particles. For consecutive injections of small particles a memory effect of the previous penetration was discovered for the first time. This memory effect was investigated quantitatively with respect to the structure formation and the penetration speed. We show that the memory effect in lane formation is linear. In addition, we studied the crossover from lane formation to phase separation driven by the nonadditive interactions between small and big particles. We found that during this transition the small penetrating particles effectively cage the background particles.

 Online supplementary data available from stacks.iop.org/NJP/14/073058/mmedia

⁴ Author to whom any correspondence should be addressed.

⁵ Present address: Department of Chemical and Biomolecular Engineering, University of California, Berkeley, CA 94720, USA.

Contents

1. Introduction	2
2. The experimental setup and procedures	3
3. The analysis method	5
4. Dependence of lane formation on the number density ratio	6
5. Dependence of lane formation on the size ratio	9
6. Memory effect	10
7. Crossover from lane formation to phase separation	12
8. Conclusion	15
Acknowledgments	15
References	15

1. Introduction

Pattern formation in complex fluids has been a long-standing, intriguing topic, e.g. electric-field-induced pattern formation in colloidal dispersions [1], and ‘oscillons’ self-organized into clusters in granular materials [2]. The dissipative interactions through friction are a source of nonlinear dynamics and complexity which result in pattern formation on large scales. A complex plasma showing non-Newtonian behavior [3] and visco-elasticity [4] as a complex fluid is also the host of various pattern formation phenomena, e.g. plasma crystals [5–7], coaxial ring patterns in strong magnetic fields [8] and lane formation [9]. Lane formation is an evolving pattern formation that occurs when two species of particles are driven into each other. Like-driven particles form lanes and move collectively. Typically, the lanes exhibit considerable anisotropic structural order accompanied by an enhancement of mobility. Lane formation was discovered in complex plasmas in 2009 [9] and has been studied both experimentally [10] and numerically [11].

A complex plasma is comprised of ions, electrons, neutral gas and immersed particles, whose diameters range from the nanometer scale to several hundreds of micrometers [12, 13]. Those particles are charged either positively or negatively depending on the dominant charging mechanism [14, 15]. For low-temperature laboratory gas discharges, particles of micrometer size (microparticles) acquire negative charge due to the higher mobility of electrons, where the net charge is roughly proportional to their size. The resulting surface potential is screened by ions and electrons inside the plasma, which leads to repulsive Yukawa-type interactions. Under microgravity conditions the microparticles are trapped in the plasma potential well, and tend to form a homogeneous three-dimensional (3D) cloud usually with a void in the center [16]. Within the cloud, particles experience not only Yukawa-type interaction but also an electric force due to the plasma potential well, friction due to the neutral gas and an ion drag force due to the ion flow.

In this paper, we review a series of experiments on the lane formation observed in complex plasmas under microgravity conditions. The experiments presented here were performed in the PK-3 Plus laboratory [17] on board the International Space Station (ISS). The paper covers all lane formation experiment data from July 2006 until January 2011. This paper is organized as follows. In section 2, we introduce the setup of the PK-3 Plus laboratory, describe the experiment procedure and mention their limits. In section 3, the analysis method for quantifying

the lane structure is described in detail. In sections 4–7, we investigate different aspects of lane formation. Finally, the conclusions are presented in section 8.

2. The experimental setup and procedures

PK-3 Plus is the second-generation microgravity laboratory that was specially designed for complex plasma research on board the ISS [17]. Different types of experiments have been performed including externally excited wave propagation [18], heartbeat oscillation [19], plasma crystal formation [20], etc. The setup consists of a capacitively coupled radio-frequency (rf) chamber and surrounding infrastructure including laser illumination, a gas system, a video recording system, a vacuum system, as well as a control system. The chamber itself has a cubic shape and contains two circular electrodes that are 3 cm from each other, as shown in figure 1(b). Each electrode has a diameter of 6 cm and is surrounded by a grounded guard ring of 1.5 cm width. Each guard ring includes three dispensers, which allow the injection of monodisperse microparticles of six different sizes: silica microparticles with a diameter of $1.55 \pm 0.04 \mu\text{m}$ and melamine-formaldehyde (MF) microparticles with diameters of 2.55 ± 0.04 , 3.43 ± 0.06 , 6.81 ± 0.1 , 9.19 ± 0.09 and $14.9 \pm 0.26 \mu\text{m}$. The particles can be injected by shaking the dispenser controlled by a coil. The injected particle number can be tuned by varying the shaking time. The glass walls are made of quartz through which the dynamics of individual particles and the structure of the microparticle cloud can be recorded by three CCD cameras: the ‘overview (OV) camera’ includes the whole area inside the chamber, the ‘high resolution (HR) camera’ focuses on the center of the chamber and a ‘glow camera’ (not shown in the figure) records the plasma discharge with a similar field of view as the OV camera. In our experiments on lane formation, the videos are all recorded by the ‘quadrant view (QV) camera’, which records only half of the field of view captured by the OV camera with a higher spatial resolution. The maximal recording speed for all four cameras is 50 fps (frames per second). As shown in figure 1, the particles are illuminated by a laser sheet with a full-width at half-maximum (FWHM) of about $80 \mu\text{m}$ at the focal axis perpendicular to the cameras’ line of sight. The cameras and lasers are mounted on a translation stage which can move back and forth with a given speed. This function makes it possible to scan the particle cloud in the chamber and obtain 3D information. However, due to the limited scan speed, it is not possible to visualize the 3D information in some experiments with fast dynamics, such as lane formation.

The experiment procedure is relatively simple. After igniting the argon plasma, we inserted a relatively large number of particles of one type to fill the chamber and waited for a while to let the particles form a homogeneous background cloud. Then we injected particles of another species which are smaller than the existing particles in the chamber. We distinguish between the two particle species based on their kinetics. The small particles penetrate into the cloud of big particles due to the driving force F_d resulting from the electric force (plasma potential), ion drag force and neutral friction. Whether the lane structure can be formed during the penetration depends on several factors including the number density ratio, the size ratio between big and small particles and plasma parameters such as plasma potential. While the small particles penetrate the background cloud, the nonadditivity between small and big particles (an asymmetry in the mutual interactions between particles of different species [21]) leads to phase separation. The small particles start to form a dense droplet that finally settles around the central void.

The plasma conditions cannot be controlled directly. They depend on several control parameters such as the neutral gas type, neutral gas pressure, discharge power and the number of

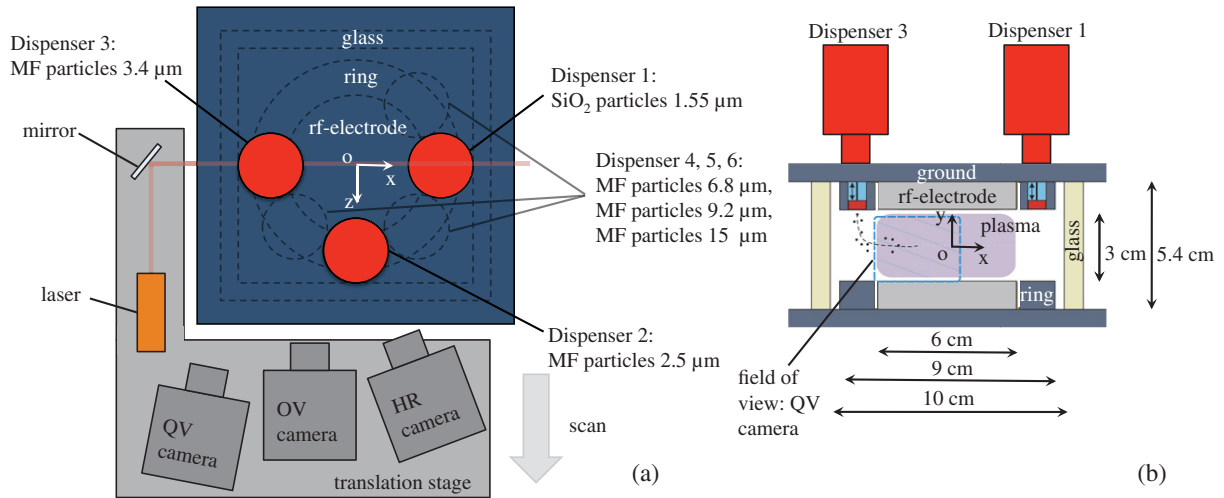


Figure 1. A sketch of the PK-3 Plus plasma chamber (b) and the particle observation system, with the definition of the coordinate system used throughout the paper. Panel (a) shows the top view of the chamber. The laser and the recording system are mounted on a translation stage that can move back and forth in the z -direction. The laser light is focused into a vertical sheet, approximately $80 \mu\text{m}$ wide in the focal plane. A total of six particle dispensers can independently inject mono-disperse spherical microparticles into the chamber. Panel (b) shows the side view of the chamber, along the cross section through the center.

microparticles injected into the discharge. In all the cases studied, lane structures of background particles are formed, unless the input power is too low to sustain a stable particle cloud [19].

The experiments described in this paper are performed in argon gas at a pressure of 30 Pa and at a peak-to-peak rf voltage of 40 V. This results in an effective current $I_{\text{eff}} = 6 \text{ mA}$ measured on the electrodes. Some experimental measurements of the plasma parameters in the PK-3 Plus chamber in ground-based conditions have recently been reported [22]. In order to get the order of magnitude estimate for the present experimental conditions, we use the results of SIGLO-2D plasma simulation published earlier [17]. For the above-mentioned conditions, the plasma density at the center of the discharge chamber (in the absence of particles) is estimated as $n_e \simeq n_i \simeq n_0 \simeq 8 \times 10^8 \text{ cm}^{-3}$ and the electron temperature is $T_e \simeq 4 \text{ eV}$. The ion temperature is expected to be equal to the neutral gas temperature $T_i \simeq T_n \simeq 0.025 \text{ eV}$. This results in the ion (electron) Debye radius of $\lambda_{Di} \simeq 40 \mu\text{m}$ ($\lambda_{De} \simeq 500 \mu\text{m}$) and the ion mean free path of $l_i = 70 \mu\text{m}$. The particle charges are then estimated taking into account the collisional [23] and ionization-enhanced [24] ion collection by the particle. The resulting charges are summarized in table 1. We point out that the presence of particles in the discharge can modify plasma parameters. In particular, the ion density in the particle cloud should exceed the electron density to keep quasi-neutrality. This, in turn, lowers the particle charges in comparison with the individual particle regime. We expect, however, that these effects are not dominant under the conditions investigated, since the value of the Havnes parameter $P = (aT_e/e^2)(n_p/n_0)$ remains below unity in all the experiments discussed in this paper [25] (here a is the particle radius and n_p is the particle number density).

Table 1. Values of the (individual) microparticle charge Q estimated for the conditions relevant to the described experiment (see the text).

$2a$ (μm)	2.55	3.4	6.8	9.2	14.9
$ Q/e $	1400	1900	4500	6900	14300

The particle number density ratio can be tuned relatively precisely and the size ratio between big and small particles is defined within a few per cent. Due to the mounting location of dispensers on the chamber and the camera position, only dispensers 2 and 3 (cf see figure 1), which contain MF particles with diameters of 2.55 ± 0.04 and $3.43 \pm 0.06 \mu\text{m}$, can be used for the penetration experiments. Particles injected from dispenser 3 enter the field of view from the left and their motion towards the center can be fully resolved: we call this ‘in-plane injection’. In contrast, particles injected from dispenser 2 move in the line of sight of the camera. Thus, they move perpendicular to the field of view, which allows us to record a full cross section through the penetration region, but not the motion of individual small particles: this is denoted as ‘in-the-line-of-sight injection’. Dispenser 1 injects $1.55 \mu\text{m}$ particles from the right-hand side. This field of view is visible only with the OV camera, the resolution of which is too low to identify the particle positions and motion.

3. The analysis method

In this paper, we focus on the lane structure formed by big particles in the background during the penetration. In order to quantify such structures, we employ the anisotropic scaling index method (ASIM) to realize a local nonlinear measure for structure characterization [26]. The ASIM has been applied to various studies, for instance complex plasma [27], cosmology [26] and medical image processing [28]. This method detects the ‘local lane structure’ of each particle by assessing the local scaling properties of particle density in the neighborhood. The size of the neighborhood and the degree of anisotropy are controlled by two additional characteristic parameters: the length R and aspect the ratio ϵ of ‘ideal’ lanes.

For a given set of particle positions, $[\mathbf{r}_j]$, $j = 1, \dots, N$, the anisotropic scaling index α is defined as

$$\alpha(\mathbf{r}_j, R, \epsilon, \theta) = \frac{2 \sum_{k=1}^N (d_{jk}/R)^2 e^{-(d_{jk}/R)^2}}{\sum_{k=1}^N e^{-(d_{jk}/R)^2}}, \quad (1)$$

where $d_{jk} = d(\mathbf{r}_j, \mathbf{r}_k, \epsilon, \theta)$ is the distance between particles j and k in a space stretched by ϵ along the direction $\mathbf{u} = \begin{pmatrix} \cos \theta \\ \sin \theta \end{pmatrix}$, $-\pi/2 \leq \theta \leq \pi/2$. In practice, we transform the coordinates of particle positions in the new space by applying a stretch matrix $\Lambda = \begin{pmatrix} 1 & 0 \\ 0 & \epsilon \end{pmatrix}$ and rotation matrix $\Omega = \begin{pmatrix} \cos \theta & \sin \theta \\ \sin \theta & -\cos \theta \end{pmatrix}$ on the experiment coordinates, i.e. $\mathbf{r}'_j = \Lambda \Omega \mathbf{r}_j$, and thus, $d_{jk} = |\mathbf{r}'_j - \mathbf{r}'_k|$. By determining the value of θ that maximizes the difference $\alpha(\mathbf{r}_j, R, \epsilon, \theta + \pi/2) - \alpha(\mathbf{r}_j, R, \epsilon, \theta)$, we obtain a ‘preferred’ direction \mathbf{u}_j associated with particle j , signifying the local anisotropy. The ‘length’ of this anisotropy is given by R and ϵ describes the ratio between its ‘length’ and ‘width’.

In order to characterize the global laning of big particles in each single frame, we define a laning-order parameter S_b , which is the largest eigenvalue of a second-rank tensor $T = 2N^{-1} \sum_{j=1}^N \mathbf{u}_j \otimes \mathbf{u}_j - I$, where I is an identity matrix. $S_b = 1$ denotes perfect alignment

(of the preferred angles), while $S_b = 0$ represents a perfectly random phase. Because of the similar morphology of the lane structure in the experiments presented in this paper, we use the same spatial scale $R = 1200 \mu\text{m}$ and the anisotropic aspect ratio $\epsilon = 5$ throughout this analysis. The value of R corresponds to the typical length of lanes in our experiments and the value of ϵ represents the typical length to width ratio.

4. Dependence of lane formation on the number density ratio

The number density ratio between the background and the penetrating particles is one of the most important factors influencing lane formation in our experiments. We study three cases with *low*, *medium* and *high* density clouds of small particles (MF particles with a diameter of $3.4 \mu\text{m}$) injected into the same background cloud of large particles, one after another. The background particle cloud (MF particles with a diameter of $6.8 \mu\text{m}$) is prepared prior to the start of injections and is not replaced between injections. As some volume around the central void is occupied by small particles, the initial number density of the background is increased slightly after each injection. In order to inject small particle clouds with different densities, we set the shaking time (t_s) of the particle dispenser to three different values: (I) low $t_s = 31$ ms, (II) medium $t_s = 33$ ms and (III) high $t_s = 35$ ms. Generally speaking, the longer the shaking time, the more particles are injected. As this increases the number of particles injected as one bunch, this effectively results in denser small particle clouds (see also the next paragraph).

To estimate the number density ratio n_s/n_b , where $n_{s/b}$ is the number density of small/big particles, we select a fixed square area in the center of the penetration region, as shown in figure 3, where we count the number of small (big) particles N_s (N_b): $n_s/n_b = N_s/N_b$. When the small particles pass through the penetration region, N_s increases, while big particles are expelled and N_b decreases. Please note that the variation of N_b with time is the same during penetration for all three injections. The change of n_s/n_b results from the change of N_s , i.e. from the increased density of the small particle cloud. The number density ratio n_s/n_b for all three cases is shown in figure 2.

We quantify the lane structure formed by big particles during penetration by ASIM described in the previous section. For the purpose of eliminating boundary effects and to define the penetration region, we select an ROI (see figure 3). The same ROI is used for all three injection cases. Figure 3 summarizes the results for the three injection cases. For every case it shows two diagrams. In the left column the morphology for in-plane injection is visualized: all positions of small (in red) as well as big (in cyan) particles from 250 frames ($\simeq 5$ s) are superimposed into a single picture. When the small particles are injected from the dispenser mounted on the top flange, the direction of penetration of the small particle cloud is slanted. Apparently, small particles in the upper half of the picture are denser than in the lower half. In this picture a small central square indicates where n_s/n_b was estimated, and the ROI for the calculation of S_b is emphasized. In the right column the temporal evolution of S_b as well as of the particle number in the ROI are shown.

The number of particles in the ROI develops similarly for all three cases. As small particles enter the ROI, big particles are repelled out of the ROI by the small particles. This is possible because the confinement by the plasma potential is weak. As the number density of the small particles is higher than the background cloud, the total number of particles in the ROI is increased during the penetration. As we can see in figure 3, the maximum total number of particles in the ROI occurs at the same time ($t \approx 2$ s) for all injection cases. Also the minimum of

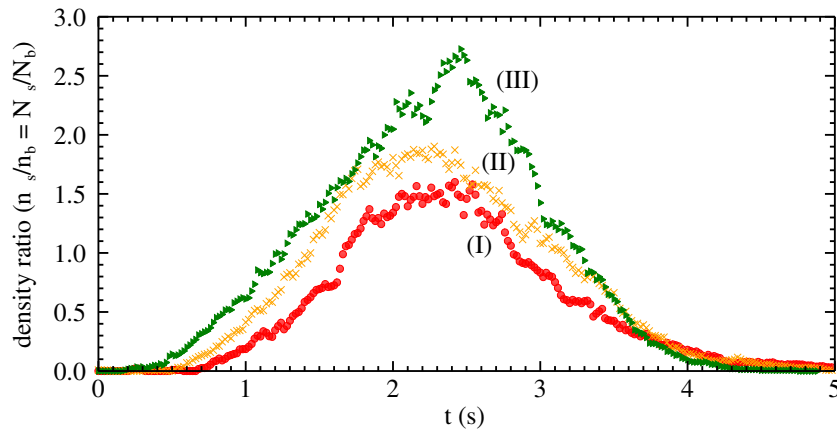


Figure 2. Evolution of the particle number density ratio. The number of large (N_b) and small (N_s) particles is measured in a square close to the center of the penetration region. The number density ratio is given by $n_s/n_b = N_s/N_b$. Three different curves are drawn for three different dispenser shaking times, corresponding to three densities of the injected small particle cloud: (I) $t_s = 31$ ms, low density as red circles, (II) $t_s = 33$ ms, medium density as orange crosses and (III) $t_s = 35$ ms, high density as green triangles.

the number of big particles occurs at the same time ($t \approx 2.5$ s). This implies that the penetration dynamics of small particles is comparable in all three cases.

In contrast, the laning order parameter S_b evolves differently in all three injection cases. It is clearly visible that the lane structure of big particles is only formed in that part of the penetration region where the density of the small particle cloud is high enough, and for the high-density case (III) the order parameter even seems to attain some plateau during the penetration. For case (III) due to the high density of small particles injected, once they penetrate into the big particles, they effectively cage the big particles (as described in detail in section 7). Therefore, the lane structure of big particles is formed instantaneously and maintained until the small particles leave the ROI. In case (I) and also (II), the number density of small particles is not sufficient to cage the big particles everywhere, so that the big particles on the sides can escape across the wings of the small particle cloud. Also note that with increasing density of the small particle cloud, S_b reaches its maximum value earlier: for the low-density case (I) $t_{(I)} \approx 3$ s, for the medium-density case (II) $t_{(II)} \approx 2.5$ s and for the high-density case (III) $t_{(III)} \approx 1.3$ s. This is because at later times even cases (I) and (II) attain sufficient densities inside the ROI to cage the big particles from escaping. Interestingly enough, case (I) reaches the highest value $S_{b(I)} \approx 0.3$, whereas $S_{b(II)} \approx 0.28$ and $S_{b(III)} \approx 0.23$. Even though fewer big particles get caged in case (I), the lanes formed by the big particles have a narrower distribution of preferred angles, which directly leads to a higher value of S_b . For case (II) and increasingly so for case (III), the penetration geometry allows for a wider range of preferred angles, and therefore for a systematic decrease of the peak value of S_b . Take note that these results are not conclusive, since the evolution of S_b strongly depends on the initial configuration. According to the numerical study presented in [11], S_b varies dramatically for statistically independent but thermodynamically equivalent initial configurations. A huge number of repetitions of the experiment (several hundreds of times according to the simulation) is necessary to obtain a statistically significant laning order parameter. This is not really

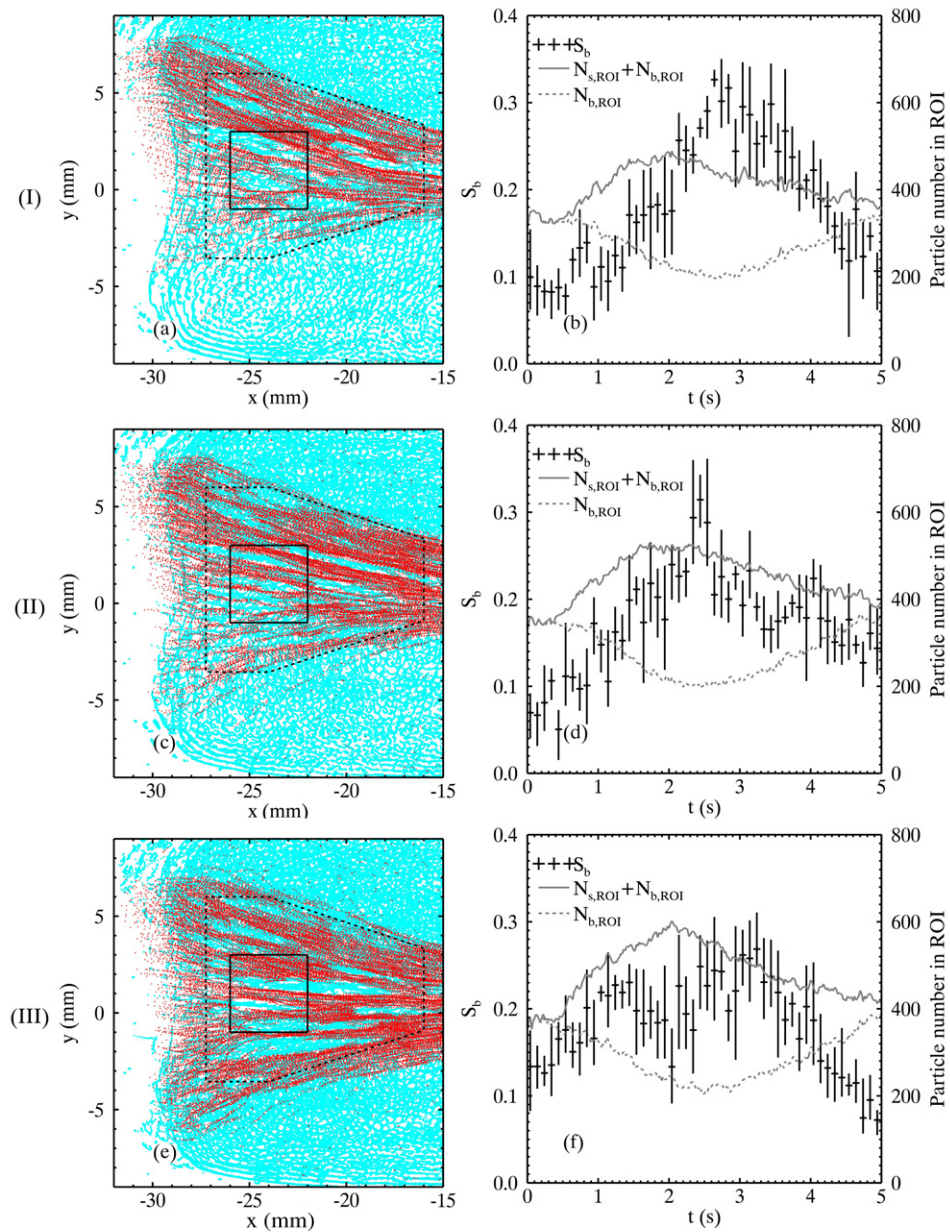


Figure 3. Influence of the number density ratio on the dynamics of lane formation. For three different densities of the injected small particle cloud, (I), (II) and (III) from top to bottom (see also movies 1, 2 and 3, respectively, available from stacks.iop.org/NJP/14/073058/mmedia), two pictures are shown. On the left is a superposition of particle trajectories during the penetration (250 frames $\simeq 5$ s). The big MF particles ($6.8 \mu\text{m}$ diameter) are represented in cyan, and the penetrating MF particles ($3.4 \mu\text{m}$ diameter) in red. The small solid rectangle at the center of the penetration region is used during the estimation of the number density ratio. The dashed line indicates the region of interest (ROI) used during the calculation of S_b . On the right, the evolution of the laning order parameter for big particles S_b (crosses), as well as the number of big particles $N_{b,ROI}$ (dashed line) and the total number of particles $N_{s,ROI} + N_{b,ROI}$ (solid line) in the ROI, is shown.

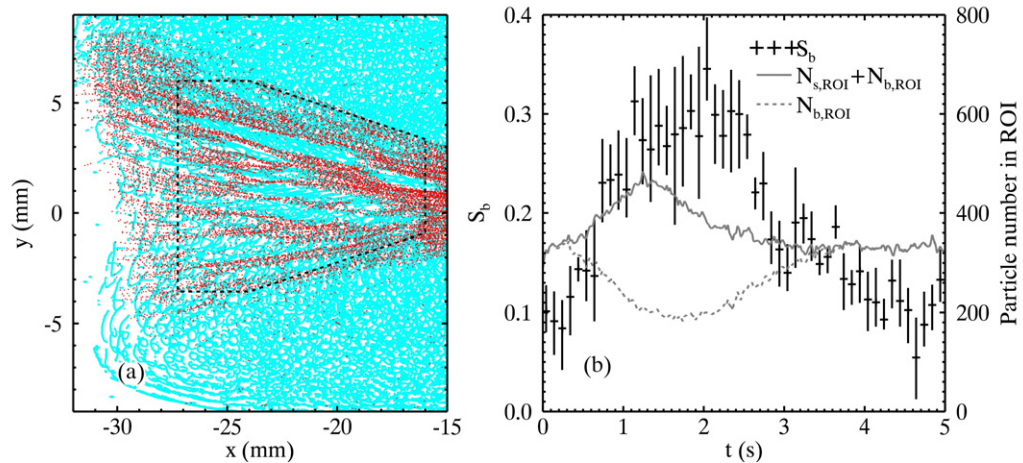


Figure 4. Influence of the size ratio on the dynamics of lane formation (see also movie 4, available from stacks.iop.org/NJP/14/073058/mmedia). On the left is a superposition of particle trajectories during the penetration (250 frames \simeq 5 s). The big background MF particles ($9.2 \mu\text{m}$ diameter) are represented in cyan, and the small penetrating MF particles ($3.4 \mu\text{m}$ diameter) in red. The dashed line indicates the region of interest (ROI) used during the calculation of S_b . On the right the evolution of the laning-order parameter for big particles S_b (crosses) as well as the number of big particles $N_{b,ROI}$ (dashed line) and the total number of particles $N_{s,ROI} + N_{b,ROI}$ (solid line) in the ROI is shown.

feasible in our experiments due to the limited resources (gas, particles, operator time) on board the ISS.

5. Dependence of lane formation on the size ratio

In order to compare the influence of the particle size ratio, we use MF particles with a diameter of $9.2 \mu\text{m}$ as background particles and keep MF particles with a diameter of $3.4 \mu\text{m}$ as the penetrating particles. The same pressure, rf voltage and ROI as in section 4 are used. As we see in figure 4, the number of big particles and the total number of particles in the ROI are comparable with case (I) of the previous section. However, the maximum of the total particle number and the minimum of the number of big particles occur earlier than for case (I). This implies a higher penetration speed. Also a higher peak value of S_b is attained.

For a combination of particles with larger difference in size, in other words, larger nonadditivity [21], this seems counter-intuitive. The simulation results in [11] show that with higher nonadditivity, particles penetrate slower and the peak value of the laning-order parameter becomes smaller. However, in reality, the situation is more complicated. The change of the size of background particles changes not only the nonadditivity, but also the particle cloud profile as well as the local plasma parameters. The difference between the ion and the electron density tends to be larger in the plasma with bigger particles because of electron depletion due to the higher charge on the surface of big particles [25]. This results in a stronger electric field and therefore increases the driving force and penetration speed. Besides, the coupling strength for the cloud of bigger particles is higher, resulting in a more ordered system. Small particles can

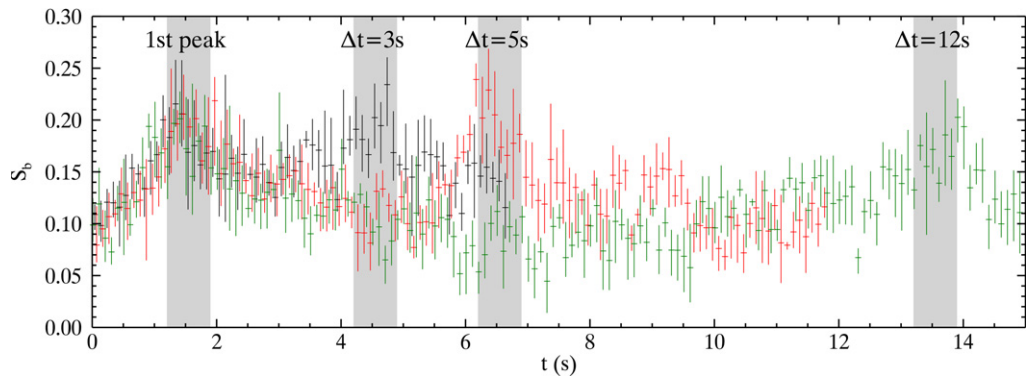


Figure 5. Memory effect on the laning-order parameter. The temporal evolution of S_b is displayed for three sets of two consecutive injections with different intervals Δt . Symbols with error bars in black, red, and green correspond to the cases with $\Delta t = 3, 5, 12$ s (see also movies 5, 6 and 7, available from stacks.iop.org/NJP/14/073058/mmedia), respectively. The locations of the peaks of S_b are shaded in grey.

penetrate more easily in such a system than in a disordered system. Since the nonadditivity has a minor influence on the lane formation compared to other factors such as particle interaction or driving force, we can conclude from the experiment that a combination of particles with a larger size difference leads to more pronounced lane formation.

6. Memory effect

As mentioned before, when the small particles penetrate the big particle cloud, they repel these background particles outwards, creating sponge-like tunnels. After the small particles have passed through the cloud of big particles, it takes some time for the big particles to relax and refill the empty tunnels [29, 30]. If small particles are injected into the big particle cloud before complete relaxation of the background, the remnant of the sponge-like structure will influence the penetration of small particles and therefore the dynamics of lane formation. We call this the ‘memory effect’ of lane formation.

In this section, we investigate this phenomenon by injecting two consecutive bunches of small particles with a variable time interval Δt in between. We used $\Delta t = 3$ s, $\Delta t = 5$ s and $\Delta t = 12$ s. The memory effect is evaluated in terms of the laning-order parameter of the big particles S_b and the penetration speed of the small particles. The penetrating particles have a diameter of $3.4 \mu\text{m}$ and the background particles have a diameter of $9.2 \mu\text{m}$.

Figure 5 shows the temporal evolution of S_b . Three messages can be read from the diagram, namely the time separation of peaks by consecutive injections, the relaxation process of S_b and the peak value of S_b . For all three cases the laning-order parameter has a first maximum at $t \approx 1.5$ s after the small particles appear in the camera view. The initial value of S_b , its rise time, peak value and relaxation for the first injection are basically identical in all three cases. The second peak of the order parameter, however, appears at different times completely determined by the selected injection interval. Of all three cases only for the largest injection time interval $\Delta t = 12$ s is the relaxation time long enough for the laning-order parameter to reach its initial value $S_b \approx 0.08$. That means that the lane structure among the big particles vanishes, and the

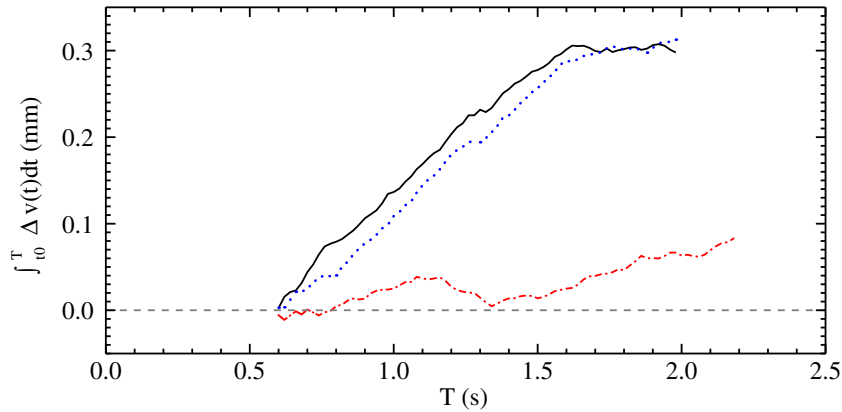


Figure 6. Memory effect on the penetration speed. The cumulative difference $\int_{t_0}^T \Delta \bar{v}(t) dt$ of the penetration speed of small particles between consecutive and initial injection: $\Delta \bar{v}(t) = \bar{v}(t + \Delta t) - \bar{v}(t)$, is plotted against time T , where t_0 is 0.6 s. $\bar{v}(t)$ is the mean speed of small particles in the x -direction, and $\Delta t \in [3 \text{ s}, 5 \text{ s}, 12 \text{ s}]$ is the selected time interval. The solid line in black corresponds to $\Delta t = 3 \text{ s}$, the dotted line in blue corresponds to $\Delta t = 5 \text{ s}$ and the dashed dotted line in red corresponds to $\Delta t = 12 \text{ s}$.

tunnels left by the small particles are filled. The background particles form a homogeneous dust cloud, similar to before the initial injection. In this case, the consecutive penetration can be treated independently of the initial penetration. For the other two cases where $\Delta t = 3 \text{ s}$ and $\Delta t = 5 \text{ s}$, the relaxation time is too short, so that the laning-order parameter cannot be restored to the initial value. The lane structure in the background does not dissolve completely and the tunnels remain to different extents depending on the relaxation time. For the shortest interval $\Delta t = 3 \text{ s}$, S_b falls to ≈ 0.14 , before it starts to increase again due to the consecutive injection. For $\Delta t = 5 \text{ s}$ it reaches $S_b \approx 0.10$. Note that for all three cases the relaxation of the first peak is completely identical till $t \approx 2.8 \text{ s}$ and that the relaxation of the second peaks is consistent. Also, the value of the second peak is independent of the relaxation process. Even though, for the consecutive injection, S_b starts from ≈ 0.14 , ≈ 0.10 or ≈ 0.08 , it reaches the same peak value $S_b \approx 0.22$ in all three cases. That means that the memory effect in lane formation is a linear phenomenon.

The memory effect can also be investigated from the point of view of the kinetics of the small particles. The tunnels left in the background particles during the initial penetration influence the penetration speed of the small particles in the consecutive injection. We investigate this effect by measuring the cumulative difference of mean Gauss-fit penetration speed (x -component of velocity) of small particles between consecutive and initial injection: $\int_{t_0}^T \Delta \bar{v}(t) dt$, where $\Delta \bar{v}(t) = \bar{v}(t + \Delta t) - \bar{v}(t)$, $\bar{v}(t)$ is the average speed of small particles in the x -direction, T is the penetration time (integral from $t_0 = 0.6 \text{ s}$ in our case), and $\Delta t \in [3 \text{ s}, 5 \text{ s}, 12 \text{ s}]$ is the selected time interval. The results for all three cases are shown in figure 6. In the case of $\Delta t = 12 \text{ s}$, the difference varies around zero during the whole penetration process, leading to a cumulative difference slightly above zero. The small particle speed in the consecutive penetration is marginally increased over the initial penetration. Due to the short penetration time and lack of statistics it is not clear if this marginal increase derives from statistical fluctuations or

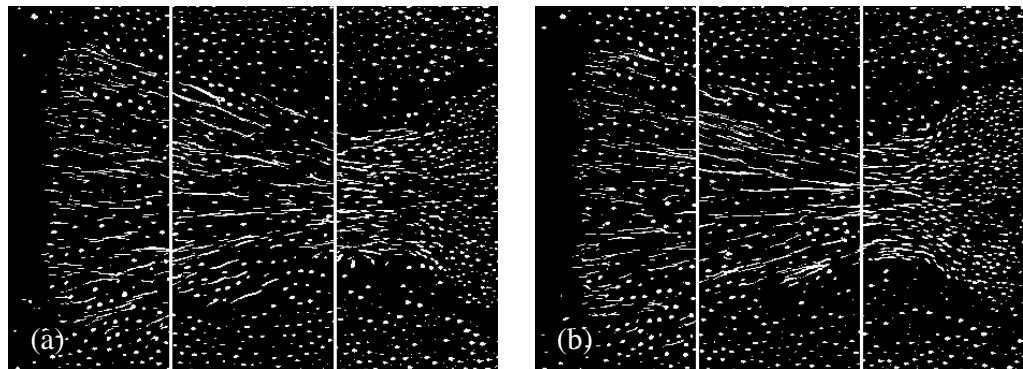


Figure 7. Illustration of the memory effect on the penetration path taken by small particles. The pictures show a superposition of particle positions of four consecutive frames at three times during the penetration for the time interval $\Delta t = 3$ s. The left picture (a) shows the initial injection, and the right picture (b) the corresponding consecutive injection. Each picture is made up of three panels. Each panel shows a part of the original picture at its original position. The left panel is cut from the original at the time point of 0.7 s after the injection is issued, the central panel at the time point of 1.4 s, and the right panel at the time point of 2.1 s.

from a change in the background structure. For the cases with short relaxation time $\Delta t = 3$ s, 5 s, the penetration speed difference is mainly positive during the penetration. This can be clearly seen as a positive slope of the cumulative difference, indicating a speedup of the consecutive penetration process over the initial one. The dogleg bend of both curves at $t = 1.6$ s happens when the particle bunch from the consecutive injection hits the cloud of small particles from the initial injection close to the center of the chamber. The speedup is mainly caused by the tunnels formed during the first penetration, which dramatically reduces the resistance the small particles experience during the penetration. With the presence of these tunnels, the small particles will mainly follow them, taking the same path as in the previous penetration, as can be seen in figure 7. With the longer time interval $\Delta t = 12$ s, small particles take completely different paths to penetrate the background particle cloud.

7. Crossover from lane formation to phase separation

As we described in the previous sections, each experiment goes through three main stages. Initially, the small particles are injected into the plasma and move under the influence of the inhomogeneous plasma potential. Then they enter the background cloud of big particles where lane formation can occur. Finally, when the small particles approach the center where the driving force exerted on small particles, F_d , decreases due to the effective potential configuration, phase separation of small and big particles due to nonadditivity starts to dominate and the small particles form a droplet. Between all three stages there is a smooth transition. The transition from the injection to the laning stage is significantly influenced by the initial configuration of the contact, which has been extensively studied numerically in [11]. During the laning stage the small and big particles form an array of interpenetrating lanes [9]. At the final stage of the

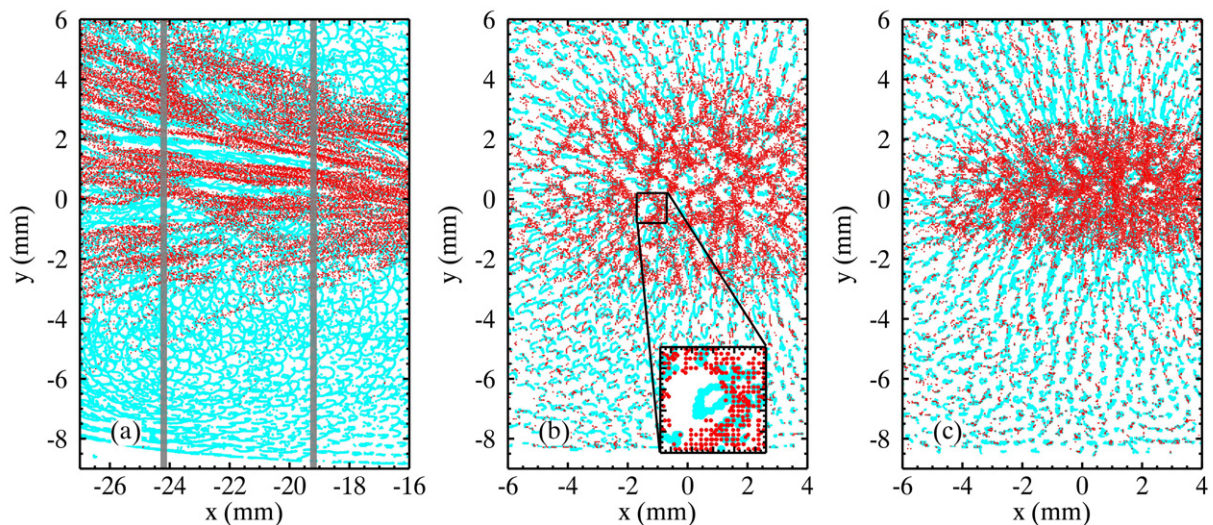


Figure 8. The cage effect. Small MF particles (a) with diameter $3.4 \mu\text{m}$ are injected in-plane and (b, c) with diameter $2.5 \mu\text{m}$ are injected in-the-line-of-sight into a background of big particles with diameters 6.8 and $14.9 \mu\text{m}$, respectively. The pictures are a superposition of particle positions for (a) 250 frames and (b, c) 200 frames, with penetrating small particles in red, and background big particles in cyan. Picture (a) is adopted and magnified from picture (b) in figure 3. The in-the-line-of-sight pictures have been recorded with a shifted z -position of the laser and camera system, (b) $z = 24 \text{ mm}$ (see also movie 8, available from stacks.iop.org/NJP/14/073058/mmedia), and (c) $z = 19 \text{ mm}$ (see also movie 9). The two vertical gray bars at $x = -24 \text{ mm}$ and $x = -19 \text{ mm}$ in (a) indicate the equivalent positions of the laser planes used for pictures (b) and (c).

experiments, the ratio of the magnitude of the driving force to the nonadditivity parameter, $R = F_d/\Delta$, describes the competition between lane formation and demixing, similar to the Weber number in a macroscopic fluid system, which is used to determine the transition from lane formation to the classical Rayleigh–Taylor instability [31]. As the ratio R decreases the penetrating particles form a separated droplet (composed of small particles only) that moves as an ensemble towards the center of the chamber. This phenomenon is generally known as demixing (phase separation) [11, 21, 32].

During the crossover from the laning stage to the phase separation stage there is a change in the laning mode, from free lane formation to a demixing dominated mode, where the interior part of the small particle cloud already forms a honeycomb-like substructure, in which big particles can be effectively caged, while big particles closer to the wings of the small particle cloud are quickly expelled (see section 4 and figure 8). During this crossover, lanes are formed by the big particles only. To finally form a dense cluster of small particles (see figure 9), the lanes of big particles are expelled from the rear of the honeycomb structure. This is an important process in the phase separation dynamics.

The cage effect and the crossover can be better visualized in the in-the-line-of-sight injection. Due to the limitations of the setup configuration (camera position and dispenser arrangement) as described in section 2, we are not able to perform experiments with the

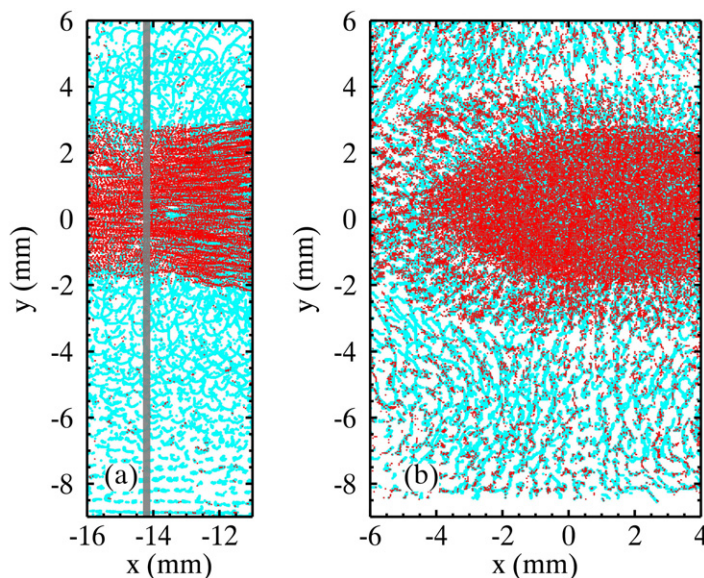


Figure 9. Crossover from lane formation to phase separation. Small MF particles (a) with diameter $3.4 \mu\text{m}$ are injected in-plane and (b) with diameter $2.5 \mu\text{m}$ are injected in-the-line-of-sight into a background of big particles with diameters 6.8 and $14.9 \mu\text{m}$, respectively. The pictures are a superposition of particle positions for (a) 250 frames and (b) 200 frames, with penetrating small particles in red, and background big particles in cyan. Picture (a) is an extension of picture (a) in figure 8. The in-the-line-of-sight picture has been recorded with a shifted z -position $z = 14 \text{ mm}$ of the laser and camera system (see also movie 10, available from stacks.iop.org/NJP/14/073058/mmedia). The vertical gray bar at $x = -14 \text{ mm}$ in picture (a) indicates the equivalent position of the laser plane.

same particle combinations as for in-plane injection. Therefore, we used MF particles with a diameter of $2.5 \mu\text{m}$ as the penetrating particles and MF particles with a diameter of $14.9 \mu\text{m}$ as background particles. This makes it easier to distinguish particles of different types in the recorded movies. Here, we do not intend to make quantitative comparison but only demonstrate the cage effect qualitatively.

As we can see in figures 8(b) and (c), the small particles form a honeycomb structure, penetrating the big particle cloud. These pictures show two cross sections through the system 24 and 19 mm away from the center of the chamber in the z -direction. The equivalent positions of these layers in an in-plane injection are indicated as gray bars in figure 8(a), which is adopted and magnified from figure 3(b). The honeycomb structure is visible as a band structure in the in-plane injection. Within the cells of such a honeycomb structure, big particles are caged and form lanes. The big particles in the perimeter of the small particle cloud move outwards when the small particles contact and penetrate the respective layers. This corresponds to the repulsion of big particles from the ROI mentioned in the previous section. These particles move back to their original positions after the small particles leave the layer, resulting in curly trajectories.

When we look at the cross section closer to the center of the chamber ($z = 19 \text{ mm}$), the small particle cloud becomes much denser, so that the cells of the honeycomb structure shrink dramatically. The system starts the crossover from lane formation to phase separation.

The fully phase separated particle cloud in the vicinity of the void ($z = 14$ mm) is shown in figure 9. The big particles are almost completely expelled out of the small particle cluster so that the honeycomb structure of small particles vanishes. At this moment, small particles and big particles demix completely and phase separation of the two particle species is achieved.

8. Conclusion

To conclude, we have presented a series of experiments on lane formation under microgravity conditions on board the ISS with the PK-3 Plus setup. Big particles form pronounced lane structures when small particles are driven and penetrate through them. A sensitive lane-order parameter based on anisotropic scaling indices enabled us to identify an optimal number density ratio between small and big particles for the lane formation. It is also found that big particles are more easily caged between the lanes formed by small particles if the number of injected small particles is increased. These caged big particles form streaming lanes and result in a peak value in the lane-order parameter. As the small particles leave the big particle cloud, the leftover cavities in the big particle cloud are refilled with big particles due to relaxation. By tuning the time interval between two consecutive penetration events of small particles, we investigated the ‘memory’ effect of the previous penetration on the consecutive one. The shorter the time interval, the greater the number of tunnels left from the initial penetration and the faster the small particles penetrate through the background particle cloud. We found that the peak values of the lane-order parameter from all cases with different time intervals are all about 0.22, which indicates that the ordering of the laning pattern has no evident dependence on the time interval and that the memory effect is linear. These leftover cavities from the previous penetration event serve as fast channels for the consecutive injection event and result in a clear speedup of the penetration of small particles. In addition, a crossover from free lane formation to a demixing dominated mode of the nonequilibrium system has been observed.

Acknowledgments

The PK-3 Plus project is funded by the space agency of the Deutsches Zentrum für Luft- und Raumfahrt eV with funds from the Federal Ministry for Economy and Technology according to a resolution of the Deutscher Bundestag under grant number 50 WP 0203. MS is funded by the European Union via a Marie Curie IOF. We thank the firm Kayser–Threde for constructive collaboration during the development, fabrication, test and delivery of the laboratory, RSC-Energia for continuous support during the project and the Mission Control Centre in Korolev for help in planning and performing the experiments.

References

- [1] Halsey T C 1992 Electrorheological fluids *Science* **258** 761–6
- [2] Umbanhowar P B, Melo F and Swinney H L 1996 Localized excitations in a vertically vibrated granular layer *Nature* **382** 793–6
- [3] Ivlev A V, Steinberg V, Kompaneets R, Höfner H, Sidorenko I and Morfill G E 2007 Non-newtonian viscosity of complex-plasma fluids *Phys. Rev. Lett.* **98** 145003
- [4] Feng Y, Goree J and Liu B 2010 Viscoelasticity of 2D liquids quantified in a dusty plasma experiment *Phys. Rev. Lett.* **105** 025002

- [5] Thomas H M, Morfill G E, Demmel V, Goree J, Feuerbacher B and Möhlmann D 1994 Plasma crystal: Coulomb crystallization in a dusty plasma *Phys. Rev. Lett.* **73** 652–5
- [6] Chu J H and I L 1994 Direct observation of Coulomb crystals and liquids in strongly coupled rf dusty plasmas *Phys. Rev. Lett.* **72** 4009–12
- [7] Hayashi Y and Tachibana K 1994 Observation of Coulomb-crystal formation from carbon particles grown in a methane plasma *Japan. J. Appl. Phys.* **33** L804–8003
- [8] Schwabe M, Konopka U, Bandyopadhyay P and Morfill G E 2011 Pattern formation in a complex plasma in high magnetic fields *Phys. Rev. Lett.* **106** 215004
- [9] Sütterlin K R *et al* 2009 Dynamics of lane formation in driven binary complex plasmas *Phys. Rev. Lett.* **102** 085003
- [10] Sütterlin K R, Thomas H M, Ivlev A V, Morfill G E, Fortov V E, Lipaev A M, Molotkov V I, Petrov O F, Wysocki A and Löwen H 2009 Lane formation in driven binary complex plasmas on the international space station *IEEE Trans. Plasma Sci.* **38** 861–8
- [11] Jiang K, Du C-R, Sütterlin K R, Ivlev A V and Morfill G E 2010 Lane formation in binary complex plasmas: role of initial configurations and non-additive interactions *Eur. Phys. Lett.* **92** 65002
- [12] Fortov V E, Ivlev A V, Khrapak S A, Khrapak A G and Morfill G E 2005 Complex (dusty) plasmas: current status, open issues, perspectives *Phys. Rep.* **421** 1–103
- [13] Morfill G E and Ivlev A V 2009 Complex plasmas: an interdisciplinary research field *Rev. Mod. Phys.* **81** 1353
- [14] Allen J E, Annaratone B M and de Angelis U 2000 On the orbital motion limited theory for a small body at floating potential in a Maxwellian plasma *J. Plasma Phys.* **63** 299–309
- [15] Du C-R, Khrapak S A, Antonova T, Steffes B, Thomas H M and Morfill G E 2011 Frequency dependence of microparticle charge in a radio frequency discharge with Margenau electron velocity distribution *Phys. Plasmas* **18** 014501
- [16] Goree J, Morfill G E, Tsytovich V N and Vladimirov S V 1999 Theory of dust voids in plasmas *Phys. Rev. E* **59** 7055–67
- [17] Thomas H M *et al* 2008 Complex plasma laboratory PK-3 Plus on the International Space Station *New J. Phys.* **10** 033036
- [18] Schwabe M, Zhdanov S K, Thomas H M, Ivlev A V, Rubin-Zuzic M, Morfill G E, Molotkov A M, Lipaev V I, Fortov V E and Reiter T 2008 Nonlinear waves externally excited in a complex plasma under microgravity conditions *New J. Phys.* **10** 033037
- [19] Heidemann R J *et al* 2011 Comprehensive experimental study of heartbeat oscillations observed under microgravity conditions in the PK-3 Plus laboratory on board the International Space Station *Phys. Plasmas* **18** 053701
- [20] Khrapak S A *et al* 2011 Freezing and melting of 3D complex plasma structures under microgravity conditions driven by neutral gas pressure manipulation *Phys. Rev. Lett.* **106** 205001
- [21] Ivlev A V, Zhdanov S K, Thomas H M and Morfill G E 2009 Fluid phase separation in binary complex plasmas *Eur. Phys. Lett.* **85** 45001
- [22] Takahashi K, Hayashi Y and Adachi S 2011 Measurement of electron density in complex plasmas of the PK-3 plus apparatus on the International Space Station *J. Appl. Phys.* **110** 013307
- [23] Khrapak S and Morfill G 2009 Basic processes in complex (dusty) plasmas: charging, interactions, and ion drag force *Contrib. Plasma Phys.* **49** 148–68
- [24] Khrapak S A and Morfill G E 2012 Ionization enhanced ion collection by a small floating grain in plasmas *Phys. Plasmas* **19** 024510
- [25] Havnes O, Morfill G E and Goertz C K 1984 Plasma potential and grain charges in a dust cloud embedded in a plasma *J. Geophys. Res.* **89** 10999–11003
- [26] R ath C, Bunk W, Huber M B, Morfill G E, Retzlaff J and Schuecker P 2002 Analysing large-scale structure-I. Weighted scaling indices and constrained randomization *Mon. Not. R. Astron. Soc.* **337** 413–21
- [27] Ivlev A V *et al* 2008 First observation of electrorheological plasmas *Phys. Rev. Lett.* **100** 095003

- [28] R ath C, Monetti R, Bauer J, Sidorenko I, M uller D, Matsuura M, Lochm uller E-M, Zysset P and Eckstein F 2008 Strength through structure: visualization and local assessment of the trabecular bone structure *New J. Phys.* **10** 125010
- [29] Ivlev A V, Thomas H M, Morfill G E, Molotkov V I, Lipaev A M, Fortov V E, Hagl T, Rothermel H and Krikalev S 2006 Coalescence of complex plasma clouds *New J. Phys.* **8** 25
- [30] Arp O, Caliebe D and Piel A 2011 Cavity dynamics and particle alignment in the wake of a supersonic projectile penetrating a dusty plasma *Phys. Rev. E* **83** 066404
- [31] Wysocki A and L owen H 2004 Instability of a fluid–fluid interface in driven colloidal mixtures *J. Phys.: Condens. Matter* **16** 7209–24
- [32] Wysocki A *et al* 2010 Kinetics of fluid demixing in complex plasmas: role of two-scale interactions *Phys. Rev. Lett.* **105** 045001

Model experiment for studying lane formation in binary complex plasmas

C.-R. DU^(a), K. R. SÜTTERLIN, A. V. IVLEV, H. M. THOMAS and G. E. MORFILL

Max-Planck-Institute for Extraterrestrial Physics - Giessenbachstr., 85748 Garching, Germany, EU

received 15 May 2012; accepted 26 July 2012

published online 29 August 2012

PACS 52.27.Lw – Dusty or complex plasmas; plasma crystals

PACS 64.75.Cd – Phase equilibria of fluid mixtures, including gases, hydrates, etc.

PACS 61.20.-p – Structure of liquids

Abstract – We present the first experimental realisation on lane formation in binary complex plasmas under gravity conditions. The amount of penetrating particles can be controlled. The experiment can be operated with stable conditions continuously, which allows to study steady state. The driving force is independent of time and position and the background density is homogeneous and isotropic. This provides an ideal model system for comparison with numerical experiments and observations in colloidal suspensions. The experiment setup is based on PK-3 Plus laboratory operated on the International Space Station. Gravitation is compensated by thermophoretic force and penetrating particles are controlled via a toroidal vortex with poloidal flow. The evolution of lane formation along the penetration direction is illustrated by lane order parameter.

Copyright © EPLA, 2012

Introduction. – As the ubiquitous prototype of non-equilibrium pattern formation, lane formation has drawn a lot of attention over the last decade. It is a generic process, which has been studied for mixtures in various branches of physics, for instance colloidal suspensions [1–5] and molecular ions [6]. Besides physics, such process has also been studied in the context of self-organization, for instance in biology [7] with traffic routes of army ants. Recently lane formation was also discovered in complex plasma experiments performed under microgravity conditions on board the International Space Station (ISS) [8,9], and further investigated with numerical simulations [10]. Complex plasma is composed of weakly ionized gas and microparticles [11,12] that attain a huge charge and interact strongly via a shielded Coulomb potential. Complex plasmas have the unique feature of tunable damping, from virtually undamped kinetics to fully overdamped. This allows to study pattern formation in completely new dynamical regime.

So far the experiments performed on board the ISS allowed for a limited control of experimental conditions. The main problem is the weak confinement of the background particles, which resulted in inhomogeneities and a strong influence of the penetrating particles on the structure of the background. In addition the driving force is

pointed to the center of the experiment chamber, and its magnitude depends on the distance from the center. All together this results in a strong dependence of the penetration dynamics on time and position. The experimental setup on the ISS only allows to inject bunches of particles, therefore continuous operation and fine tuning of penetrating particle numbers is not possible. Besides, due to the low frequency of the camera equipped on board the ISS, the tracking of the penetrating particles has a low accuracy, therefore the temporal evolution of the lane structure could only be quantified for the background particles. These limits interfered with a direct quantitative comparison with numerical simulation [8,10].

In this letter, we introduce an experiment, where lanes were formed by penetrating particles. The force driving the particles was practically constant along the penetration direction and the background density distribution was homogenous and weakly influenced by the penetrating particles. Thanks to a fast camera, we were able to track the penetrating particles and observe the gradual formation of lane structure of penetrating particles after they entered the background cloud.

Experiment. – The experiment was performed on ground in a modified PK-3 Plus chamber, which was originally designed for the microgravity experiments on board the ISS [13]. The chamber consists of two

^(a)E-mail: chengran.du@mpe.mpg.de

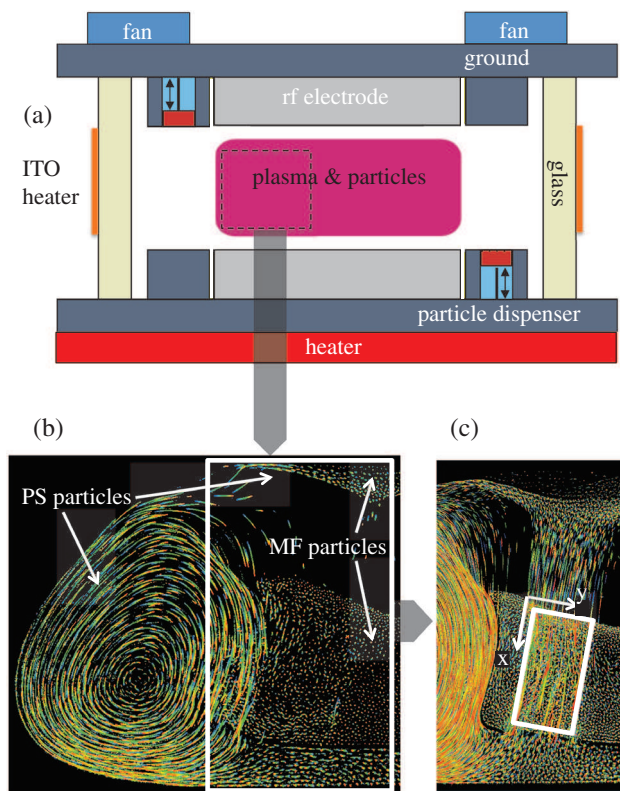


Fig. 1: Sketch of the modified PK-3 Plus chamber (a) and illustration of particle motions in the presence of thermal gradient of 15 K/cm (b) and after the further increase of the temperature of bottom electrode (c). Panel (a) shows a side view of the PK-3 Plus chamber with additional ITO heaters installed on the glass wall. The field of view recorded by the camera is marked by a rectangle (dashed lines). The particles in the field of view are illuminated by a narrow laser plane. Therefore, only a cross-section of the complex plasma through the center of the discharge chamber is visible. Note that the system is cylindrical symmetric. Particle motion in this area is shown in panel (b). Panels (b) and (c) are overlays of 250 consecutive experiment images (color coded from blue to red), where the particle trajectories can be clearly identified. In panel (b) small particles (MF particles) form a reservoir close to the top electrode and a cloud separated by a void while big particles (PS particles) form a “bowl”, with clearly visible particle circulation (vortex) on the side. Panel (c) illustrates particle motion in the white rectangle in panel (b) after the circulation is enhanced. The enhanced circulation leads to a stronger flux of big particles to the reservoir. They sink into the cloud of small particles and form lane structure. The region of interest (ROI) for further analysis is marked by a white rectangle in panel (c), where the x , y axes indicate the coordinate system used in the analysis.

parallel electrodes (3 cm apart) driven in push-pull mode at a frequency of 13.56 MHz to generate plasma, see fig. 1(a). The bottom electrode can be heated up to 100 °C by heaters and the top electrode can be cooled by electric fans. The temperature difference between those two electrodes can be automatically maintained to a

desired value, generating a stable temperature gradient and accordingly a constant thermophoretic force. This force can to some extent compensate for gravity and levitate the particle cloud in the bulk plasma [14]. The temperature inhomogeneity causes an additional effect: It leads to thermal gas creep along the walls of the chamber that can drive circulations of the neutral gas and in the particle cloud [15]. The circulating particles form a toroidal vortex with poloidal flow [16,17]. This vortex was used to control the flow of penetrating particles. In order to enhance the circulation and prevent losing particles to the glass wall, we installed indium tin oxide (ITO) heaters on the glass walls to control their temperature, see fig. 1(a). Microparticles in the plasma are illuminated by a vertical laser sheet (perpendicular to the electrode) with a thickness of about 100 μm and recorded at 90° by a high-speed complementary metal-oxide-semiconductor (CMOS) camera. The recording rate can reach 1000 frames per second with a spatial resolution of 28 μm per pixel. The particle position can be calculated with subpixel resolution in postprocessing with an accuracy of 3 μm .

The experiment presented here was done in an argon gas discharge maintained at a gas pressure of 30 Pa and an rf effective voltage of ≈ 15 V on each electrode. We injected polystyrene (PS) particles (7.57 μm diameter and 1.05 g/cm³ mass density) and melamine-formaldehyde (MF) particles (5.26 μm diameter and 1.51 g/cm³ mass density). From theoretical calculations a complete compensation of gravity through the thermophoretic force for both particle types is attained at a vertical temperature gradient of 15 K/cm in the gas. Accordingly we fixed the temperature of bottom electrode, top electrode and glass wall to 80 °C, 35 °C, and 63 °C, respectively, to obtain a particle cloud configuration as shown in fig. 1(b). The big particles formed a “bowl” shape with a strong circulation (vortex) on the side. The small particles formed a cloud inside the “bowl”, divided into two parts by the void in the center of the chamber. The part below the void was significantly larger than the one above it. The formation of this spacial configuration is governed mainly by the distribution of plasma potential and ion drift inside the gas discharge. As can be seen a few big particles can escape the vortex at the top, where they flow into a small reservoir of small and big particles trapped above the central void. Eventually the big particles fall from this reservoir down towards the central cloud of small particles.

A further increase of the temperature of the bottom electrode by 5% enhances the circulation on the side of the big particle cloud. This increases the flux of big particles into the reservoir, and consequently the number of big particles falling downwards under a small angle (around 10° deviated from vertical direction). These big particles cross the void and penetrate into the small particle cloud as shown in fig. 1(c). During penetration the big particles gradually form lane structures, see fig. 2.

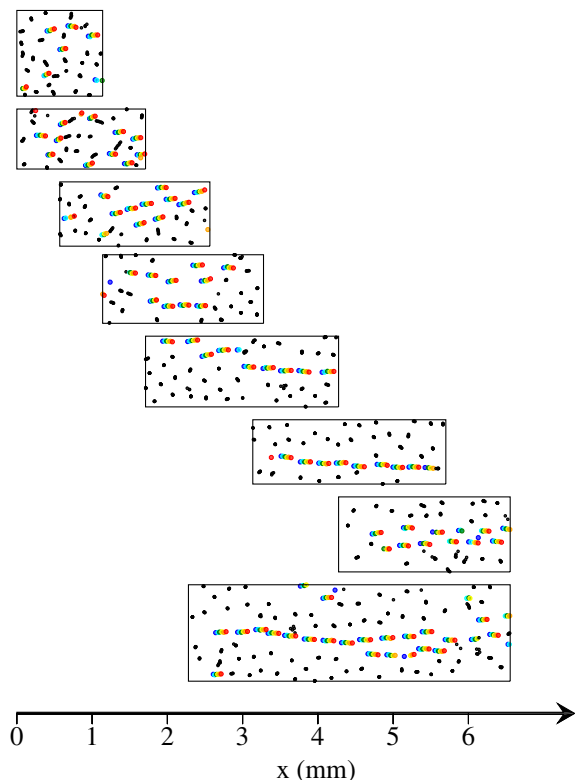


Fig. 2: Samples of lane structure in the ROI of fig. 1(c) along the penetration direction. The eight panels show overlays of tracked particle positions in 6 consecutive frames (corresponding to 12 ms, color coded from blue to red). Since penetrating (big) particles move at a much higher speed than background (small) particles, they can be distinguished based on their dynamics. Small particles are represented by black dots while big particles are represented by colored bands (left end blue and right end red), indicating propagation in the positive x -direction. Initially big particles move independently as they enter the cloud. During propagation lane structures are formed as big particles sink to a deeper position. The average length of lanes increases along the x -direction. On the top end of the ROI we get only individual particles or short lanes comprised of mostly two particles. At lower positions lanes contain more and more particles. The lane size reaches around 10 particles in average at the bottom end of the ROI. In some extreme cases, lanes composed of more than 20 microparticles were observed, see the last panel.

Analysis. – The big particles fall through the void with a speed of about 15 mm/s. The moment they impact the small particle cloud, they are decelerated instantaneously. The speed drops to a value of around 10 mm/s. Penetration speed stays constant through the whole small particle cloud as can be seen from fig. 3(a). While the big particles penetrate the small particle cloud, they gradually form lane structures as depicted in fig. 2. The top layers of the small particle cloud are compressed with a higher number density. However this density decreases in the x -direction, till at $x \simeq 1.5$ mm it attains a value of 21 mm^{-2} and stays constant throughout the remaining penetration (with a negligible fluctuation of less than 5%).

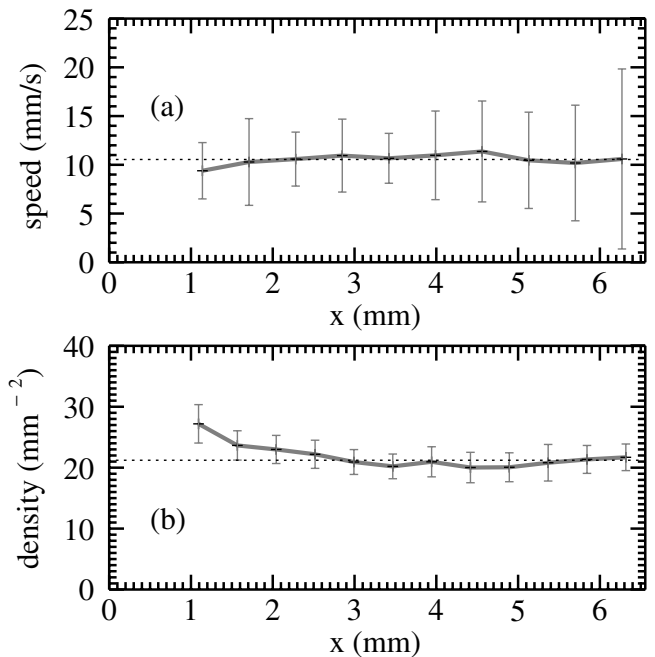


Fig. 3: Speed of penetrating particles (a) and number density of background particles (b) along the penetration direction.

Moreover, the density does not vary in the y -direction perpendicular to the penetration direction. For the largest part of the penetration this provides us with a homogeneous background of small particles and a constant speed of the big particles, which are essential for quantitative comparison of experiments on lane formation in complex plasmas with numerical experiments and results from colloidal suspensions.

In order to quantify the development of the lane formation of penetrating particles, we applied the order parameter Φ , which has been recently used to identify the lane structure in colloidal suspensions [5]: On each big particle i a rectangle of length 3Δ along the penetration direction and width of Δ across is centered, where $\Delta = 0.23$ mm is roughly the interparticle distance of the background cloud. If all the particles contained in the rectangle are big, we define Φ_i to be unity, as shown in the inset of fig. 4(b). If there are one or more small particles contained in the rectangle, $\Phi_i = 0$. In case that there is only the central big particle in the rectangle, we also define $\Phi_i = 0$. In practice we divide the ROI into several narrow segments along the x -axis and average the order parameter $\Phi(x) = \frac{1}{N_x} \sum_1^{N_x} \Phi_i$ in each segment, where N_x is the number of particles in the corresponding segment. The averaged laning order parameter $\Phi(x)$ thus represents the local fraction of particles in the lane structure at the corresponding x -position.

As we clearly see from fig. 4(b), individual big particles move independently as they first enter the small particle cloud. The $\Phi(x \simeq 0)$ is close to zero. During the penetration, initially single big particles join to form short lanes along the penetration direction. Later on these short lanes join each other to form longer lanes. At the same time the number of lanes decreases, due to the particle flux

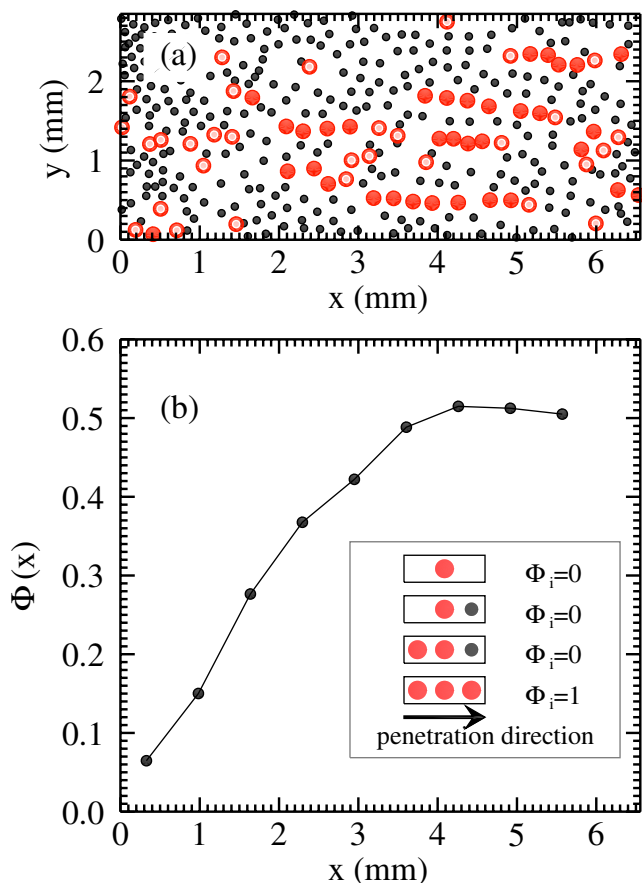


Fig. 4: (Color online) Snapshot of lane formation in the ROI of Fig. 1(c) in the corresponding coordinate system (a) and lane order parameter along the penetration direction (b). Panel (a) shows big particles (red big circles) penetrating the small particle cloud (black small circles). The big particles belonging to the lanes according to Vissers' definition [5] are filled and the others are empty. Panel (b) shows the evolution of lane order parameter (of the ensemble of big particles) along the penetration direction. The inset illustrates the definition of lane order parameter (details in the text).

conservation along the penetration direction. This results in the linear increase of the lane order parameter till $x \simeq 4$ mm, as shown in fig. 4(b). At this stage due to thinning no more single big particles join lanes and existing lanes no longer merge. This results in the plateau of the lane order parameter.

Conclusions. – In this letter we presented a model experiment for studying lane formation in binary complex plasmas. Experimental conditions can be tuned, and the system can be operated in the prescribed regime for a long time. The observed configuration of interpenetrating particles is practically ideal in terms of density-homogeneity and constance of driving force for studying lane formation. This provides a very convenient model system for comparison with computer simulations and experiments in colloidal suspensions. Furthermore we can nicely complement experiments done in colloidal suspensions, as we start from a very different (unmixed) initial

condition. Since our system is homogeneous and one-dimensional, such combined studies can shed a light on the nature of lane formation and non-equilibrium phase transitions.

This work was supported by “Die Raumfahrt-Agentur des Deutschen Zentrums für Luft und Raumfahrt e. V. mit Mitteln des Bundesministeriums für Wirtschaft und Technologie aufgrund eines Beschlusses des Deutschen Bundestages unter dem Förderkennzeichen 50 WP 0203”.

REFERENCES

- [1] DZUBIELLA J., HOFFMANN G. P. and LÖWEN H., *Phys. Rev. E*, **65** (2002) 021402.
- [2] WYSOCKI A. and LÖWEN H., *J. Phys.: Condens. Matter*, **16** (2004) 7209.
- [3] LEUNISSEN M. E., CHRISTOVA C. G., HYNINEN A. P., ROYALL C. P., CAMPBELL A. I., IMHOF A., DIJKSTRA M., VAN ROIJ R. and VAN BLAADEREN A., *Nature*, **437** (2005) 235.
- [4] REX M. and LÖWEN H., *Eur. Phys. J. E*, **26** (2008) 143.
- [5] VISSERS T., WYSOCKI A., REX M., LÖWEN H., ROYALL C. P., IMHOF A. and VAN BLAADEREN A., *Soft Matter*, **7** (2011) 2352.
- [6] NETZ R. R., *EPL*, **63** (2003) 616.
- [7] COUZIN I. D. and FRANKS N. R., *Proc. R. Soc. London, Ser. B*, **270** (2003) 139.
- [8] SÜTTERLIN K. R., WYSOCKI A., IVLEV A. V., RÄTH C., THOMAS H. M., RUBIN-ZUZIC M., GOEDHEER W. J., FORTOV V. E., LIPAЕV A. M., MOLOTKOV V. I., PETROV O. F., MORFILL G. E. and LÖWEN H., *Phys. Rev. Lett.*, **102** (2009) 085003.
- [9] SÜTTERLIN K. R., THOMAS H. M., IVLEV A. V., MORFILL G. E., FORTOV V. E., LIPAЕV A. M., MOLOTKOV V. I., PETROV O. F., WYSOCKI A. and LÖWEN H., *IEEE Trans. Plasma Sci.*, **99** (2009) 1.
- [10] JIANG K., DU C.-R., SÜTTERLIN K. R., IVLEV A. V. and MORFILL G. E., *EPL*, **92** (2010) 65002.
- [11] FORTOV V. E., KHRAPAK A. G., KHRAPAK S. A., MOLOTKOV V. I. and PETROV O. F., *Phys. Usp.*, **47** (2004) 447.
- [12] MORFILL G. E. and IVLEV A. V., *Rev. Mod. Phys.*, **81** (2009) 1353.
- [13] THOMAS H. M., MORFILL G. E., FORTOV V. E., IVLEV A. V., MOLOTKOV V. I., LIPAЕV A. M., HAGL T., ROTHERMEL H., KHRAPAK S. A., SÜTTERLIN K. R., RUBIN-ZUZIC M., PETROV O. F., TOKAREV V. I. and KRIKALEV S. K., *New J. Phys.*, **10** (2008) 033036.
- [14] ROTHERMEL H., HAGL T., MORFILL G. E., THOMA M. H. and THOMAS H. M., *Phys. Rev. Lett.*, **89** (2002) 175001.
- [15] MITIC S., SÜTTERLIN R., HÖFNER H., IVLEV A. V., THOMA M. H., ZHDANOV S. and MORFILL G. E., *Phys. Rev. Lett.*, **101** (2008) 235001.
- [16] RUBIN-ZUZIC M., THOMAS H. M., ZHDANOV S. K. and MORFILL G. E., *New J. Phys.*, **9** (2007) 39.
- [17] HEIDEMANN R., ZHDANOV S., SÜTTERLIN K. R., THOMAS H. M. and MORFILL G. E., *EPL*, **96** (2011) 15001.